

The Lyman Alpha Reference Sample XI: Efficient Turbulence Driven Ly α Escape and the Analysis of IR, CO and [C II]158 μ m *

Accepted for publication in A&A, 22 April 2020

J. Puschnig,^{1,2,*} M. Hayes,¹ G. Östlin,¹ J. Cannon,³ I. Smirnova-Pinchukova,⁴ B. Husemann,⁴ D. Kunth,⁵ J. Bridge,⁶
E. C. Herenz,⁷ M. Messa,⁸ I. Oteo^{9,10}

* e-mail: johannes.puschnig@uni-bonn.de

- 1 Department of Astronomy, University of Stockholm, AlbaNova, Stockholm
2 Argelander-Institut für Astronomie, Auf dem Hügel 71, 53121 Bonn, Germany
3 Department of Physics & Astronomy, Macalester College, 1600 Grand Avenue, Saint Paul, MN 55105, USA
4 Max Planck Institute for Astronomy, Königstuhl 17, 69117 Heidelberg, Germany
5 Institut d'Astrophysique de Paris (IAP), 98bis Boulevard Arago, 75014 Paris, France
6 University of Louisville, Natural Science Bldg. 208, Louisville KY 40292, USA
7 European Southern Observatory, Av. Alonso de Córdova 3107, 763 0355 Vitacura, Santiago, Chile
8 Department of Astronomy, University of Massachusetts Amherst, Amherst, MA 01003, USA
9 Institute for Astronomy, University of Edinburgh, Royal Observatory, Blackford Hill, Edinburgh EH9 3HJ, UK
10 European Southern Observatory, Karl-Schwarzschild-Str. 2, 85748 Garching, Germany

Abstract

Lyman- α (Ly α) is intrinsically the brightest emission line in star forming galaxies. However, its interpretation in terms of physical properties is hampered by the resonant nature of Ly α photons. In order to remedy this complicated situation, the *Lyman Alpha Reference Sample* (LARS) was defined, allowing to study Ly α production and escape mechanisms in 14 local star-forming galaxies. With this paper, we complement our efforts and study the global dust and (molecular) gas content as well as properties of gas associated with photon-dominated regions (PDRs). We aim to characterize the interstellar medium of LARS galaxies, allowing us to relate these newly derived properties to quantities relevant for Ly α escape. We observed LARS galaxies with Herschel/PACS, SOFIA/FIFI-LS, the IRAM 30m telescope and APEX, targeting far-infrared (FIR) continuum and emission lines of [C II]158 μ m, [O I]63 μ m, [O III]88 μ m and low-J CO lines. Using Bayesian methods we derive Draine & Li (2007) model parameters and estimate total gas masses for all LARS galaxies, taking into account a metallicity-dependent gas-to-dust ratio. Star formation rates were estimated from FIR, [C II]158 μ m and [O I]63 μ m luminosities. LARS covers a wide dynamic range in the derived properties, with

*Based on observations with *Herschel*, an ESA space observatory with science instruments provided by European-led Principal Investigator consortia and with important participation from NASA. Based on observations made with the NASA/DLR Stratospheric Observatory for Infrared Astronomy (*SOFIA*). SOFIA is jointly operated by the Universities Space Research Association, Inc. (USRA), under NASA contract NNA17BF53C, and the Deutsches SOFIA Institut (DSI) under DLR contract 50 OK 0901 to the University of Stuttgart. Based on observations carried out with the *IRAM 30m* Telescope. IRAM is supported by INSU/CNRS (France), MPG (Germany) and IGN (Spain). This publication is based on data acquired with the Atacama Pathfinder Experiment (*APEX*). APEX is a collaboration between the Max-Planck-Institut für Radioastronomie, the European Southern Observatory, and the Onsala Space Observatory. Based on observations made with the NASA/ESA *Hubble Space Telescope*, obtained at the Space Telescope Science Institute, which is operated by the Association of Universities for Research in Astronomy, Inc., under NASA contract NAS 5-26555. These observations are associated with program GO 12310.

FIR-based star formation rates from $\sim 0.5\text{--}100 M_{\odot} \text{ yr}^{-1}$, gas fractions between $\sim 15\text{--}80\%$ and gas depletion times ranging from a few hundred Myr up to more than 10 Gyr. The distribution of LARS galaxies in the Σ_{gas} vs. Σ_{SFR} (Kennicutt-Schmidt plane) is thus quite heterogeneous. However, we find that LARS galaxies with the longest gas depletion times, i.e. relatively high gas surface densities (Σ_{gas}) and low star formation rate densities (Σ_{SFR}), have by far the highest Ly α escape fraction. A strong \sim linear relation is found between Ly α escape fraction and the total gas (HI+H $_2$) depletion time. We argue that the Ly α escape in those galaxies is driven by turbulence in the star-forming gas that shifts the Ly α photons out of resonance close to the places where they originate. We further report on an extreme [C II]158 μm excess in LARS 5, corresponding to $\sim 14\pm 3\%$ of the FIR luminosity, i.e. the most extreme [C II]-to-FIR ratio observed in a non-AGN galaxy to date.

1 Introduction

1.1 Challenges of Lyman Alpha Astrophysics

Already more than fifty years ago, Partridge and Peebles (1967) suggested to search for galaxies at high redshifts using a very narrow spectral window around the (redshifted) Lyman Alpha (hereafter Ly α) hydrogen emission line at 1216 \AA rest wavelength. According to their prediction, bulk of the ionizing photons in young galaxies are ultimately converted to a single line, Ly α , making it the brightest spectral feature, that is holding a substantial fraction of the bolometric flux.

In practice, however, it turned out to be very difficult to find Ly α emitters and it was not until 1981, when Meier and Terlevich (1981) discovered weak Ly α emission in a local blue compact galaxy. It took another 17 years until Cowie and Hu (1998) found a substantial population of Ly α emitters at $z\sim 3.4$. Although the number of high- z galaxies detected through the Ly α line has increased ever since (Ouchi et al., 2008, 2010; Adams et al., 2011; Matthee et al., 2015; Santos et al., 2016; Herenz et al., 2017; Sobral et al., 2018; Urrutia et al., 2019), the decades long endeavour made evident that some physical processes are at play that may suppress or enhance the Ly α emission.

Yet, it is known that resonant scattering of Ly α photons leads to a complex radiative transport problem (Neufeld, 1990; Ahn et al., 2001, 2002; Dijkstra et al., 2006a,b; Verhamme et al., 2006; Schaerer and Verhamme, 2008; Verhamme et al., 2008). The line strength and visibility of Ly α depends on many factors such as dust content (Hayes et al., 2010), dust geometry (Scarlata et al., 2009), neutral gas content (Zheng et al., 2017), kinematics (Kunth et al., 1998; Cannon et al., 2004; Wofford et al., 2013; Pardy et al., 2014) and gas geometry (Tenorio-Tagle et al., 1999; Mas-Hesse et al., 2003; Duval et al., 2014; Jaskot and Oey, 2014). See Hayes (2015) for a review.

While, for example, large scale galaxy winds may enhance Ly α escape via a large velocity gradient along which the photons are shifted to wavelengths less prone to further scattering, dust works in the other direction. Since the resonant nature of the line drastically increases the path length out of the galaxy, the chance for Ly α photons to be destroyed by dust is significantly enhanced. Remarkably, Ly α photons do not appear to diffuse very far in space, because their re-distribution scales are small (Bridge et al., 2018), i.e. Ly α photons get stuck locally over many scattering events. As a result, in some galaxies, the interstellar medium is optically thin even for UV photons (e.g. at a hydrogen column density of 10^{16} cm^{-2}), but opaque for Ly α (Verhamme et al., 2015; Puschnig et al., 2017).

Given the fact that the total escape fraction of Ly α photons depends on such a large variety of effects that all act together in a complex way, predictions of Ly α emission are difficult. However, progress has been made recently (Trainor et al., 2019; Sobral and Matthee, 2019). In particular, Runnholm et al. (2020) reproduced the Ly α output of local Ly α emitters with a dispersion of ~ 0.3 dex only.

One path to remedy this complicated situation is to study the Ly α production and escape mechanisms in a sample of star-forming galaxies on a spatially resolved basis. To do so, *LARS* – the Lyman Alpha Reference Sample – was defined (Hayes et al., 2013, 2014; Östlin et al., 2014). It is a sample of 14 galaxies (see Table 1 for basic properties) which is statistically meaningful enough to observe trends (i.e. it covers a wide range in stellar mass, star formation rate and metallicity) and, most importantly, comparable in selection to galaxies observed at high- z (Ouchi et al., 2008; Cowie et al., 2011). LARS galaxies are selected by two main parameters: UV luminosity and H α equivalent width. The former is comparable to Lyman Break galaxies at redshifts $\sim 3\text{--}4$ and the latter is $> 100\text{\AA}$, limiting the sample to galaxies with currently ongoing (young) bursts of star formation. Multi-band imaging with the Hubble Space Telescope (HST) forms the groundwork of our study which includes HST ultraviolet spectroscopy (Rivera-Thorsen et al., 2015), optical broadband imaging (Micheva et al., 2018), PMAS/LArr IFU data (Herenz et al., 2016), Green Bank Telescope 21 cm spectra (Pardy et al., 2014) and JVLA data (Le Reste et al. in prep.).

1.2 The Kennicutt-Schmidt Relation

The Kennicutt-Schmidt relation or KS law (Schmidt, 1959; Kennicutt, 1998) is key for studies of star formation, because it relates gas surface densities to star formation rate (SFR) surface densities. In its classical form, i.e. *total* gas ($\text{H I} + \text{H}_2$) vs. SFR, the slope is typically found to be non-linear with power-law indices of $\sim 1.4\text{--}1.5$ (Kennicutt, 1998). In contrast, the *molecular* gas relation is often found to be *linear* (e.g. Wong and Blitz, 2002; Bigiel et al., 2008, 2011; Leroy et al., 2008, 2013; Bolatto et al., 2017; Utomo et al., 2018; Colombo et al., 2018), and it holds over eight orders of magnitude in mass, on a wide range of spatial scales – from tens of parsec (Wu et al., 2005) to entire galaxies – and even in low-density disk outskirts of galaxies (Schruba et al., 2011) as well as in low-metallicity dwarf galaxies (Bolatto et al., 2011; Jameson et al., 2016). The observed linear slope has far reaching consequences: 1) the time scale to consume the gas at the current SFR, i.e. $M_{\text{gas}}/\text{SFR}$, or the gas depletion time, is constant and 2) the driving physics behind the KS law is not self-gravity alone (Semenov et al., 2019), but other processes (e.g. feedback) must play a fundamental role as well.

However, non-linear molecular KS relations are also observed, namely on even smaller scales (e.g. Evans et al., 2009, 2014; Heiderman et al., 2010; Gutermuth et al., 2011), in starburst galaxies (e.g. Genzel et al., 2010, 2015), in the dwarf magellanic irregular galaxy NGC4449 (Calzetti et al., 2018) and also in galactic centers (e.g. Leroy et al., 2013).

It was further shown by Gao and Solomon (2004a,b) and Lada et al. (2010) that star formation linearly scales with the *dense gas* traced by HCN (1–0). However, it is still a matter of debate which of these scaling relations (molecular or dense gas) is the more fundamental one. See e.g. Lada et al. (2012) for a discussion. In recent years, however, large efforts have been undertaken to study the dense gas in external galaxies (Bigiel et al., 2016; Jiménez-Donaire et al., 2019), showing that the environment and feedback plays a fundamental role (Kruijssen et al., 2019).

Observations of galaxies at redshifts between 0 and 4 have shown that the level of star formation is mainly dictated by stellar mass, and regulated by secular processes (Popesso et al., 2019). This is seen as a tight relation between stellar mass and SFR, the so called *main sequence of star forming galaxies* (Brinchmann et al., 2004; Noeske et al., 2007; Daddi et al., 2007; Elbaz et al., 2007; Peng et al., 2010; Wuyts et al., 2011; Whitaker et al., 2012, 2014; Tomczak et al., 2016). While the slope of the relation does not vary with redshift, its intercept shifts towards higher SFRs, see for example Wuyts et al. (2011); Rodighiero et al. (2011). However, for main sequence galaxies it was also found that even out to redshift $z \sim 4$ galaxies have constant gas depletion times due to an increase of the gas fraction (Tacconi et al., 2013; Genzel et al., 2015; Scoville et al., 2017). It was also realized that the consumption time scales are too short compared to the age of the Universe. And thus, galaxies must accrete gas, e.g. from the circumgalactic medium or other galaxies by mergers, in order to sustain star formation.

1.3 This Work – KS law for LARS galaxies

In this paper, we establish the KS relation, calculate gas fractions, gas depletion times and star formation efficiencies in the Lyman Alpha Reference Sample. This allows us to study dependencies between previously derived quantities related to the $\text{Ly}\alpha$ emission and global properties of the star forming gas, giving new insights into physical processes and environmental properties that efficiently drive the escape of $\text{Ly}\alpha$ photons.

We have performed low-J CO spectroscopy with the IRAM 30m telescope, far-infrared imaging and spectroscopy with Herschel/PACS and SOFIA/FIFI-LS, targeting continuum and fine structure emission lines of $[\text{C II}]158\mu\text{m}$ and $[\text{O I}]63\mu\text{m}$.

We utilize the aforementioned radio and far infrared observations (see a description of the observations in Section 2) to derive properties of the ISM from dust models (see Section 3.1) and to establish the KS law for LARS galaxies and study the environment, i.e. molecular and total gas fractions, star formation rates and efficiencies, as well as gas depletion times (see Section 4.2). We further use far-infrared photometry and spectroscopy to explore photon-dominated regions (hereafter PDR) within LARS (see Section 4.5), i.e. FUV radiation field and densities. In Section 5 we finally discuss which of the derived properties influence $\text{Ly}\alpha$ escape and bring our results in context with early phases of disk formation.

Throughout the paper, we adopt a cosmology with $H_0=70$, $\Omega_M=0.3$ and $\Omega_{\text{vac}}=0.7$.

Table 1. Compilation of properties of LARS galaxies relevant for this work

ID	z	$\log_{10}M_*$ [M_\odot]	Z [12 + log O/H]	$\log_{10}M_{\text{HI}}$ [M_\odot]	$L_{\text{Ly}\alpha}$ [10^{42}cgs]	$f_{\text{esc}}^{\text{Ly}\alpha}$	D_{scatt} [kpc]	$D_{25\text{SDSS}}$ ["]	b/a_{SDSS}	R_{cutM18} [kpc]	b/a_{M18}
1	0.02782	9.785	8.24	9.3979	0.85	0.119	0.72	14.94	0.69	2.69	0.71
2	0.02982	9.371	8.23	9.4472	0.81	0.521	0.36	25.67	0.43	2.00	0.39
3	0.03143	10.303	8.41	9.8388	0.10	0.003	0.35	85.80	0.22	2.34	0.29
4	0.03249	10.111	8.19	9.8865	0.00	0.000	0.70	19.07	0.89	4.21	0.64
5	0.03375	9.630	8.12	<9.4624	1.11	0.174	0.40	13.11	0.73	2.20	0.71
6	0.03461	9.320	8.08	*<10.3617	0.00	0.000	0.41	20.32	0.60	2.05	0.55
7	0.03774	9.677	8.35	9.4914	1.01	0.100	0.37	19.03	0.48	2.33	0.55
8	0.03825	10.970	8.51	10.3424	1.00	0.025	0.44	30.84	0.59	5.10	1.00
9	0.04677	10.708	8.37	10.1139	0.33	0.007	0.56	7.37	0.86	6.70	0.50
10	0.05765	10.332	8.51	9.6532	0.16	0.026	0.52	22.44	0.43	3.12	0.60
11	0.08461	11.083	8.44	10.415	1.20	0.036	1.56	33.52	0.28	8.40	0.24
12	0.10210	9.870	8.34	–	0.93	0.009	1.03	8.71	0.81	4.44	0.88
13	0.14670	10.772	8.50	–	0.72	0.010	2.24	10.26	0.59	7.40	0.71
14	0.18070	9.243	8.06	–	4.46	0.163	1.68	5.46	0.82	5.03	1.00

The redshifts were derived from radial velocities (given in the optical definition) in Pardy et al. (2014) and are thus related to the H I systemic velocities for all LARS galaxies but 12-14 (which have no H I detection). For those, Pardy et al. (2014) report optical SDSS velocities. Stellar masses ($\log_{10}M_*$), Ly α luminosities ($L_{\text{Ly}\alpha}$) and escape fractions ($f_{\text{esc}}^{\text{Ly}\alpha}$) were previously published by Hayes et al. (2014). The metallicities (Z) derived through the empirical O3N2 relation are taken from Östlin et al. (2014), and atomic gas masses ($\log_{10}M_{\text{HI}}$) from Pardy et al. (2014). *Note that the atomic mass reported for LARS 6 is contaminated by the field spiral UGC10028 and thus only an upper limit. Typical Ly α scattering distances (D_{scatt}) for the galaxies were derived by Bridge et al. (2018) and the radii at which the star formation rate density has decreased to $0.01M_\odot \text{ yr}^{-1} \text{ kpc}^2$ (R_{cutM18}), together with axis ratios (b/a_{M18}) were calculated by Micheva et al. (2018). The blue-band diameters of the 25mag arcsec² isophote ($D_{25\text{SDSS}}$) as well as b/a_{SDSS} were derived from SDSS g-band observations using an SQL query on SDSS DR7. Since the SDSS g-band isophote typically gives sizes that are ~ 1.3 times larger than those measured in the Johnson B band (Hakobyan et al., 2012), we divided the g-band diameters by that factor and report estimated values for $D_{25\text{SDSS}}$ here.

2 Observations and Archival Data

2.1 Observations of Molecular Lines of CO, HCN and HCO⁺

Observations with the IRAM 30m telescope were carried out under programs 082-14, 064-15 and 178-15. Data were acquired during the heterodyne pool weeks in September, October and November 2014 as well as in January and February 2016. Observing runs in visitor mode were carried out in June and September 2015, as well as during May 2016. In total, more than 110h of observing time were scheduled at the telescope, from which roughly 1/3 was lost due to poor weather conditions. Using SFR and metallicity as indicators for the chance to detect CO, we first select 10 galaxies out of our sample for molecular line observations, i.e. we initially rejected LARS 4, 5, 6 and 14 as targets. Finally, we include LARS 5, given the fact that the galaxy has strong winds (Duval et al., 2016) that might trigger molecular gas formation.

Five galaxies out of our sample were detected (simultaneously) in CO (1-0) and CO (2-1) using the *Eight Mixer Receiver* (EMIR). The observed CO lines are shown in Figure 1 on the main beam brightness temperature scale. Beamsizes, main beam efficiencies, Gaussian fit results and flux densities per beam are summarized in Table 2. Note that we also detected CO (1-0) in the companion galaxy of LARS 11. As it is not part of our sample, no analysis was performed. Six LARS galaxies remained undetected down to a baseline r.m.s. level of $\sim 1\text{mK}@20\text{km/s}$, corresponding to a flux density of roughly 5mJy per CO (1-0) beam (see Table 3 and Figure 3). Additionally, in the two galaxies with the strongest CO emission, LARS 3 and 8, HCN and HCO⁺ (1-0) were detected, however at signal-to-noise ratios of $\sim 3-6$ only.

Additional CO (3-2) observations of two galaxies were carried out with APEX, the *Atacama Pathfinder Experiment* (Güsten et al., 2006) within the Swedish time allocation during periods P94 and P96 under project codes F-9340A-2014 and F-9329A-2015. LARS 8 was detected in CO (2-1) and (3-2) and LARS 13 was detected in CO (3-2) using the *Swedish heterodyne Facility Instrument* (Belitsky et al., 2006; Vassilev et al., 2008).

All molecular scans (IRAM 30m and APEX) were obtained in wobbler-switching mode and the calibrated data was reduced using GILDAS/CLASS¹, a collection of state-of-the-art software oriented toward (sub-)millimeter radioastronomical applications. IRAM scans obtained with the Fast Fourier Transform Spectrometer (FTS) unit were corrected for platforming. In our pipeline, we initially chose a wide constant line window ranging from -300 to +300 km/s around the expected zero-velocity position of the line, extract a range of -1000 to +1000 km/s and applied a linear baseline correction on each individual scan. In the next step, we masked spikes and then examined plots of system temperature and r.m.s. noise for all scans, which we used to filter scans that do not follow the radiometer equation. Scans that were obtained under conditions of high precipitable water vapor, i.e. when the atmospheric transmission at the given frequency was lower than ~ 33 percent, were excluded from further processing. The remaining scans per galaxy were average stacked and re-sampled to a resolution of 1 km/s. From that point on, each galaxy was manually processed using individual line windows, baseline fits and smoothing to resolutions between 5 and 56 km/s per channel. Gaussian fits were performed to reveal velocity components. Total fluxes were derived via summation of channels along the line window. Errors on the fluxes are the r.m.s. times the number of channels along the window.

2.2 Infrared Observations

2.2.1 Herschel PACS Observations

Far infrared observations of LARS galaxies (2, 4, 6, 8, 9) were executed with the *Photoconductor Array Camera and Spectrometer* (PACS Poglitsch et al., 2010) on board the *Herschel Space Observatory* (Pilbratt et al., 2010) under program OT2_mhayes_4, for a total time of 12.1 hours. Our observations were carried out in the standard single pointing chop-nod mode. PACS was operated in parallel mode (using the photometer and spectrometer simultaneously), targeting photometry at 70, 100 and 160 μm as well as spectral lines of [O I]63 μm , [O III]88 μm and [C II]158 μm . The point spread function (PSF) is well described by a two dimensional Gaussian with sizes of roughly 6x12, 7x13 and 12x16 arcsec for the blue, green and red channel respectively.

Further PACS imaging of LARS galaxies is found in the archive. LARS 3 was observed under the guarantee time key program KPGT_esturm_1 (PI: Eckhard Sturm) as part of a comprehensive far-infrared survey of infrared bright galaxies. LARS 5 was observed in program OT2_dhunter_4 (PI: Deidre Hunter), as part of an investigation of dust and

¹<http://www.iram.fr/IRAMFR/GILDAS>

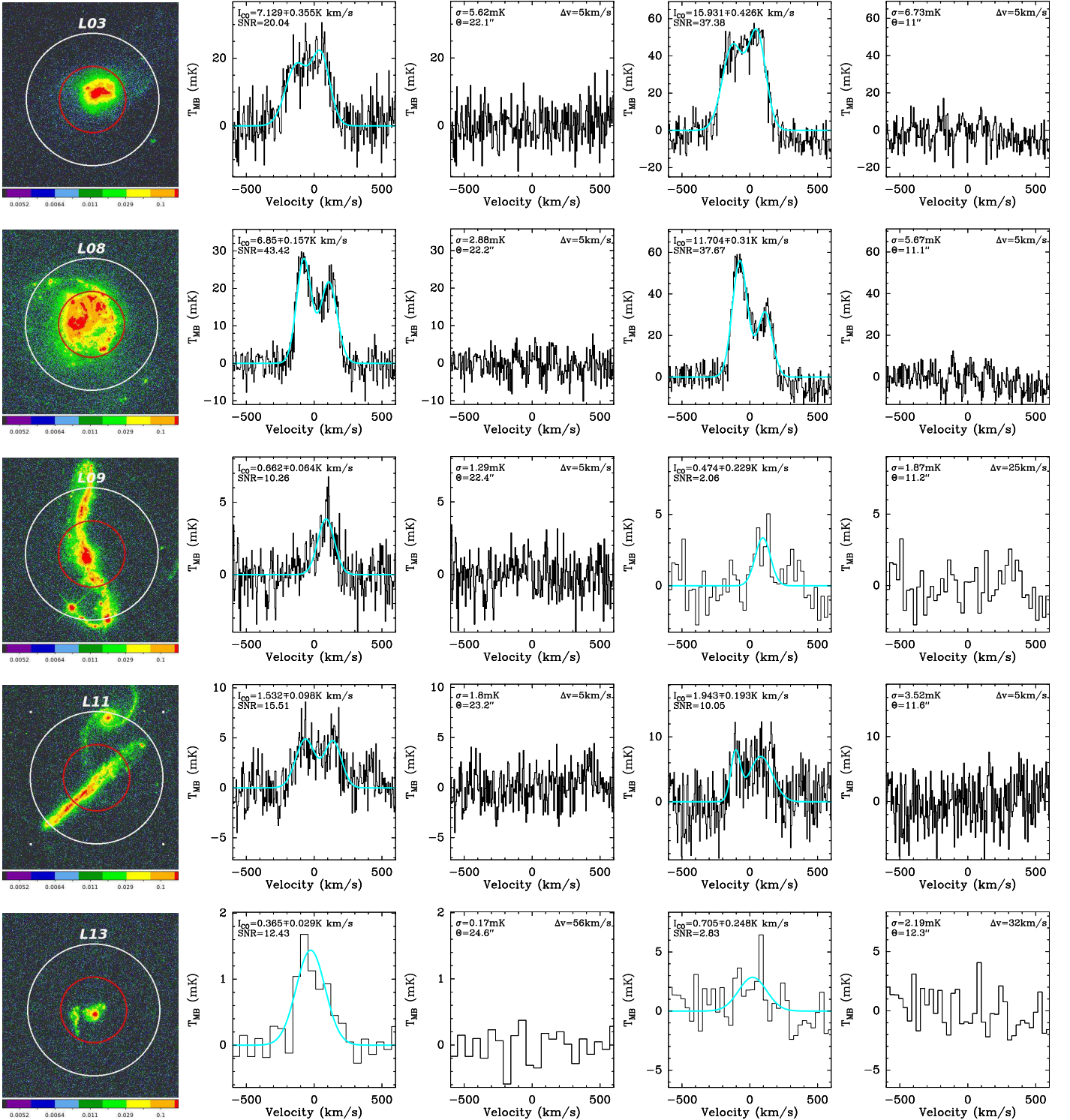
Table 2. Summary of the detected molecular lines

ID	line	B_{eff}	θ [arcsec]	t_{on} [h]	v_{peak} [km/s]		FWHM [km/s]		SNR	I_{mb} [K km/s]	S [Jy km/s]
3	CO(1-0)	0.79	22.10	0.6	49.6 [17.6]	-129.8 [26.4]	157.7 [29.35]	190.7 [41.43]	20.0	7.13±0.36	35.6±1.8
3	CO(2-1)	0.58	11.00	0.6	-127.2 [10]	53.1 [7.9]	178.3 [16.13]	152.9 [12.2]	37.4	15.93±0.43	79.6±2.1
3	HCN(1-0)	0.84	28.70	1.3	-40.3 [51.5]			623.7 [126.79]	7.0	1.06±0.15	5.3±0.8
3	HCO+(1-0)	0.84	28.60	1.3	-64.4 [56.7]			556.4 [136.97]	6.1	1.08±0.18	5.4±0.9
8	CO(1-0)	0.80	22.20	3.2	-75.8 [2.8]	108.4 [3.9]	127 [6.17]	144.7 [8.16]	43.4	6.85±0.16	34.2±0.8
8	CO(2-1)	0.59	11.10	3.4	-68 [0.2]	118.9 [2.6]	139.1 [4.04]	114.9 [5.82]	37.7	11.7±0.31	58.5±1.6
8	CO(3-2)	0.73	18.50	0.9	-59.8 [4.4]	124.6 [4.7]	148.7 [10.45]	118.5 [10.19]	29.8	6.5±0.22	203.1±6.8
8	HCN(1-0)	0.84	28.90	3.2	-121.9 [26.5]			151.8 [47.73]	4.0	0.29±0.07	1.5±0.4
8	HCO+(1-0)	0.84	28.70	3.2	-30.9 [36.1]	0 [0]		216.4 [98.46]	3.2	0.19±0.06	0.9±0.3
9	CO(1-0)	0.80	22.40	6.9		90 [5.6]		143.1 [17.01]	9.9	0.66±0.07	3.3±0.3
9	CO(2-1)	0.59	11.20	4.5		97.1 [19.5]		130.9 [40.19]	3.0	0.51±0.17	2.6±0.8
11	CO(1-0)	0.80	23.20	3.1	-64.9 [15.8]	139.1 [14.8]	165.6 [29.89]	149.2 [39.68]	15.5	1.53±0.1	7.7±0.5
11	CO(2-1)	0.60	11.60	1.4	-85 [3.6]	101.8 [9.7]	123.6 [16.35]	159.6 [16.24]	10.1	1.94±0.19	9.7±1.0
13	CO(1-0)	0.82	24.60	4.0	-20.2 [21.3]			256.1 [50.78]	11.3	0.38±0.03	1.9±0.2
13	CO(2-1)	0.63	12.30	3.3		42.6 [33]		242.9 [79.22]	6.1	0.62±0.1	3.1±0.5
13	CO(3-2)	0.73	20.50	5.4		-11 [24.1]		320.8 [65.29]	6.2	0.52±0.08	16.2±2.6

For each transition, we show the beam efficiency B_{eff} that was used to translate the antenna temperature to the T_{mb} scale, the beam size θ , the total effective on-source observing time (after processing and filtering) T_{on} as well as results from Gaussian fits and fluxes. v_{peak} is the velocity (with respect to systemic velocity of H I) at the Gaussian peak brightness temperature with the error on v_{peak} in square brackets (in cases with more than one Gaussian fit, v_{peak} is given for each component), FWHM is the full-width-at-half-maximum calculated from the Gaussian sigma value(s) and SNR is the signal-to-noise ratio. The velocity-integrated source brightness temperatures on the main beam brightness temperature scale as well as velocity-integrated flux densities are indicated by I_{mb} and S respectively.

Table 3. Summary of LARS galaxies not detected in CO

ID	Beff	HPBW [arcsec]	t_{on} [h]	$\sigma_{\text{rms},20\text{km/s}}$ [mK]	$\sigma_{\text{rms},20\text{km/s}}$ [mJy]
1	0.79	22.0	3.40	1.01	5.06
2	0.79	22.0	1.90	1.38	6.93
5	0.79	22.1	3.55	0.77	3.88
7	0.80	22.2	5.70	0.68	3.42
10	0.80	22.6	1.05	1.71	8.57
12	0.81	23.6	2.30	0.90	4.54



(1) H α & HPBW

(2) CO (1-0)

(3) residual

(4) CO (2-1)

(5) residual

Figure 1. CO (1-0) and (2-1) emission lines of LARS galaxies obtained with the IRAM 30m telescope, shown on the T_{MB} scale in mK. The beamsizes for the transitions are shown in column (1) on top of our HST H α narrowband images: *white*: CO (1-0) and *red*: CO (2-1). CO (1-0) and CO (2-1) spectra are shown in columns (2) and (4) respectively. Single- or double-Gaussian fits were performed for calculating the line flux. They are shown as cyan solid lines. The residuals after subtraction of the fits from the data are given in columns (3) and (5).

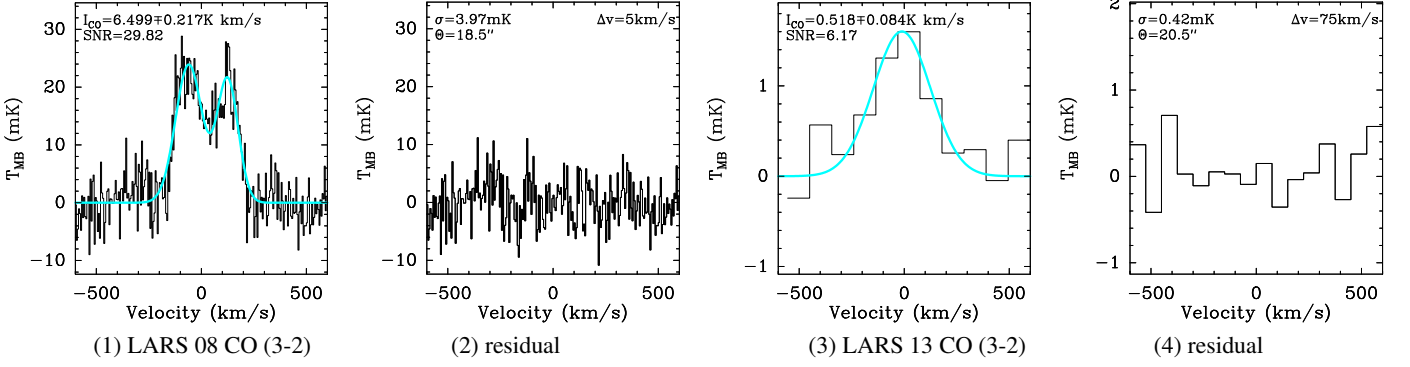


Figure 2. Detections of CO (3-2) with APEX/SHeFI for LARS 8 (*column 1*) and 13 (*column 3*). Spectra are shown on the T_{MB} scale in mK. Single- or double-Gaussian fits were performed for calculating the line flux. They are shown as cyan solid lines. The residuals after subtraction of the fits from the data are shown in panels (2) and (4).

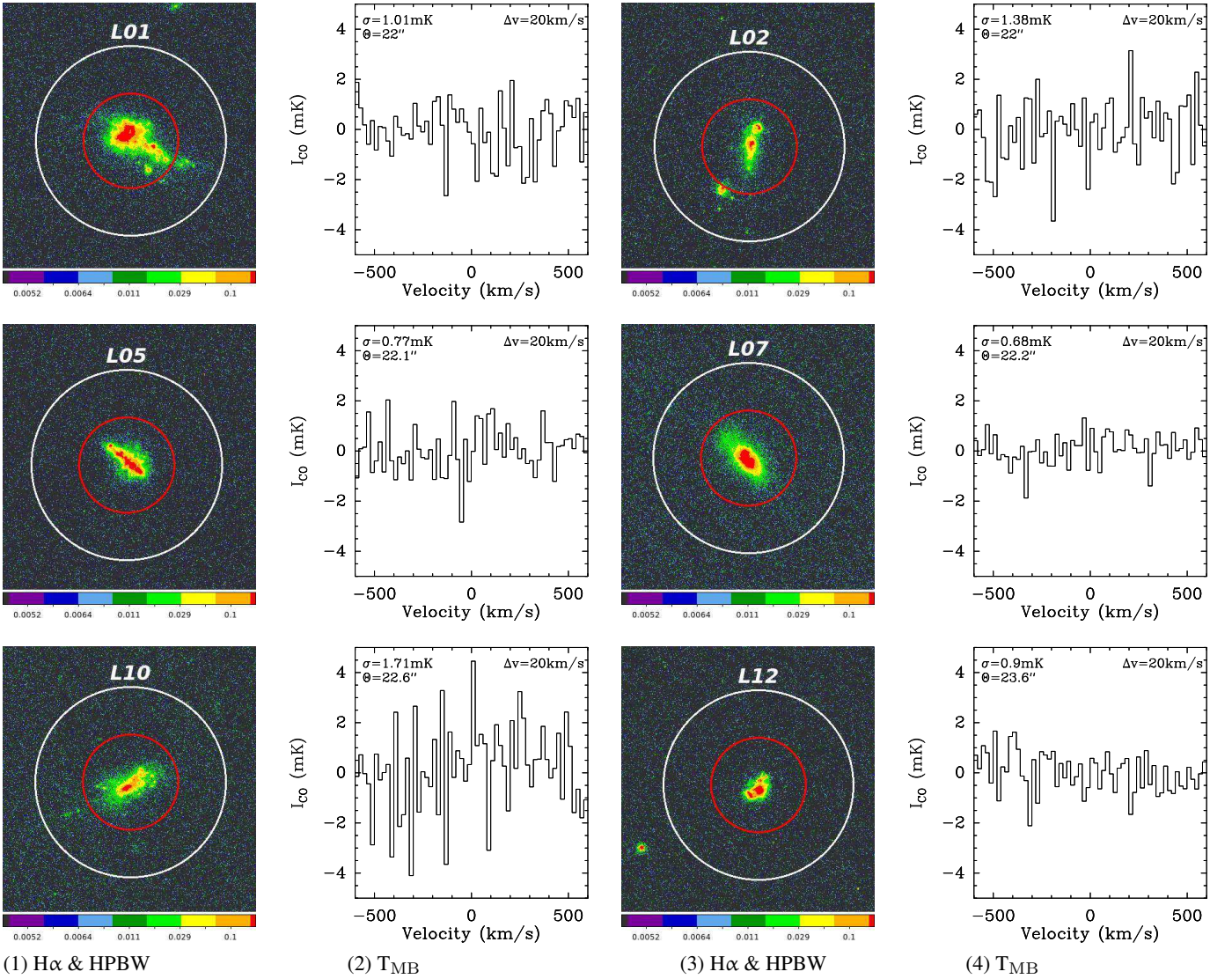


Figure 3. CO (1-0) nondetections of LARS galaxies. The beamsize for the CO (1-0) transition is shown in columns (1) and (3) as white circle on top of our HST H α narrowband images. The measured signals on the main beam brightness temperature scales are shown in columns (2) and (4).

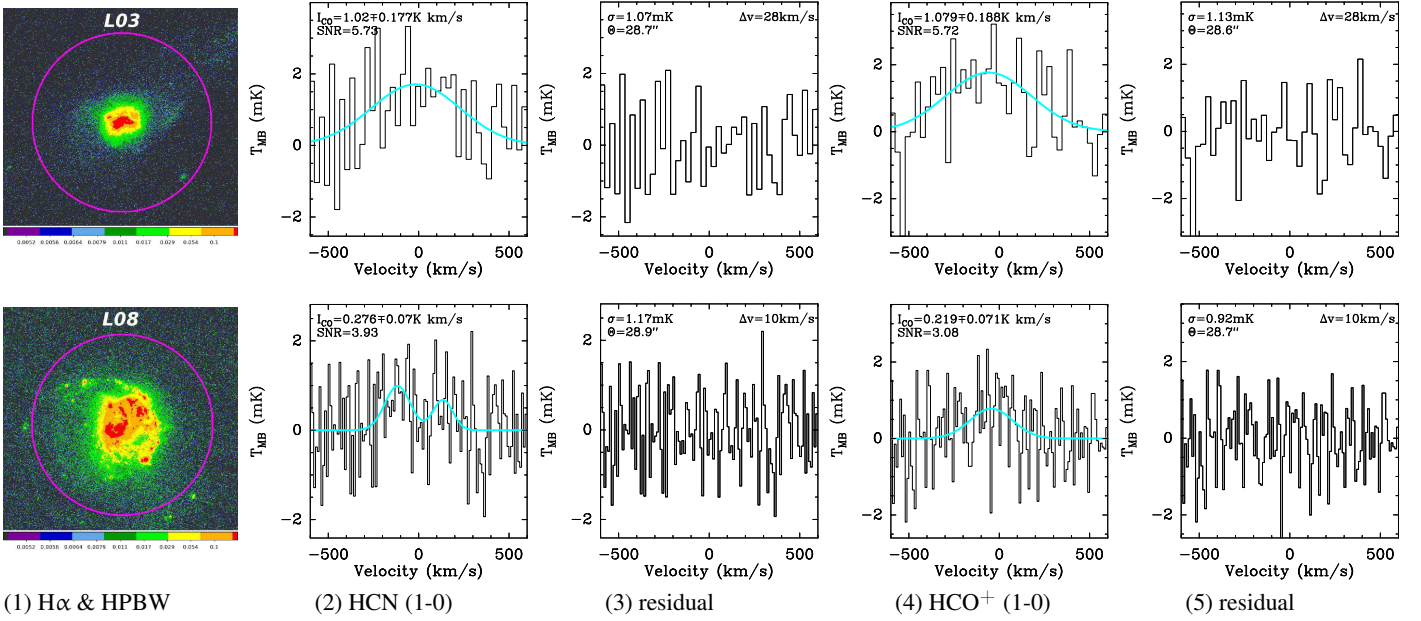


Figure 4. Detections of dense gas tracers in LARS 3 (*top row*) and 8 (*bottom row*). The beamsizes for the transitions are shown in column (1) on top of our HST H α narrowband images. HCN and HCO⁺ (1-0) spectra are shown in columns (2) and (4). Spectra are given on the T_{MB} scale in mK. Single- or double-Gaussian fits were performed for calculating the line flux. They are shown as cyan solid lines. The residuals after subtraction of the fits from the data are shown in columns (3) and (5).

star formation in local low metallicity galaxies. LARS 7 and 10 are covered by program KPOT_seales_01_2, the *Herschel Thousand Degree Survey* (PI: Stephen Eales). LARS 12, 13 and 14 were observed as part of a survey of local Lyman Break Analogues under program OT1_roverzie_1 (PI: Roderik Overzier).

All PACS imaging data was reduced using the *Herschel Interactive Processing Environment* (HIPE; (Ott, 2010)) version 14.0.1. To create a set of homogeneous images of our galaxies, we re-reduce all observations starting from level 1 data products. The mapping was performed using the MADMap maximum likelihood code for LARS 7 and 10 and JScanam otherwise. Due to the different observations available for the galaxies, our final reduction levels range from 2.0 to 3.0, where level 2.0 indicates a fully reduced dataset, level 2.5 is the result of combining pairs of observations acquired in the scan and cross-scan mode, and level 3.0 are mosaics of level 2.5 products that belong to the same sky field and observing program. A summary of the photometric PACS observations used in this paper is shown in Table 4.

In order to measure the fluxes of our galaxies, we have used the *Daophot* algorithm as implemented in the *annularSkyAperturePhotometry* task of HIPE’s Jython console. We also examined source sizes and flux measurements using the *sourceFitting* task. However, since most of our sources are not or only marginally resolved, in particular in the red channel, we finally used the results from the aperture photometry, with an aperture correction factor applied. Our flux measurements are summarized in Table 6.

PACS spectroscopic data of our observing program was not re-reduced, instead we use the level 2.0 data products provided through the standard PACS spectrometer pipeline. The fluxes of the spectral lines were derived after summation over all spaxels and subsequent fitting of the continuum and the Gaussian line. The continuum subtracted line fluxes are then found from the area below the Gaussian fits. A summary of the measurements is shown in Table 5.

2.2.2 SOFIA FIR Line Spectroscopy

We performed observations of LARS galaxies targeting FIR fine structure lines of [C II]158 μm , [O I]63 μm and [O III]88 μm with the *Far Infrared Field-Imaging Line Spectrometer* (FIFI-LS) aboard the Stratospheric Observatory for Infrared Astronomy (SOFIA) airplane (see Figures 5, 6 and 7). Observations were carried out in Cycle 3 under project 03_0059.

Basic data calibration was provided by the FIFI-LS team, i.e. level 3 data products, consisting of ~ 30 second exposures. The data was further processed using the same method as described in Smirnova-Pinchukova et al. (2019), i.e. an additional selection routine and background subtraction. Final data cubes with a sampling of 6" are produced

Table 4. Summary of PACS data used in this paper

ID	PACS Obsid	Proposal Code	Reduction Level
2	1342270859	OT2_mhayes_4	2.0
3	1342209025,1342209027	KPGT_esturm_1	3.0
4	1342247700	OT2_mhayes_4	2.0
5	1342253524,1342253526	OT2_lhunt_4	3.0
6	1342261848,1342262223	OT2_mhayes_4	3.0
7	1342210558,1342210903, 1342210946,1342210963, 1342222626	KPOT_seales01_2	3.0
8	1342248630	OT2_mhayes_4	2.0
9	1342270829,1342270830	OT2_mhayes_4	3.0
10	1342210567,1342210963, 1342222626	KPOT_seales01_2	3.0
12	1342231634,1342231636	OT1_roverzie_1	3.0
13	1342237833,1342223573	OT1_roverzie_1, GT1_aconturs_1	2.5
14	1342231640,1342231642	OT1_roverzie_1	3.0

Table 5. Summary of Gaussian fit results for the PACS and FIFI-LS spectral lines of [C II]158, [O I]63 and [O III]88

ID	line	center [km s ⁻¹]	FWHM [km s ⁻¹]	flux [10 ⁻¹⁵ erg s ⁻¹ cm ⁻²]	instrument
2	[C II]158	-20	209	8.4±4.0	PACS
2	[O I]63	177	<572	<30.3	PACS
3	[C II]158	-52	398	688.0±15.6	PACS
3	[O I]63	3	380	1317.0±63.8	PACS
3	[O III]88	-43	440	843.8±54.7	PACS
5	[C II]158	-117	584	479.1±84.7	FIFI-LS
5	[O III]88	-110	>222 [†]	254.9±43.3	FIFI-LS
8	[C II]158	-20	497	1052.0±161.3	FIFI-LS
9	[C II]158	105	284	285.7±5.7	PACS
9	[O I]63	153	218	249.3±23.1	PACS
11	[C II]158	-118	388	502.3±30.5	FIFI-LS
12	[C II]158	38	214	14.5±2.1	PACS
12	[O I]63	134	212	20.1±6.0	PACS
13	[C II]158	-18	299	30.8±3.1	PACS
13	[O I]63	127	280	36.6±7.7	PACS

[†] Due to strong atmospheric absorption, the red side of the line is truncated and the reported value is considered to be a lower limit.

Also note that the spectral resolution varies between the different instruments and channels. PACS offers spectral resolutions of ~240 km/s for the [C II]158μm observations and ~100 km/s for [O I]63μm. FIFI-LS has R~1200 (~250 km s⁻¹) for the observed wavelength of [C II]158μm and R~670 (~450 km s⁻¹) for [O III]88μm.

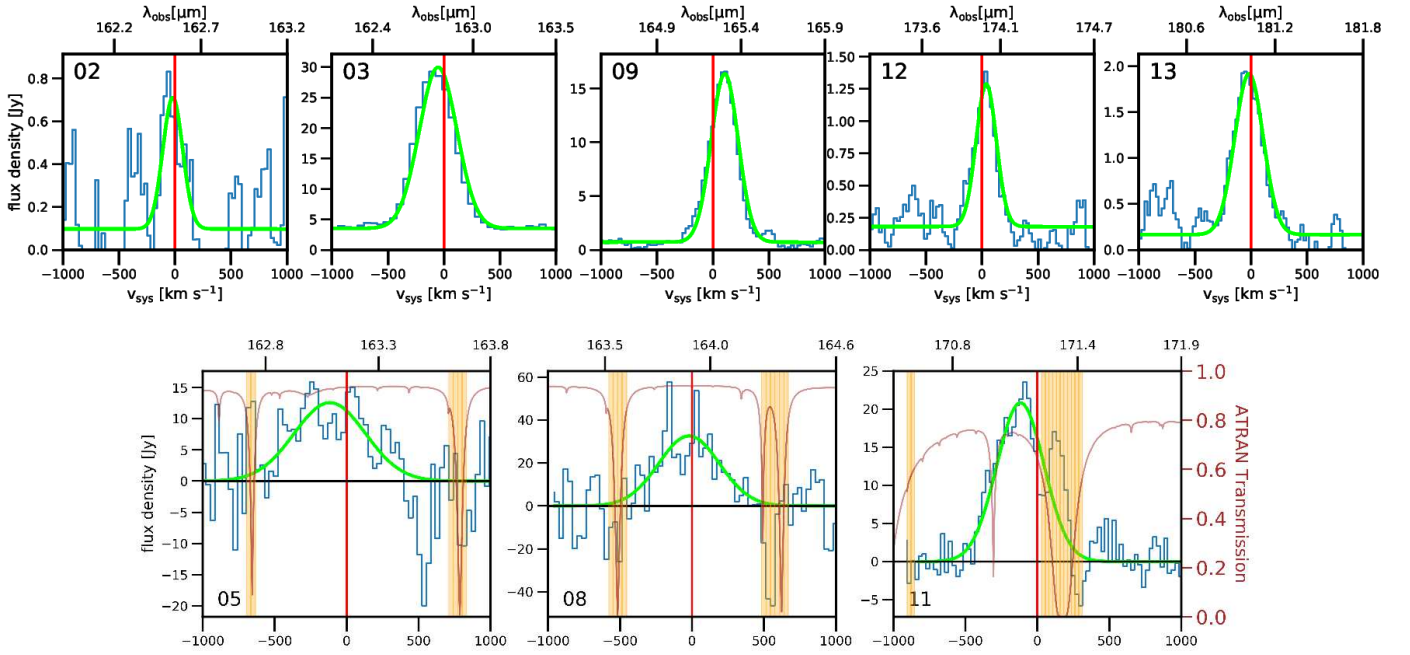


Figure 5. [C II]158 μ m fine structure lines of LARS galaxies. Herschel/PACS spectra are shown in the top row, and SOFIA/FIFI-LS spectra in the bottom row. Total fluxes were derived using Gaussian fits (see Table 5). For FIFI-LS data, the atmospheric absorption, calculated using ATRAN (Lord, 1992), is shown as red curve. Spectral ranges with strong atmospheric absorption (see orange range) were masked out for the fitting process. The zero-velocity (red vertical line) is related to the H I systemic velocity from Pardy et al. (2014) for all LARS galaxies but LARS 12-14 (which have no H I detection). For those, the systemic velocity is based on SDSS optical redshifts.

with the Drizzle algorithm (Fruchter and Hook, 2002). Total line fluxes were calculated using Gaussian fits to the summed spectra within an aperture of 36". Spectral ranges with strong atmospheric absorptions were masked out for the fitting process. A summary of the measurements is shown in Table 5. Note that the spectral resolution varies between the channels, with $R \sim 1200$ ($\sim 250 \text{ km s}^{-1}$) for the observed wavelength of [C II]158 μ m and $R \sim 670$ ($\sim 450 \text{ km s}^{-1}$) for [O III]88 μ m.

2.2.3 unWISE Source Extractions

NASA's Wide-field Infrared Survey Explorer (WISE; Wright et al. (2010) mapped the sky at 3.4, 4.6, 12, and 22 μ m (W1, W2, W3, W4) in 2010 with an angular resolution of 6.1, 6.4, 6.5 and 12.0 arcsec respectively. We checked the WISE all-sky source catalog for entries of our targets. Unfortunately, photometry was not available for all LARS

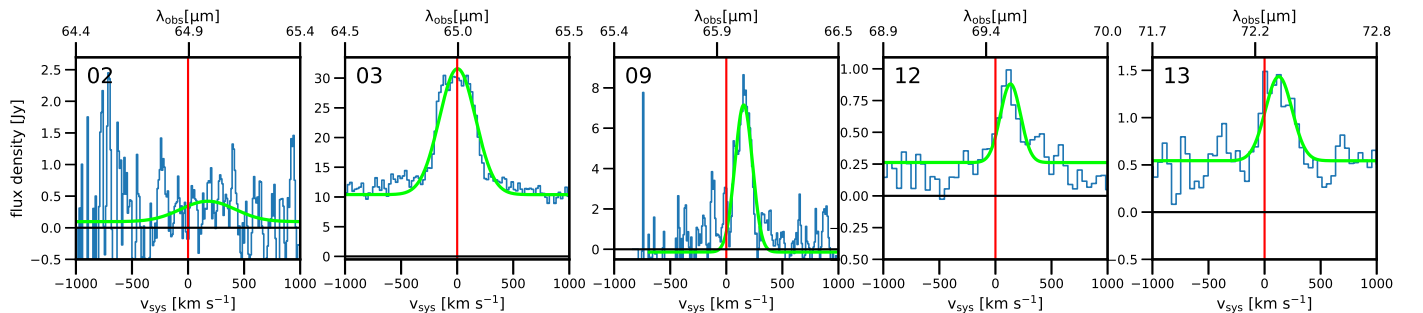


Figure 6. [O I]63 μ m fine structure lines of LARS galaxies, obtained with Herschel/PACS. Total fluxes were derived using Gaussian fits (see Table 5). The zero-velocity (red vertical line) is related to the H I systemic velocity from Pardy et al. (2014) for all LARS galaxies but LARS 12-14 (which have no H I detection). For those, the systemic velocity is based on SDSS optical redshifts.

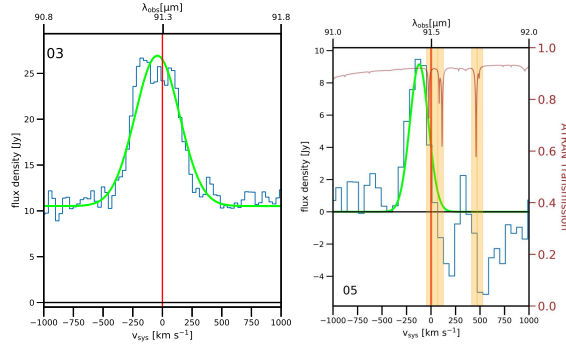


Figure 7. [O III]88 μ m fine structure lines of LARS 3 (*left*) and 5 (*right*), obtained with Herschel/PACS and SOFIA/FIFI-LS respectively. Total fluxes were derived using Gaussian fits (see Table 5). For FIFI-LS data, the atmospheric absorption, calculated using ATRAN (Lord, 1992), is shown as red curve. Spectral ranges with strong atmospheric absorption (see orange range) were masked out for the fitting process. The zero-velocity (red vertical line) is related to the H I systemic velocity from Pardy et al. (2014).

Table 6. WISE and Herschel/PACS photometric measurements of LARS galaxies

ID	W1	W2	W3	W4	P70	P100	P160
	[mJy]	[mJy]	[mJy]	[mJy]	[mJy]	[mJy]	[mJy]
1	1.7 \pm 0.1	1.2 \pm 0.1	14.1 \pm 0.4	97.3 \pm 3.1	–	–	–
2	0.5 \pm 0.1	0.2 \pm 0.1	1.0 \pm 0.3	4.5 \pm 1.5	80 \pm 11	–	121 \pm 14
3	15.5 \pm 0.1	16.7 \pm 0.2	236.3 \pm 3.6	1586.5 \pm 24.0	9306 \pm 8	8628 \pm 7	4745 \pm 19
4	2.0 \pm 0.2	1.4 \pm 0.1	12.5 \pm 0.5	79.9 \pm 2.5	474 \pm 8	–	331 \pm 11
5	0.5 \pm 0.1	0.5 \pm 0.1	4.5 \pm 0.7	29.1 \pm 5.5	113 \pm 5	117 \pm 4	40 \pm 4
6	0.4 \pm 0.2	0.4 \pm 0.2	–	–	51 \pm 8	24 \pm 8	58 \pm 10
7	0.9 \pm 0.1	0.8 \pm 0.1	8.1 \pm 0.5	51.9 \pm 2.1	–	303 \pm 78	309 \pm 50
8	16.1 \pm 0.1	11.3 \pm 0.1	108.7 \pm 1.2	323.5 \pm 3.3	–	4322 \pm 27	3346 \pm 34
9	2.3 \pm 0.5	4.0 \pm 0.1	36.2 \pm 0.6	171.6 \pm 4.1	1147 \pm 17	1415 \pm 20	1306 \pm 27
10	1.0 \pm 0.1	0.8 \pm 0.2	3.4 \pm 0.6	9.3 \pm 3.2	–	336 \pm 77	413 \pm 50
11	4.1 \pm 0.3	3.1 \pm 0.1	27.9 \pm 0.7	56.7 \pm 4.9	–	–	–
12	0.3 \pm 0.2	0.3 \pm 0.1	2.8 \pm 0.6	17.4 \pm 3.5	104 \pm 4	113 \pm 6	62 \pm 4
13	0.6 \pm 0.1	1.1 \pm 0.2	10.6 \pm 0.7	39.7 \pm 4.5	506 \pm 3	464 \pm 3	286 \pm 3
14	0.2 \pm 0.1	0.1 \pm 0.1	0.3 \pm 0.2	2.8 \pm 0.7	16 \pm 2	12 \pm 1	–

galaxies. Thus, we performed source extraction using SExtractor (Bertin and Arnouts, 1996) on unWISE² (Lang, 2014) images, which are unblurred coadds of the original WISE imaging. For the extraction, we used the provided weight maps as RMS maps, applied Gaussian filters to the W3 and W4 bands in order to smooth the irregular PSFs, and used an RMS-based absolute detection threshold. For those LARS galaxies that are unresolved, and have a WISE catalog entry, we find that our extracted flux levels (FLUX_AUTO) agree to a level better than 10 percent compared to the catalog’s profile fitting magnitude (mpro). We convert the derived magnitudes to flux densities using W1-W4 zero magnitude fluxes³ of 309.54, 171.787, 31.674 and 8.363 Jy. The photometric results for the LARS galaxies in units of mJy are summarized in Table 6.

2.2.4 IRIS Photometry

Only six LARS galaxies were found in the Infrared Astronomical Satellite (IRAS) point source catalogue (PSC) and the faint source catalogue (FSC). Therefore, we have downloaded images of the improved reprocessing of the IRAS Survey (IRIS⁴), and performed photometric flux measurements for all LARS galaxies using these data products. The originally

²<http://unwise.me/>

³http://wise2.ipac.caltech.edu/docs/release/allsky/expsup/sec4_4h.html

⁴http://irsa.ipac.caltech.edu/data/IRIS/index_cutouts.html

Table 7. IRAS (I) and AKARI (A) photometric measurements of LARS galaxies

ID	I12	I25	I60	I100	A65	A90	A140	A165
	[mJy]	[mJy]	[mJy]	[mJy]	[mJy]	[mJy]	[mJy]	[mJy]
1	–	–	810±257	–	–	384±146	–	–
3	307±108	1694±203	11461±733	15350±4109	7663±1054	9249±485	3311±200	1552±251
4	–	–	–	–	–	321±197	218±148	–
6	–	–	–	–	–	–	222±163	–
8	–	–	4096±464	10633±4930	1488±617	3593±689	3769±1786	3441±2531
9	–	–	1085±209	1979±907	–	1022±246	–	–
11	–	–	505±209	1929±1057	–	810±272	859±155	–
13	–	–	–	–	–	298±194	–	–

downloaded IRIS images cover fields of two square degree (NASA’s *Montage* tool⁵ was used to create smaller cutouts). The full width at the half maximum of the point spread function in the new images is 3.8, 3.8, 4.0 and 4.3 arcmin for the four IRAS bands of 12, 25, 60 and 100 μ m. All LARS galaxies are thus unresolved. After conversion from MJy/sr to mJy/px, flux densities were extracted using *SExtractor*’s (Bertin and Arnouts, 1996) FLUX_AUTO value. The results are shown in Table 7.

2.2.5 AKARI Photometry

We also checked the archive of the AKARI (Murakami et al., 2007) infrared satellite mission for LARS galaxy data. AKARI comprises two main instruments with 13 spectral bands in total covering a wavelength range of 1.8 to 180 μ m. For our purpose we focused on the four FIS (Far-Infrared Surveyor; (Kawada et al., 2007)) bands with central wavelengths of 65, 90, 140, and 160 μ m. Only three LARS galaxies fluxes were published in the FIS Bright Source Catalogue Ver. 2.0 (released April 2016), so we downloaded cutouts of the AKARI Far-infrared All-Sky Survey Maps (Doi et al., 2015; Takita et al., 2015). The originally downloaded images cover fields of six degree (NASA’s *Montage* tool⁵ was used to create smaller cutouts). The full width at the half maximum of the PSF in these maps is roughly 60 arcsec for the 65 and the 90 μ m bands and 90 arcsec for the 140 and 160 μ m bands. All LARS galaxies are thus unresolved. After conversion from MJy/sr to mJy/px, flux densities were extracted using *SExtractor*’s (Bertin and Arnouts, 1996) FLUX_AUTO value. The results are summarized in Table 7.

2.3 Previously Derived Lyman Alpha Related Quantities

2.3.1 Lyman Alpha Escape Fraction and Scattering Length

Hayes et al. (2014) have computed the Ly α escape fractions of LARS galaxies in the following way. Assuming case B recombination theory, the observed Ly α flux was compared to that expected from extinction corrected H α . Note that H α was obtained through HST narrowband imaging, i.e. capturing all of the ionized gas. Adopting an intrinsic value of Ly α _{intrinsic}/H α =8.7, the escape fraction was calculated as Ly α _{obs}/Ly α _{intrinsic}.

The Ly α scattering lengths of LARS galaxies were published by Bridge et al. (2018). They are derived from modeling the Ly α morphology based on H α images, which again when multiplied by 8.7 should give the approximate intrinsic morphology of Ly α . The scattering is then modeled using a Gaussian convolution, with an additional component of dust attenuation (from H α /H β). Using the MCMC method, the observed Ly α image is re-produced and the scattering length is found from the size of the best-fit Gaussian convolution kernel.

⁵<http://montage.ipac.caltech.edu/>

3 Methods

3.1 Dust Based Gas Masses

Given that we could detect only one third of the LARS sample in CO (1-0), we employ the models⁶ of Draine and Li (2007) to derive dust masses, which finally enables us to infer the total gas masses for all LARS galaxies in a homogeneous way. The models predict infrared spectra for wavelengths between 1 μm and 1 cm. They are based on a mixture of dust grains containing carbonaceous grains (including PAHs) and amorphous silicates, with grain size distributions – or extinction curves – as found in the Milky Way (MW), the Large Magellanic Cloud (LMC) and the Small Magellanic Cloud (SMC). Within each distribution type (MW, LMC or SMC), a variety of PAH dust mass fractions q_{PAH} is implemented, ranging from 0.1% to 4.6%, with the lowest and highest q_{PAH} value being consistent with observations of the dust in the SMC and Milky Way, respectively. The total power radiated per H-nucleon per unit frequency per steradian, j_ν , then depends on two radiative components: 1) the average stellar intensity found in the diffuse ISM, described by the energy density parameter U_{min} , and 2) a fraction γ of dust mass that is exposed to a power law distribution of intensities ranging from U_{min} to U_{max} with a power law slope $\alpha = -2$. The latter component is related to photodissociation regions (hereafter PDRs). U is a scale factor to the local Galactic interstellar radiation field estimated by Mathis et al. (1983), and can be related to the Habing (1968) field G_0 via $U = 0.88G_0$. The final value of j_ν is given by a linear combination of the two components with a $(1 - \gamma)$ mass fraction that is originating from dust exposed to the average, diffuse stellar intensity and a fraction γ related to the currently ongoing star formation, with $0 \leq \gamma \leq 1$. Thus, the fraction of dust mass associated with PDR regions is given by the product of γ and M_{dust} .

Another parameter included in the models is the solid angle subtended by (old) stars, Ω_* , since they also contribute to the overall emission spectrum, albeit mainly at wavelengths of few μm , which is at the low end of the range we are considering. Assuming an average stellar surface temperature T of 5000K, their share is calculated through the Planck function $B_\nu(T)$.

In the analysis that follows we keep the upper energy density cutoff U_{max} fixed at a value of 10^6 , which decreases the number of degrees of freedom by 1, while having only little influence on the fitting result, as shown by Draine et al. (2007). Hence, we are left with five free parameters for the models: q_{PAH} , U_{min} , γ , M_{dust} and Ω_* .

We derive those quantities for LARS galaxies using Bayesian inference, similar to the method described in Galliano (2018). Our logarithmic prior is set to a constant (0.0) within the following intervals for our parameters: U_{min} : 0.1-25, q_{PAH} : 0.1-4.6%, M_{dust} : 10^6 - $10^9 M_\odot$, γ : 10^{-3} - $10^{-0.1}$ and Ω_* : 10^{-10} - 10^{-7} sterad. Outside these intervals, the prior is set to negative infinity. Using the photometric data from WISE, Herschel/PACS, AKARI and IRAS allows us to infer the logarithmic likelihood for the whole parameter space. Note that – beside the measured photometric error – a 10-percent model-based error is also included when calculating the logarithmic likelihood of the parameter space. The latter is explored through the Markov-Chain Monte Carlo (MCMC) method as implemented in the Python package `emcee` (version 3.0.2). The final joint posterior probability distribution of the derived parameters is shown in Appendix A. The best-fit SED was found from the 50% quantile of the logarithmic posterior distribution and the uncertainties are derived from a quantile-based credible interval corresponding to 16% and 84% (i.e. $\pm 1\sigma$). A summary of the derived quantities is found in Table 8, where also the number of degrees of freedom (ν) is denoted.

The dust masses are finally converted into total gas mass estimates ($M_{\text{gas,est}}$) using a metallicity-dependent gas-to-dust ratio as described in the following section.

3.1.1 Metallicity-Dependent Gas-to-Dust Ratio

Once the dust masses are calculated, we convert them into total gas masses using a metallicity-dependent gas-to-dust ratio (hereafter GDR). GDR is found to scale with Z^{-1} at near-solar metallicities (Lisenfeld and Ferrara, 1998; Hirashita et al., 2002; James et al., 2002; Hunt et al., 2005; Draine et al., 2007; Engelbracht et al., 2008; Galliano et al., 2008; Muñoz-Mateos et al., 2009; Bendo et al., 2010; Galametz et al., 2011; Magrini et al., 2011; Sandstrom et al., 2013; Rémy-Ruyer et al., 2014; Roman-Duval et al., 2014; Cortese et al., 2016; Kahre et al., 2018). However, this trend is not seen in low-metallicity dwarf galaxies, which show higher GDRs than expected (Lisenfeld and Ferrara, 1998; Galliano et al., 2003, 2005, 2011; Galametz et al., 2011; Rémy-Ruyer et al., 2014; Kahre et al., 2018). Given the generally low metal content of LARS galaxies, ranging from $\sim 13\%$ solar to $\sim 2/3$ solar, we adopt a

⁶<ftp://ftp.astro.princeton.edu/draine/dust/irem4/>

Table 8. Results from Bayesian inference of Draine & Li (2007) dust model parameters for LARS galaxies

ID	q_{PAH}	$\log(\Omega_*)$ [sr]	U_{min} ($U = 0.88G_0$)	$\log(\gamma)$	$\log(M_{\text{dust}})$ [M_{\odot}]	T_{dust} [K]	ν
1	$0.86^{+0.74}_{-0.21}$	$-8.96^{+0.21}_{-0.21}$	$7.37^{+8.07}_{-4.64}$	$-0.68^{+0.27}_{-0.27}$	$7.40^{+0.58}_{-0.66}$	$25.11^{+3.29}_{-3.83}$	1
2	$0.83^{+0.64}_{-0.32}$	$-9.54^{+0.13}_{-0.28}$	$8.45^{+6.89}_{-3.49}$	$-2.28^{+0.38}_{-0.80}$	$6.86^{+0.29}_{-0.56}$	$25.69^{+2.68}_{-2.18}$	1
3	$1.21^{+0.90}_{-0.67}$	$-8.09^{+0.16}_{-0.44}$	$12.73^{+5.29}_{-2.97}$	$-0.80^{+0.19}_{-0.14}$	$8.01^{+0.26}_{-0.20}$	$29.15^{+1.64}_{-1.19}$	10
4	$1.17^{+0.56}_{-0.44}$	$-8.91^{+0.15}_{-0.16}$	$6.67^{+2.04}_{-1.83}$	$-0.87^{+0.19}_{-0.17}$	$7.13^{+0.51}_{-0.18}$	$24.70^{+1.12}_{-1.29}$	3
5	$1.71^{+0.86}_{-0.61}$	$-9.42^{+0.21}_{-0.18}$	$18.14^{+7.20}_{-8.93}$	$-1.11^{+0.35}_{-0.33}$	$6.01^{+0.93}_{-0.66}$	$29.18^{+1.67}_{-3.12}$	2
6	$3.27^{+1.46}_{-1.71}$	$-9.67^{+0.35}_{-0.80}$	$10.74^{+3.57}_{-4.95}$	$-1.91^{+1.11}_{-1.23}$	$5.73^{+0.61}_{-0.64}$	$26.74^{+1.31}_{-2.62}$	1
7	$1.23^{+1.11}_{-0.59}$	$-9.21^{+0.16}_{-0.15}$	$9.34^{+5.80}_{-5.04}$	$-0.84^{+0.17}_{-0.22}$	$7.20^{+0.50}_{-0.45}$	$26.12^{+2.19}_{-3.17}$	1
8	$1.64^{+0.91}_{-1.08}$	$-7.93^{+0.18}_{-0.14}$	$9.09^{+3.77}_{-3.13}$	$-1.34^{+0.16}_{-0.11}$	$8.14^{+0.41}_{-0.17}$	$24.24^{+1.55}_{-1.77}$	7
9	$1.78^{+0.61}_{-0.67}$	$-8.54^{+0.10}_{-0.08}$	$6.58^{+2.49}_{-2.76}$	$-1.07^{+0.22}_{-0.16}$	$7.95^{+0.56}_{-0.18}$	$24.64^{+1.35}_{-2.13}$	5
10	$1.36^{+0.64}_{-0.38}$	$-8.99^{+0.09}_{-0.10}$	$7.15^{+6.36}_{-4.25}$	$-2.35^{+0.50}_{-0.81}$	$7.63^{+0.38}_{-0.28}$	$24.98^{+2.80}_{-3.49}$	1
11	$4.38^{+0.81}_{-1.66}$	$-8.48^{+0.09}_{-0.10}$	$7.30^{+6.81}_{-5.00}$	$-1.43^{+0.29}_{-0.29}$	$8.25^{+0.96}_{-0.33}$	$25.07^{+2.91}_{-4.39}$	3
12	$2.70^{+1.45}_{-1.44}$	$-10.20^{+0.64}_{-1.01}$	$17.70^{+6.48}_{-5.77}$	$-0.94^{+0.30}_{-0.24}$	$7.08^{+0.17}_{-0.12}$	$29.06^{+1.55}_{-1.85}$	2
13	$3.47^{+1.00}_{-0.92}$	$-9.43^{+0.23}_{-0.32}$	$19.22^{+7.02}_{-4.97}$	$-1.11^{+0.11}_{-0.24}$	$8.11^{+0.15}_{-0.15}$	$29.46^{+1.57}_{-1.43}$	3
14	$2.81^{+1.50}_{-1.47}$	$-10.41^{+0.52}_{-0.97}$	$11.34^{+8.58}_{-7.25}$	$-0.68^{+0.64}_{-0.75}$	$6.90^{+0.64}_{-0.28}$	$26.98^{+2.66}_{-4.22}$	1

metallicity-dependent GDR as defined in Rémy-Ruyer et al. (2014), which is a broken power-law, i.e. a linear scaling down to a metallicity of $12+\log(\text{O}/\text{H})=8.1$, and a power law with an index of 3.1 at even lower Z : For $Z=12+\log(\text{O}/\text{H})>8.10$:

$$\log(\text{GDR}) = 2.21 + 1.0 \times (8.69 - Z), \quad (1)$$

and for $Z=12+\log(\text{O}/\text{H})\leq 8.10$:

$$\log(\text{GDR}) = 0.96 + 3.1 \times (8.69 - Z). \quad (2)$$

Note that several other prescriptions for GDR calculations have been published to date. We discuss the reasoning of our choice in Appendix E.

3.1.2 Far-infrared SEDs of LARS Galaxies

SEDs fits for all LARS galaxies are shown in Appendix B. The agreement between the models and the data is generally very good, in particular below $\sim 100\mu\text{m}$. However, due to the lack of observations at wavelengths longer than $160\mu\text{m}$, the uncertainty largely increases to this end. The fit for LARS 6 is somewhat unreliable, owed to the fact that it is the faintest galaxy in the PACS bands of the whole sample. An examination of the shape of the SEDs shows that while most galaxies have a rather flat distribution in the range between $50\text{--}100\mu\text{m}$, LARS 2 and 10 show significant steepening within that range. This is a result of the lack of hot dust directly associated to star formation that would show up as excess in the mid-infrared. Consequently, they have lower γ values, i.e. the fraction of dust mass linked to PDR regions.

We further caution that our flux measurements were obtained using varying aperture sizes, reflecting the capabilities of the different instruments at varying wavelengths. In particular, a single source in IRAS or AKARI may show up as several sources in the blue WISE bands. In most cases the latter are likely of stellar origin and thus do not impact measurements in the far infrared. However, some might still be of extragalactic origin, contaminating our measurements and SED fits.

3.2 CO (1–0) Based Molecular Masses

3.2.1 CO (1–0) Luminosity

We convert our measured CO (1-0) velocity-integrated main beam brightness temperatures I_{CO} (given in units of K km/s) to CO luminosities using the definition of L'_{CO} by Solomon and Vanden Bout (2005), with an aperture correction factor added:

$$L'_{\text{CO}} = C_{\text{AP}} * 23.5 \Omega I_{\text{CO}} (1+z)^{-3} D_{\text{L}}^2 \quad (3)$$

L'_{CO} is then given in $\text{K km s}^{-1} \text{pc}^2$, Ω is the solid angle of the Gaussian beam in arcsec^2 , z the redshift and D_{L} the luminosity distance in Mpc. Note that in the original formula found in Solomon and Vanden Bout (2005) (equation 2 therein), Ω is the solid angle of the source convolved with the beam. In our case, however, we perform this convolution within the calculation of the aperture correction factor and thus must use the solid angle of the Gaussian beam instead.

3.2.2 Aperture Correction for the CO (1–0) Data

Although the majority of the galaxies in our sample is smaller than the beam size θ of the IRAM 30m telescope, some galaxies have blue diameters, D_{25} , much larger than θ (compare Tables 1, 2 and Figures 1, 3). In order to estimate the *total* molecular masses of those, an aperture correction is needed. We employ a similar method as described in Lisenfeld et al. (2011) and Stark et al. (2013), which we briefly outline here. Assuming an exponential CO source brightness distribution, the total CO flux of a circular ($\theta = 0..2\pi$) galaxy can be written in polar coordinates as:

$$I_{\text{CO,extra}} = \int_0^{2\pi} \int_0^\infty I(r) 2\pi r dr d\theta \quad (4)$$

Assuming $I_{\text{CO}}(r)$ exponentially distributed with a central peak I_0 and a scale length of $r_{\text{e,CO}}$, the above equation can be re-written:

$$I_{\text{CO,extra}} = I_0 \int_0^{2\pi} \int_0^\infty \exp\left[-\left(\frac{r}{r_{\text{e,CO}}}\right)\right] 2\pi r dr d\theta \quad (5)$$

This integral can be solved by partial integration and $I_{\text{CO,extra}}$ is found to be:

$$I_{\text{CO,extra}} = I_0 2\pi r_{e,\text{CO}}^2 \quad (6)$$

The shape of the main beam can be typically estimated as a Gaussian. In fact, it represents a weighting function, which attenuates the source flux. Its 2D Cartesian formula for a unity peak height is:

$$G(x, y) = \exp\left[-\left(\frac{x^2}{\sigma_x^2} + \frac{y^2}{\sigma_y^2}\right)\right] \quad (7)$$

The standard deviation σ is related to the full width at half maximum or rather the half power beam width (θ) by:

$$\theta = 2\sqrt{2\ln(2)} \sigma \quad (8)$$

Since the measured flux is the result of a convolution of the source brightness distribution with a Gaussian, the observed flux within the beam can be expressed as:

$$\begin{aligned} I_{\text{CO,obs}} &= I_{\text{CO,extra}} * G(x, y) \\ &= 4I_0 \int_0^\infty \int_0^\infty \exp\left[-\frac{\sqrt{x^2 + y^2}}{r_{e,\text{CO}}}\right] \\ &\times \exp\left[-4\ln(2)\left(\frac{x^2}{\theta^2} + \frac{(y \cos(i))^2}{\theta^2}\right)\right] dx dy \end{aligned} \quad (9)$$

The inclination i of the galaxy is also accounted for in equation (9). It may be not clear at first sight that the effect of i can be written within the Gaussian term, because in principle it should be taken into account in the source and not in the beam. This can be understood, when bringing to mind that the integration interval dy on the sky corresponds to a larger space interval on the source. This means that in the case of accounting for inclination in the source term, also the integration interval had to be changed to $dy' = dy/\cos(i)$, where dy' is the interval on the source. If one takes into account this effect, the result is the same as in the given formula, i.e. equation (9) can be derived via variable substitution from y to $y' = y \cos(i)$. Since this cannot be solved analytically, we carry out a numerical integration to find the aperture correction factor C_{AP} :

$$C_{\text{AP}} = \frac{I_{\text{CO,extra}}}{I_{\text{CO,obs}}} \quad (10)$$

For LARS galaxies with CO (1-0) detections C_{AP} ranges from 1.01–1.94, with an average correction of 30%. When calculating C_{AP} , the peak brightness temperature I_0 , cancels out, but the scale length of the CO distribution, $r_{e,\text{CO}}$, is needed as input. Previous studies showed that $r_{e,\text{CO}}$ can be estimated from the optical, blue D_{25} diameter (Young et al., 1995; Leroy et al., 2008; Lisenfeld et al., 2011; Davis et al., 2013), roughly independent of the Hubble type:

$$r_{e,\text{CO}} = a \times 1/2 D_{25}, \quad (11)$$

with a typically ranging from 0.2 to 0.25. For our work, we choose a value in-between, $a = 0.23$. The inclination of the galaxy is calculated using the relation of Hubble (1926):

$$\cos^2(i) = \frac{\left(\frac{b}{a}\right)^2 - q^2}{1 - q^2} \quad (12)$$

We adopt $q=0.2$, and minor-to-major axis ratios, b/a_{M18} , previously derived by Micheva et al. (2018), see Table 1.

3.2.3 Metallicity Dependent CO-to-H₂ Conversion

The CO-to-H₂ conversion factor, α_{CO} is a (virialized) mass-to-light ratio in units of $(\text{K km s}^{-1} \text{ pc}^2)^{-1}$ that is used to translate L'_{CO} into the molecular mass (including Helium). Given the extreme conditions in the ISM of (some) LARS

galaxies, will potentially cause large uncertainties in α_{CO} , e.g. due to cloud-cloud collisions. See Bolatto et al. (2013) for a review on the topic.

However, the strongest effect on α_{CO} variations may emerge due to low metallicity, because at some (low Z) point CO is not able to shield itself from the ambient radiation field, and is photo-dissociated, while H_2 survives at much larger column densities. Thus, the fraction of so called CO-dark molecular gas increases, an effect that needs to be accounted for by α_{CO} .

A variety of prescriptions for the metallicity-dependence of α_{CO} exist in the literature (Magdis et al., 2011; Genzel et al., 2012; Narayanan et al., 2012; Schrubba et al., 2012; Hunt et al., 2015; Amorín et al., 2016; Accurso et al., 2017). We decided to make use of a semi-analytic relation between the metallicity Z' , the O/H abundance in proportion to the solar abundance, and the conversion factor α_{CO} , published by Narayanan et al. (2012). We discuss the reasoning of our choice in Appendix E.

$$\alpha_{\text{CO}} = \frac{\min[6.3, 10.7 \times I_{\text{CO}}^{-0.32}]}{Z'^{0.65}} \quad (13)$$

Note that for the abundances of LARS galaxies given in Table 1, a solar reference value of $[12 + \log(\text{O}/\text{H}) = 8.7]$ was chosen.

3.2.4 Upper Limit Molecular Masses from CO (1–0)

For the six LARS galaxies that remained undetected in CO (1–0), we calculate upper limit CO luminosities from the 2-sigma baseline r.m.s. (measured outside the line window) multiplied by the square-root of number of channels found within a (typical) 200km/s wide line window. The derived CO upper limit luminosity is then further multiplied by the aperture correction factor and metallicity-dependent conversion factor α_{CO} exactly as described above. However, we caution that the aperture correction is strictly only valid for peaked CO distributions with an exponential radial decline. For sources with more complex morphologies – and this is the case for few of our galaxies – beam dilution might lower the perceived signal in an unforeseeable way. Moreover, the relatively low metallicity of the galaxies, leads to hardly predictable beam filling factors, due to large fractions of CO-dark gas (Schruba et al., 2017), which further reduces the ability to accurately derive limits. The reported upper limits have thus to be taken with caution.

3.3 Star Formation Rates from SED Models, $22\mu\text{m}$, [C II]158 μm and [O I]63 μm

Star formation rates can be derived through many different methods and tracers (see Kennicutt and Evans, 2012, for a review on the topic). In what follows, unless otherwise noted, we calculate SFRs from the total infrared luminosity L_{TIR} that we find from integration of our best-fit dust model SEDs over a range of 3–1100 μm . Using the prescription in (Kennicutt and Evans, 2012, Table 1 therein), which is based on work by Hao et al. (2011) and Murphy et al. (2011), we translate L_{TIR} into SFR, assuming a Kroupa and Weidner (2003) IMF. Consequently, whenever comparing any of our results to values in the literature, we pay attention to the underlying IMF and make adoptions, if needed. Thus, we convert from a Salpeter (1955) to a Kroupa IMF using a constant factor of 0.66. Given the similarity between Kroupa and Chabrier (2003) IMFs, no changes are made in that case.

Next, we briefly compare and discuss few other prescriptions to estimate star formation rates: an extrapolation from $22\mu\text{m}$ single-band observations (Rieke et al., 2009), estimates from extinction corrected $\text{H}\alpha$ and SFRs from [C II]158 μm and [O I]63 μm emission lines (using prescriptions of De Looze et al. (2014)). Taking the far-infrared SED-based SFRs as a reference, we find that both, the $22\mu\text{m}$ photometry and the [O I]63 μm line, agree very well, with only $\sim 10\%$ differences on average (see Table 9).

The situation is worse for (extinction corrected) $\text{H}\alpha$ and [C II] that lead to SFRs that are (on average) higher by factors of ~ 3 and ~ 5 compared to the infrared based estimates. However, for the case of [C II], the discrepancy is mainly driven by LARS 5, a galaxy that is known to have a large scale outflow (Duval et al., 2016). Our finding is thus in agreement with other studies (Appleton et al., 2013, 2018; Smirnova-Pinchukova et al., 2019) that reported on excess [C II]158 μm emission due to shocks connected to outflowing gas. Excluding LARS 5, the [C II] prescription of De Looze et al. (2014) leads to SFRs that are only $\sim 80\%$ higher. It is further recognized that SFRs from (extinction corrected) $\text{H}\alpha$ are comparable to those from [C II], at least once LARS 5 is excluded. In that case the ratio between SFRs from [C II] and $\text{H}\alpha$ is 1.7 only.

Table 9. Comparison of SFR estimates for LARS galaxies

ID	SFR _{Hα}	SFR _{22μm}}	SFR _[C II]	SFR _[O I]	SFR _{TIR}
(1)	(2)	(3)	(4)	(5)	(6)
1	6.5	4.6 \pm 0.12	–	–	2.13 ^{+1.66} _{-0.56}
2	1.4	0.2 \pm 0.06	0.4 \pm 0.2	<2.3	0.28 ^{+0.23} _{-0.11}
3	26.3	105.7 \pm 0.3	35.5 \pm 0.8	73 \pm 3	65.76 ^{+17.48} _{-2.41}
4	6.1	5.2 \pm 0.15	–	–	4.00 ^{+0.47} _{-0.18}
5	5.8	2.0 \pm 0.1	29 \pm 5	–	0.81 ^{+0.41} _{-0.17}
6	0.6	–	–	–	0.27 ^{+0.18} _{-0.06}
7	9.3	4.6 \pm 0.2	–	–	2.99 ^{+0.74} _{-0.15}
8	36.8	31.0 \pm 0.32	81 \pm 13	–	29.02 ^{+9.25} _{-6.38}
9	40.7	24.7 \pm 0.44	33.4 \pm 0.6	34 \pm 3	25.31 ^{+0.40} _{-3.56}
10	5.6	1.9 \pm 0.3	–	–	6.69 ^{+0.93} _{-2.22}
11	30.5	28.4 \pm 1.01	203 \pm 12	–	38.78 ^{+14.54} _{-5.96}
12	97.0	12.7 \pm 0.72	8.7 \pm 1.2	16 \pm 4	9.99 ^{+0.88} _{-0.12}
13	64.8	66.5 \pm 3.02	40.5 \pm 4.1	54 \pm 10	106.71 ^{+6.35} _{-10.07}
14	24.8	7.0 \pm 2.13	–	–	5.79 ^{+0.98} _{-0.14}

The SFRs are given in units of $M_{\odot} \text{ yr}^{-1}$. The LARS ID is shown in *column 1*. Previously published SFRs from extinction corrected H α (Hayes et al., 2014) are found in *column 2*. New SFR estimates from WISE 22 μ m, [C II]158 μ m, [O I]63 μ m and total infrared luminosities are given in *columns 3-6*. The latter one is used for all analysis (KS plots etc.) in this paper.

The reason for the elevated SFRs from H α and [C II] compared to the IR based results, is likely due to the sensitivity to different timescales of the tracers. Both, H α and [C II]158 μ m are sensitive to the currently ongoing star formation on timescales of \sim 10Myr, because they are directly linked to the recombination within H II regions, driven by young, massive stars. On the other side, for the continuum at infrared wavelengths and the TIR emission, a significant fraction of the heating is attributed to more evolved stars. Hence, the timescale probed by TIR is longer (\sim 100Myr). The aforementioned discrepancy between the SFRs might thus be caused by varying star formation histories (Melinder et al. in prep.), given the relatively young age of LARS galaxies, due to their selection with H α equivalent widths of more than 100Å (Östlin et al., 2014).

3.4 SFR and Gas Surface Densities

For calculations of star formation rate surface densities, Σ_{SFR} , and gas surface densities, Σ_{gas} , we normalize the measured integrated values to the area enclosed by the 25 mag arcsec⁻² isophote in the optical B-band, i.e. $D_{25\text{SDSS}} = \pi \times a/2 \times b/2$. $D_{25\text{SDSS}}$ was calculated from the SDSS g-band, which typically gives sizes that are \sim 1.3 times larger than those measured in the Johnson B band (Hakobyan et al., 2012). Thus, we divided the g-band diameters by that factor first.

Table 10. Derived properties for LARS galaxies

ID	\log_{10} Σ_{SFR}	\log_{10} $\Sigma_{\text{SFR}}^{\text{rcut}}$	GDR	α_{CO}	C_{AP}	\log_{10} L'_{CO}	\log_{10} $M_{\text{H}_2_{\text{obs}}}$	\log_{10} $M_{\text{H}_2_{\text{est}}}$	\log_{10} $M_{\text{gas}_{\text{obs}}}$	\log_{10} $M_{\text{gas}_{\text{est}}}$	\log_{10} Σ_{gas}	τ_{gas} $\times 10^8$	f_{gas}	f_{HI}	f_{mol}	f_{PDR}
(1)	(2)	(3)	(4)	(5)	(6)	(7)	(8)	(9)	(10)	(11)	(12)	(13)	(14)	(15)	(16)	(17)
1	-1.862	-0.277	455.0	11.40	1.07	<8.443	<9.438	9.816	<9.719	10.058	1.868	53.70	0.65	0.22	0.57	0.21
2	-2.901	-0.641	472.1	10.60	1.15	<8.666	<9.629	8.779	<9.849	9.534	1.185	122.10	0.59	0.82	0.18	0.01
3	-1.444	1.722	306.2	5.10	1.94	9.549	10.198	10.289	10.356	10.496	1.234	4.80	0.61	0.22	0.62	0.16
4	-1.866	-0.348	511.7	–	–	–	–	9.054	–	10.009	1.541	25.50	0.44	0.75	0.11	0.13
5	-2.339	-0.523	597.0	14.80	1.06	<8.482	<9.596	–	<9.835	8.786	0.539	7.50	0.13	4.75	–	0.08
6	-3.053	-0.828	699.5	–	–	–	–	–	–	8.575	0.090	13.90	0.15	–	–	0.01
7	-2.029	0.106	353.2	11.00	1.10	<8.539	<9.526	9.227	<9.810	9.748	1.244	18.70	0.54	0.55	0.30	0.14
8	-1.846	0.152	248.3	4.50	1.36	9.546	10.145	10.030	10.556	10.535	1.226	11.80	0.27	0.64	0.31	0.05
9	-0.425	0.157	342.0	11.70	1.01	8.573	9.595	10.173	10.229	10.484	2.656	12.00	0.37	0.43	0.49	0.09
10	-2.250	0.164	248.3	6.30	1.13	<9.353	<10.114	9.781	<10.243	10.025	0.950	15.80	0.33	0.42	0.57	0.00
11	-1.638	0.465	291.1	8.00	1.19	9.498	10.388	10.377	10.703	10.714	1.487	13.30	0.30	0.50	0.46	0.04
12	-2.021	-0.135	361.4	10.20	1.03	<9.457	<10.465	–	–	9.638	0.617	4.30	0.37	–	–	0.11
13	-1.333	0.543	249.5	11.30	1.03	9.273	10.364	–	–	10.507	1.146	3.00	0.35	–	–	0.08
14	-2.474	-0.536	848.2	–	–	–	–	–	–	9.829	0.592	11.60	0.79	–	–	0.21

Surface densities in columns (2) and (10) are normalized to the B-band 25 mag arcsec⁻² area, while the SFR surface density in column (3) is normalized to the star forming area only. The CO luminosity in column (7) was derived from the CO velocity-integrated main beam brightness temperature and subsequent multiplication with the aperture correction factor in column (6). For galaxies with CO detection, $M_{\text{H}_2_{\text{obs}}}$ in column (8) was calculated from the CO luminosity in column (7) via application of the conversion factor in column (5). For galaxies with positive CO and H I detections, $M_{\text{gas}_{\text{obs}}}$ is the sum of the atomic mass from Paridy et al. (2014) and the molecular mass in column (8). Total gas masses $M_{\text{gas}_{\text{est}}}$ in column (11) were derived from the dust masses using a metallicity-dependent gas-to-dust ratio shown in column (4). The estimated molecular mass $M_{\text{H}_2_{\text{est}}}$ is the result of the dust based total mass $M_{\text{gas}_{\text{est}}}$ minus the observed atomic gas mass. The total gas surface density in column (12), the total gas depletion time τ_{gas} in column (13) as well as the total gas fraction $f_{\text{gas}} = M_{\text{gas}_{\text{est}}}/(M_* + M_{\text{gas}_{\text{est}}})$ in column (14) are using the dust-based total gas mass estimate. The atomic gas fraction f_{HI} is the ratio between the observed H I gas mass and the total dust-based gas mass. The molecular gas fraction f_{mol} is the ratio between the estimated molecular gas mass and the total dust-based gas mass. The PDR gas mass fractions in columns (17) are the γ values from Table 8 on a linear scale. Note that the large discrepancies between the reported upper limits in columns (8) and (10) and the dust-based estimated quantities are likely the result of beam dilution, i.e. the upper limits are likely misleading.

The units of the derived quantities are:

(2), (3): $M_{\odot} \text{ yr}^{-1} \text{ kpc}^{-2}$

(5): $(\text{K km s}^{-1} \text{ pc}^2)^{-1}$

(7): $\text{K km s}^{-1} \text{ pc}^2$

(8)-(11): M_{\odot}

(12): $M_{\odot} \text{ pc}^{-2}$

(13): yr

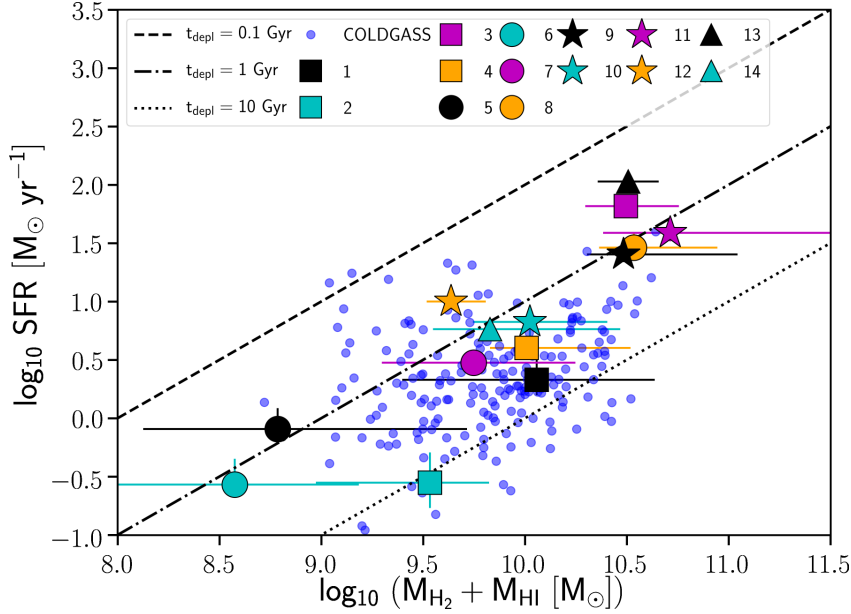


Figure 8. Gas mass and SFR (from total integrated infrared luminosity) scaling for LARS galaxies and COLDGASS, a $z \sim 0$ representative sample of galaxies.

4 Results

4.1 Scaling of Gas Mass and SFR

The scaling relation between dust-traced total gas mass and star formation rate in Figure 8 shows that LARS galaxies span a more than two orders of magnitude wide range in both quantities. LARS comprises the whole parameter space of the COLDGASS survey (Saintonge et al., 2011a,b, 2012; Catinella et al., 2012), a representative sample of $z \sim 0$ galaxies with masses above $10^{10} M_{\odot}$. A comparison between the two applied methods to calculate gas masses (dust-based vs. CO+HI based) is shown in Figure 9. For those galaxies (LARS 3, 8, 9, 11) with combined measurements of CO+HI available (LARS 13 was not detected in H I previously), we find an excellent match between the two methods, i.e. on average they agree on a level better than ~ 0.2 dex. Note that the upper limit molecular masses from our CO (1-0) observations are most likely affected by beam dilution, leading to an increase of the limits towards higher masses. We only use dust-based gas mass estimates for the following analysis.

4.2 KS Relation, Gas Fractions and Depletion Times

The global molecular Kennicutt-Schmidt relation for LARS is shown in the top panel of Figure 10. We compare our sample to the COLDGASS population as well as to $z \sim 1-3$ massive star forming main sequence galaxies of Genzel et al. (2010).

Compared to COLDGASS galaxies our sample is biased towards higher H_2 surface densities, with LARS 9 at the extreme end, where typically only high- z star-forming galaxies are located. At the lowest end, LARS 2 is found. The molecular gas depletion time, defined as the ratio between $\Sigma_{M_{H_2}}$ and Σ_{SFR} seems to be rather consistent for the whole sample, with a scatter of only ± 1 Gyr around the median value of 0.7 Gyr. The classical KS relation in the bottom panel of Figure 10 is slightly different. The total gas depletion time, i.e. the ratio between $\Sigma_{M_{H_2} + M_{HI}}$ and Σ_{SFR} , has a 3 times larger scatter (± 3 Gyr) around the median of 1.3 Gyr for the whole sample.

The inverse of the gas depletion time is often denoted as the *star formation efficiency* (hereafter SFE), i.e. the star formation rate per unit gas mass. However, it is important to understand that the SFE as defined above is not necessarily an indication of a true efficiency or ability to form stars per unit gas mass, because not all the observed gas is readily available to fuel the current star formation. The efficiency is thus degenerate with the gas fraction. For that reason, Krumholz et al. (2012) suggest to normalize the SFE by the cloud-scale gravitational free-fall time τ_{ff} . That way, the scatter in the classical KS law decreases. Unfortunately, τ_{ff} cannot be assessed from our observations, because the determination of τ_{ff} involves knowledge of the volume density of the gas, a quantity that cannot be performed based on our observations. For that reason we will mainly make use of the inverse of the SFE as defined above, which is the gas

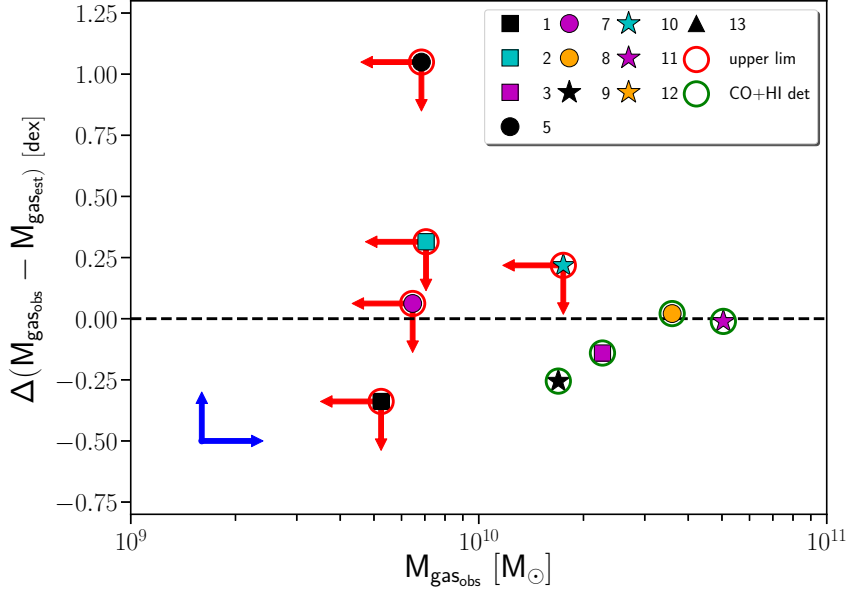


Figure 9. Total gas masses from combined CO (1-0) and H I observations vs. the difference between observed total gas mass (CO+HI) and the dust-based total gas mass. Galaxies with detections in CO+HI are encircled in *green*, while measurements with CO and/or H I upper limits are shown in *red*. Note that the CO upper limits are most likely unreliable due to beam dilution that works in the direction of the *blue arrows*.

depletion time (τ_{gas}), i.e. the timespan star formation may be maintained at the current level given the amount of gas available.

With previously published stellar masses (Hayes et al., 2014) that are given in column 3 of Table 1, the total gas fraction can be defined: $f_{\text{gas}} = M_{\text{gas,est}} / (M_* + M_{\text{gas,est}})$. For LARS the total gas fractions vary from $\sim 15\text{--}80\%$. All derived quantities discussed in this section are summarized in Table 10.

4.3 Compactness and Characteristic Size of Star Formation Activity

Figure 11 shows the star formation rate versus the surface density of star formation, $\Sigma_{\text{SFR}}^{\text{rcut}}$ – in this case the SFR is normalized to the area of star forming activity (derived by Micheva et al. (2018) from FUV imaging) rather than stellar content. It is striking that compared to the previous KS plots the scatter in the y direction is largely decreased, and also that compared to other galaxy samples, the size of the star forming activity in LARS galaxies is found to be roughly constant with a median diameter of $\sim 1\text{kpc}$, similar in size to circumnuclear star formation activity. However, a weak but tight trend is seen between $\Sigma_{\text{SFR}}^{\text{rcut}}$ and SFR, in a sense that galaxies with high star formation rates exhibit larger and more crowded areas of star formation. A possible explanation for the tighter spread seen in $\Sigma_{\text{SFR}}^{\text{rcut}}$ compared to Σ_{SFR} may be found in the star formation history, which varies from one LARS galaxy to another and has led to varying fractions and sizes of a (older) stellar populations, while the currently ongoing star formation density is similar.

4.4 Grouping LARS According to τ_{gas}

An examination of the gas depletion times and gas fractions (see Table 10) reveals that the heterogeneity of LARS galaxies that is seen in the KS law is related to $\text{Ly}\alpha$ escape. While, no trend is seen between total gas surface density and $\text{Ly}\alpha$ escape, we find a strong trend between the total gas depletion time and $\text{Ly}\alpha$ escape fraction (see Figure 12). This is also seen when grouping LARS galaxies into bins of increasing total gas depletion times (τ_{gas}):

- *Group 1* ($\tau_{\text{gas}} \lesssim 1\text{Gyr}$):
As seen in Figure 10, the galaxies with the shortest gas depletion times are LARS 3, 5, 12 and 13.
- *Group 2* ($1\text{Gyr} \lesssim \tau_{\text{gas}} \lesssim 2\text{Gyr}$):
In the group of intermediate gas depletion times – with values that are typically found in main sequence galaxies – we find LARS 6, 8, 9, 10, 11 and 14. This group is the largest of the three and the galaxies within are quite

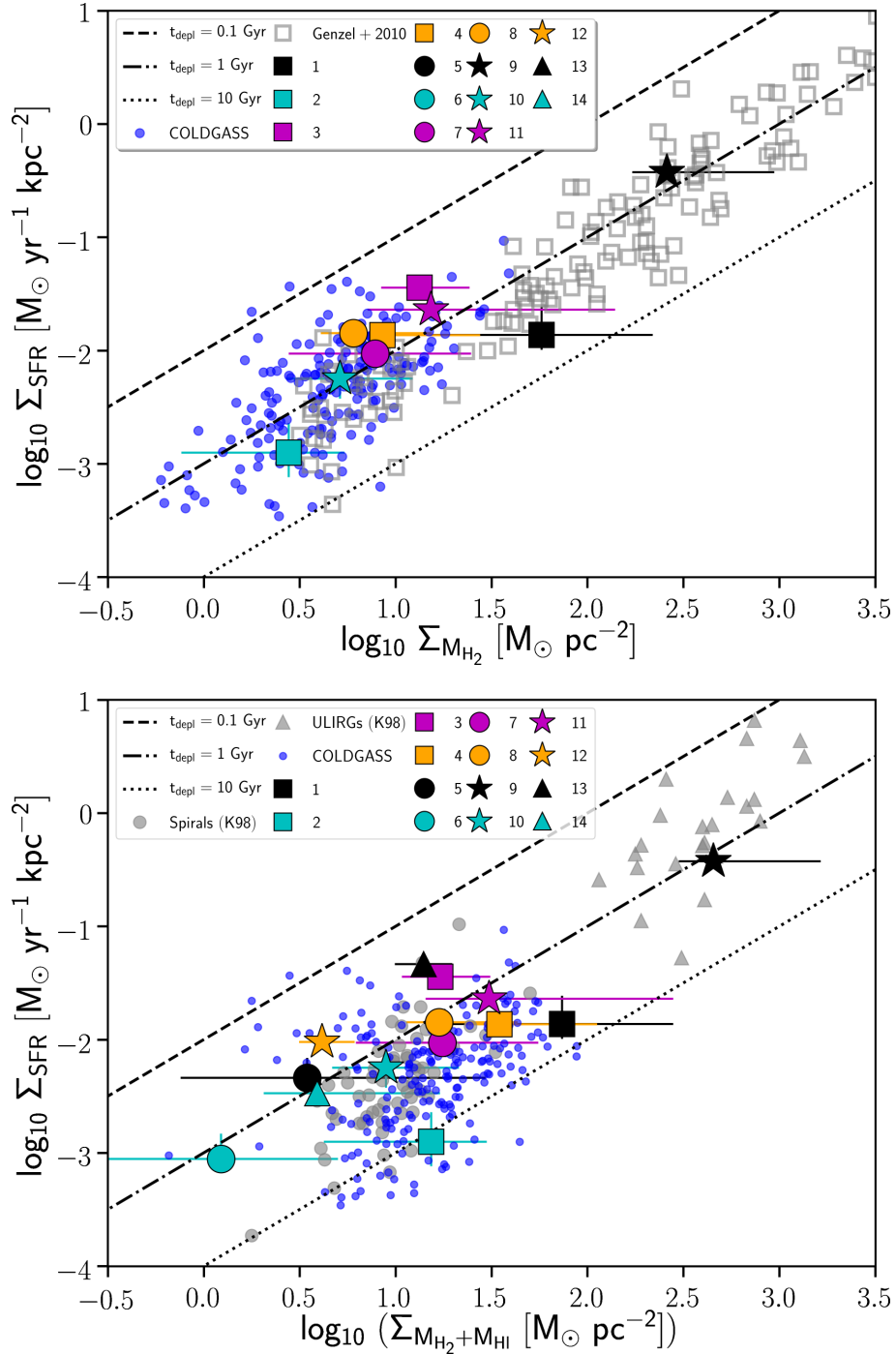


Figure 10. *Top panel:* Molecular KS relation: H_2 surface density (from dust-based gas mass minus atomic mass) versus star formation rate surface density (from total integrated L_{TIR}) for LARS compared to COLDGASS (blue) and a sample of $z \sim 1-3$ star forming galaxies from Genzel et al. (2010) (gray open squares). *Bottom panel:* KS relation: Total gas surface density (dust-based) vs. star formation rate surface density (from total integrated L_{TIR}). The COLDGASS galaxies (blue) and Kennicutt (1998) samples of local spirals (gray filled circles) and ULIRGs gray filled triangles are shown as reference. Black diagonal lines indicate (from top to bottom) constant gas depletion times of 0.1, 1 and 10 Gyr.

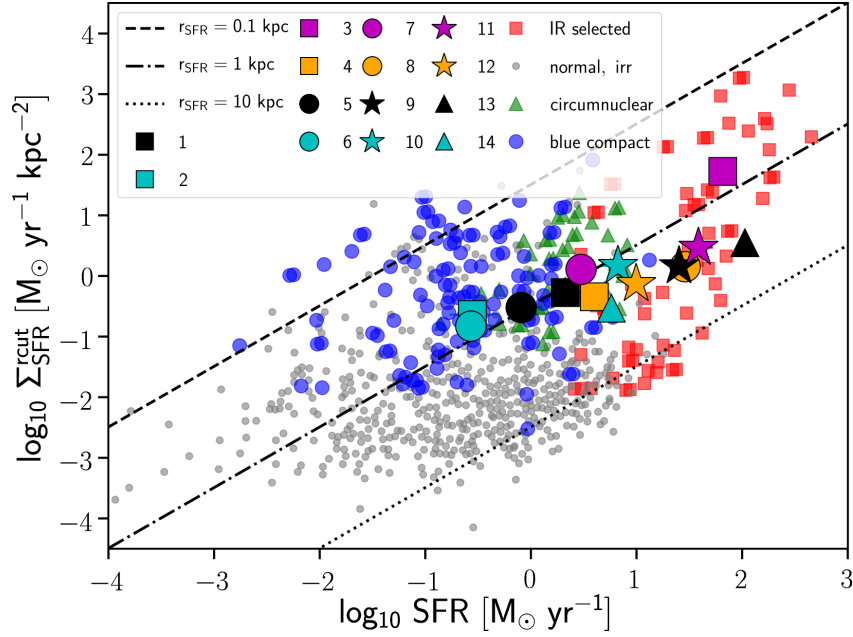


Figure 11. Total SFR versus the star formation rate density (both using SED integrated L_{TIR} as tracer) normalized by the area of activity (as seen in UV). Overplotted are comparison samples of Kennicutt and Evans (2012).

Table 11. Average and median properties of LARS galaxies grouped into bins of increasing gas depletion times. Median quantities are given in the brackets.

	τ_{gas} [10^8 yr]	$f_{\text{esc}}^{\text{Ly}\alpha}$ [%]	D_{scatt} [kpc]	f_{gas} [%]	f_{mol} [%]	U_{min}
Group 1 (3,5,12,13)	5 (5)	4.9 (1.0)	1.0 (0.7)	37 (36)	62 (62)	17.0 (17.9)
Group 2 (6,8,9,10,11,14)	13 (13)	5.1 (2.6)	0.9 (0.5)	37 (32)	46 (48)	8.7 (8.2)
Group 3 (1,2,4,7)	55 (40)	24.6 (11.9)	0.5 (0.5)	56 (57)	29 (24)	7.9 (7.9)
All LARS (incl. 6)	23 (13)	9.9 (3.1)	0.8 (0.5)	42 (37)	40 (46)	10.8 (9.2)

diverse. In fact we could break up the group into high- and low- stellar mass sub-samples. While the high-mass galaxies (LARS 8, 9, 10 and 11) might indeed be similar to $z \sim 1-2$ main sequence galaxies, a characterisation of the low-mass galaxies (6, 14) is difficult.

- *Group 3* ($\tau_{\text{gas}} \gtrsim 2\text{Gyr}$):
Those LARS galaxies that have relatively high gas surface densities and low SFR surface densities (1, 2, 4, 7) have much larger total gas fractions.

Next, we calculate for each τ_{gas} group the average and median physical quantities that we previously derived and relate those to the properties of $\text{Ly}\alpha$ escape. The result is shown in Table 11. Note that the results hold-up when the median is used instead of the average. It is eye-catching that LARS galaxies with the longest depletion times (Group 3) also exhibit the highest $\text{Ly}\alpha$ escape fractions (more than twice of the average in the sample), while they have the shortest $\text{Ly}\alpha$ scattering distances. Moreover their average environment and ISM conditions are significantly different from the other two groups, in a sense that their mean (FUV) energy density U_{min} is the lowest and their total gas fractions are highest (while having the lowest molecular gas fraction). We discuss this further in Sections 5.1 and 5.2.

4.5 Extreme [C II]158 μm Line Strength in LARS 5 and Basic PDR Analysis

In eight LARS galaxies, the [C II]158 μm line was successfully detected, either with Herschel/PACS or SOFIA/FIFI-LS. We first examine the relative strength of the [C II]158 μm line compared to the total far-infrared energy. As seen in Figure 13, LARS 5 is an extreme outlier in the plot. Neither LINER, Seyfert or QSOs from the SHINING survey (Herrera-Camus et al., 2018a,b; Zhao et al., 2016), nor any other non-AGN galaxy observed to date (see figure caption for details about the comparison samples), has a global [C II]158 μm to FIR ratio on the order of $\sim 14 \pm 3$ percent as seen

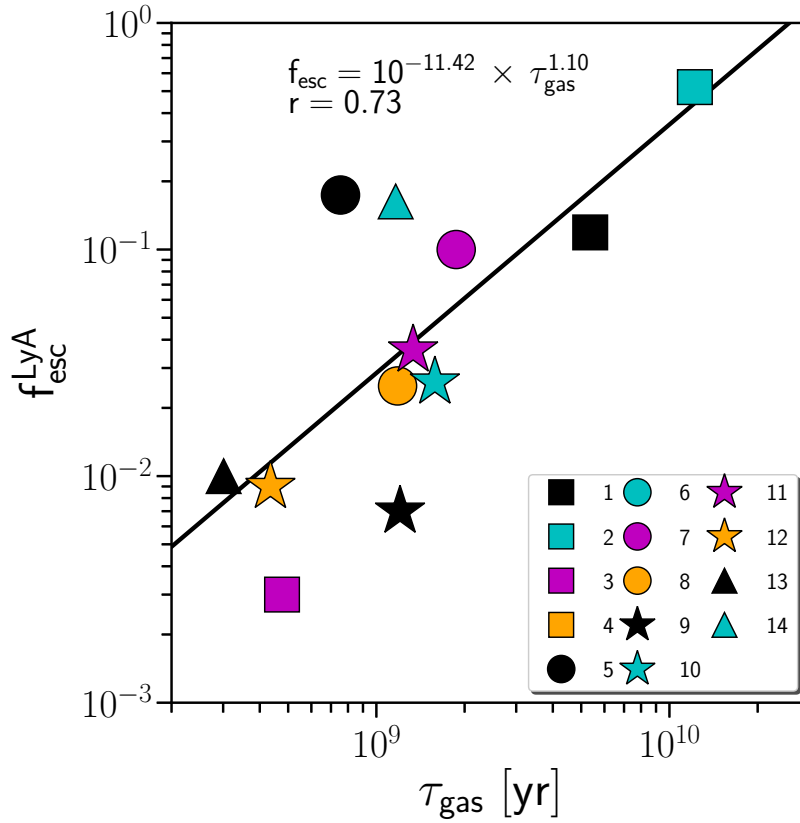


Figure 12. Relation between total gas depletion time and Ly α escape fraction. Note that LARS 4 and 6 have a *global* Ly α escape fraction of zero and are thus omitted in the fit.

in LARS 5 (see also Table 12). The mechanism that drives the extreme ratio is likely connected to the large scale galactic wind that was previously reported and studied by Duval et al. (2016). This is supported by the fact that both, the [C II]158 μ m and [O III]88 μ m emission lines are blueshifted from the systemic velocity, as seen in Figures 5 and 7. Note that shock-enhanced [C II]158 μ m excess was previously observed in other galaxies with outflows (Appleton et al., 2013, 2018; Smirnova-Pinchukova et al., 2019).

While LARS 5 is an extreme outlier, most of the other galaxies detected in [C II]158 μ m (3, 8, 9, 11, 12 and 13) also lie on the upper end of what is typically observed in local galaxies. On the other hand, LARS 2 has a much weaker relative [C II] line strength, which is interesting, considering the fact that LARS 2 is the only galaxy with a [C II] detection that is member of Group 3 (while LARS 7 despite having the longest integration time remained undetected).

We perform a very basic PDR analysis based on the models of Kaufman et al. (1999, 2006). Using the far infrared luminosity (L_{FIR_w}) and emission lines of [C II]158 μ m and [O I]63 μ m, we apply PDR Toolbox (Pound and Wolfire, 2008) to fit the observed line ratios against the model predictions. The results for the best-fit model are summarized in Table 13. The quality of the fits can be assessed from Figure 24, where the contours indicate 1, 2 and 3 σ significance regions that are confined by $\chi^2_{\alpha} = \chi^2_{\text{min}} + \delta(\nu, \alpha)$ (Wall, 1996), with the χ^2 -difference δ being a function of degrees of freedom ν (in our case $\nu=1$) and α the desired significance (in our case 0.68, 0.95 and 0.99). Note that for LARS 3 and 9, the models are not able to reproduce the observations, i.e. $\chi^2_{\text{min}} \gg 1$. This might be related to the fact that both are merging galaxies. However, for the remaining galaxies LARS 2, 12 and 13 we find model fits with uncertainties of ± 0.6 , ± 0.15 and ± 0.1 dex respectively. It may also be recognized in Figure 24 that the solution plane shows two valleys (bimodality), with density and radiation field strength being degenerate. However, solutions at lower gas densities and stronger radiation field strengths G_0 are more pronounced. For the second valley the solutions would lead to $G_0 < 3$, i.e. relatively low given the starburst nature of our galaxies. We caution that we apply models that are valid only for a particular regime (PDR) to unresolved observations that cover a multi-phase ISM. Thus, the power of such an analysis is limited. However, a comparison of the derived PDR gas volume densities between LARS 2 (which is member of Group 3) and LARS 12 and 13 (Group 1) shows that the density in LARS 2 is ~ 5 times (or 0.7 dex) higher than the average density of LARS 12 and 13. Assuming that the high PDR gas density holds for the whole Group 3, this might

Table 12. FIR Continuum and Line Luminosities

ID	L_{TIR} 3 – 1100 μm [10^{42} erg s $^{-1}$]	L_{FIR_w} 40 – 500 μm [10^{42} erg s $^{-1}$]	$L_{\text{FIR}_{n,\text{SED}}}$ 40 – 120 μm [10^{42} erg s $^{-1}$]	$L_{\text{FIR}_{n,\text{H88}}}$ 40 – 120 μm [10^{42} erg s $^{-1}$]	L_{CII} [10^{39} erg s $^{-1}$]	L_{OI63} [10^{39} erg s $^{-1}$]	L_{OIII88} [10^{39} erg s $^{-1}$]	L_{CO10} [10^{36} erg s $^{-1}$]
1	54.81 $^{42.48}_{-14.4}$	31.43 $^{28.54}_{-6.79}$	24.6 $^{16.81}_{-4.03}$	19.64 $^{14.89}_{-0.04}$	–	–	–	<48
2	7.27 $^{5.73}_{-2.66}$	6.14 $^{4.62}_{-2.2}$	3.86 $^{3.39}_{-1.41}$	7.08 $^{0.01}_{-3.09}$	17 \pm 8	62 \pm 43	–	<80
3	1690.33 $^{449.23}_{-61.83}$	950.04 $^{135.73}_{-15.56}$	796.7 $^{147.86}_{-0.08}$	136.79 $^{287.82}_{-102.34}$	1564 \pm 36	2994 \pm 145	1918 \pm 124	619 \pm 31
4	102.71 $^{12.08}_{-4.48}$	58.66 $^{6.25}_{-2.2}$	47.34 $^{3.49}_{-3.84}$	27.22 $^{21.18}_{-0.22}$	–	–	–	–
5	20.88 $^{10.39}_{-4.32}$	12.35 $^{3.28}_{-1.01}$	10.44 $^{2.75}_{-0.69}$	9.15 $^{7.07}_{-0.01}$	1260 \pm 223	–	671 \pm 114	<53
6	6.91 $^{4.64}_{-1.67}$	4.85 $^{1.65}_{-0.44}$	3.65 $^{1.17}_{-0.12}$	5.15 $^{4.06}_{-0.02}$	–	–	–	–
7	76.85 $^{19.1}_{-3.93}$	43.81 $^{12.16}_{-3.55}$	34.61 $^{7.06}_{-4.94}$	20.62 $^{15.66}_{-0.04}$	–	–	–	<62
8	745.8 $^{238}_{-164.1}$	502.59 $^{171.45}_{-81.5}$	369.91 $^{145.05}_{-64.07}$	645.18 $^{0.5}_{-2.25}$	3580 \pm 549	–	–	629 \pm 14
9	650.46 $^{10.24}_{-91.46}$	362.57 $^{19.57}_{-25.97}$	291.66 $^{3.35}_{-38.07}$	178.83 $^{0.55}_{-0.58}$	1471 \pm 29	1284 \pm 119	–	69 \pm 7
10	171.95 $^{23.8}_{-57.06}$	139.8 $^{16.97}_{-47.5}$	100.63 $^{24.54}_{-54.53}$	83.99 $^{0.01}_{-0.14}$	–	–	–	<434
11	996.71 $^{373.73}_{-153.26}$	579.55 $^{247.91}_{-73.8}$	428.6 $^{195.41}_{-21.22}$	603.07 $^{1.56}_{-0.06}$	8930 \pm 542	–	–	671 \pm 43
12	256.77 $^{22.65}_{-3.14}$	127.87 $^{20.97}_{-5.96}$	106.62 $^{20.6}_{-6.55}$	29.93 $^{60.7}_{-21.21}$	383 \pm 55	532 \pm 158	–	<653
13	2742.85 $^{163.12}_{-258.7}$	1424.78 $^{39.71}_{-55.27}$	1225.98 $^{8.15}_{-72.1}$	208.94 $^{146.47}_{-1.05}$	1785 \pm 182	2124 \pm 446	–	502 \pm 45
14	148.8 $^{25.16}_{-3.65}$	59.7 $^{21.27}_{-7.83}$	51.61 $^{10.75}_{-1.9}$	99.89 $^{76.77}_{-0.03}$	–	–	–	–

For continuum (TIR and FIR) luminosities we integrate for each galaxy the best-fit Draine et al. (2007) SED model, using a variety of ranges along the wavelength axis. For TIR, we use 3–1100 μm , as defined in Kennicutt and Evans (2012). In order to compare our measurements to previous studies (as done in Figure 13), we further calculate several versions of the FIR luminosity: L_{FIR_w} , i.e. integrated over 40 – 500 μm and used on the x-axis of Figure 13 as well as $L_{\text{FIR}_{n,\text{H88}}}$, i.e. the FIR luminosity valid for the range of 40 – 120 μm , but estimated from single flux densities at 60 and 100 μm as defined by Helou et al. (1988). $L_{\text{FIR}_{n,\text{H88}}}$ is used for the [C II]-to-FIR ratio that is given on the y-axis in Figure 13. For comparison, we also provide $L_{\text{FIR}_{n,\text{SED}}}$, i.e. the SED-integrated luminosity along the same range of 40 – 120 μm . The line luminosities are derived via Gaussian fitting.

Table 13. PDR model results. The solution space (n, G_0, χ^2) is shown in Figure 24.

ID	χ^2	n [cm^{-3}]	G_0
2	0.05	5620	562
12	0.4	1780	562
13	0.1	562	1000

signalize that bulk of the star forming regions are still deeply embedded in their birth clouds that were not yet disrupted due to stellar feedback. We are thus likely witnessing early stages of star formation. This scenario is supported by low Σ_{SFR} , low U_{min} values and high total gas fractions found in Group 3.

Assuming that the high observed PDR gas volume density in LARS 2 is reflecting a high density of the cold, star-forming gas, the free-fall time in LARS 2 is ~ 3 times shorter, suggesting that the scatter in the KS law – once normalized to the free-fall time – could indeed be largely reduced, given that LARS 2 is the most extreme outlier in the relation.

We also put the LARS galaxies onto a widely used diagnostic diagram as shown in the right panel of Figure 13 and overplot lines of constant density together with knot points indicating the FUV field strength G_0 . The shown models were calculated for two metallicities, one with solar and the other one with one tenth solar abundances. We further consider only the case for $A_V=1$. Note that with this diagram we mainly want to showcase the general sensitivity of the diagnostic lines. While the [C II]158 μm to FIR ratio mainly defines the density, the CO (1–0) to FIR ratio is most sensitive to the radiation field.

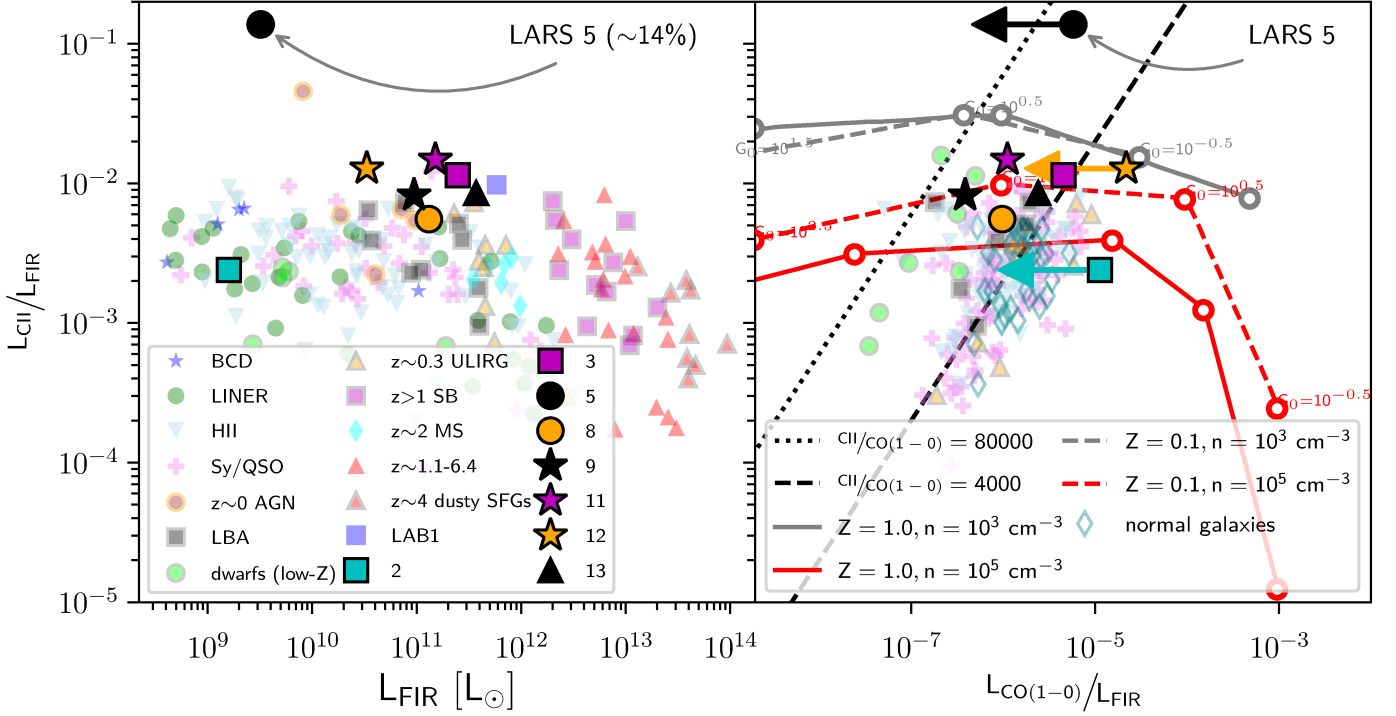


Figure 13. L_{CII} 158 μm line to $L_{\text{FIR},n,\text{H88}}$ ratio for LARS galaxies as a function of $L_{\text{FIR},w}$ (left panel) and as a function of $L_{\text{CO}10}$ line to $L_{\text{FIR},n,\text{H88}}$ ratio (right panel), together with reference data. For the left plot, we updated the compilation in (Graciá-Carpio et al., 2011, Fig. 1), and added samples of Lyman Break Analogs (LBA) from Contursi et al. (2017), local low-metallicity dwarfs from Cormier et al. (2014, 2015), $z \sim 0$ AGNs from the CARS survey (Smirnova-Pinchukova et al., 2019), $z \sim 0.3$ ULIRGs from Magdis et al. (2014), $z > 1$ starbursts (SB >1) taken from Carilli and Walter (2013), $z \sim 2$ main-sequence (MS) galaxies (Zanella et al., 2018), the Lyman Alpha Blob 1 (LAB1) at $z \sim 3.1$ from Umehata et al. (2017) and $z > 4$ dusty star-forming galaxies (Bothwell et al., 2017). The right hand plot is based on (Contursi et al., 2017, Fig. 9), which we updated by adding normal galaxies from De Breuck et al. (2011) (originally drawn from Stacey et al. (2010)), as well as local low-metallicity dwarfs from Cormier et al. (2010, 2014, 2015); Madden and Cormier (2018). Black dotted and dashed lines in the right panel indicate constant [C II]-to-CO(1-0) ratios of 80000 and 4000 respectively. Red and gray solid curves show PDR models of Kaufman et al. (1999) for densities of $n = 10^5$ and $n = 10^3 \text{ cm}^{-3}$ at solar metallicity ($Z=1.0$), while dashed curves indicate low metallicity ($Z=0.1$). For the low metallicity cases, the changing FUV radiation field along the curves is given in steps of 1dex in G_0 from right to left.

Table 14. Interpretation of the molecular line ratios using the Dense Gas Toolbox (Puschnig, 2020)

ID	$\langle n \rangle$ [cm ⁻³]	T [K]	Width [dex]	f _{dense} [%]	χ^2
3	~8000	30	0.6	36	1.5
8	~80	25	0.6	<1	5.1

Assuming a log-normal distribution of densities with a fixed width of 0.6 dex and a fixed temperature (using results from the dust models), we derive the mass-weighted mean density $\langle n \rangle$, as well as the corresponding dense gas fraction f_{dense}.

4.6 Dense Gas Fractions in LARS 3 and 8

For the two LARS galaxies with detections in HCN (1-0), we calculate the line ratios of HCN(1-0)/CO(1-0). Given the fact that the critical density of HCN (1-0) is almost 2 orders of magnitude higher than for CO (1-0), the ratio among these two lines is often used as a tracer of the *dense gas fraction* (Gao and Solomon, 2004c; Bigiel et al., 2016; Jiménez-Donaire et al., 2017). We find line ratios of 0.13 and 0.05 for LARS 3 and LARS 8 respectively. While the latter is similar to values found e.g. in M51 (Bigiel et al., 2016), the former ratio indicates an extremely high dense gas fraction that is on the upper limit of what is typically found in infrared-luminous star-forming galaxies (compare to e.g. Juneau et al., 2009, Figure 6). The high dense gas fraction in LARS 3 is likely the result of the ongoing merging process that triggers a nuclear starburst in the galaxy.

4.7 Derived Properties from Line Ratios of CO, HCN and HCO+

The IRAM 30m telescope is capable of using two heterodyne receivers at the same time. We made use of this feature and observed CO (1–0) and CO (2–1) simultaneously. However, given the different beamsizes and thus beam filling factors, in combination with the complex morphology of our galaxies, one must be cautious when interpreting line ratios between CO (2–1) and CO (1–0). On the other side, observations of the CO (3–2) line with APEX and CO (1–0) with IRAM, give similar beam widths. Hence, the ratio among these two lines may give insight into the average conditions of the molecular gas. As shown in Figure 2, we detected CO (3–2) in two of our galaxies. We find CO(3–2)/CO(1–0) line ratios of 0.5 and 1.0 (on the brightness temperature scale) for LARS 8 and 13 respectively. The former value indicates sub-thermal excitation, whereas the conditions in LARS 13 are more extreme and the line ratio suggests thermalized gas up to the CO J=3 level. This result is in agreement with our derivations of U_{min}, the average energy density, which was found to be extremely high for LARS 13 and moderate in LARS 8 (see Table 8).

4.7.1 Line Radiative Transfer Modeling for LARS 3 and 8

Given the variety of emission lines now available (i.e. CO (1–0), CO (2–1), HCN (1–0) and HCO+ (1–0)) for LARS 3 and 8, as well as CO (3–2) for the latter one, we are able to estimate the molecular gas density using novel line radiative transfer models, described in detail in a forthcoming paper by Puschnig et al. (in prep). Note that a first release of the Dense Gas Toolbox (Puschnig, 2020) is readily available, either as stand-alone web application⁷ or source code⁸. The radiative transfer models rely on RADEX (van der Tak et al., 2007), but extend the original code to take into account that molecular emission lines may emerge from a distribution of densities rather than from a single-zone (single-density) medium. This approach is more realistic, in particular for unresolved or low-resolution observations as in our case, and has strong impact on interpreting line ratios in terms of physical quantities, as shown by Leroy et al. (2017). We adopt a density distribution that is log-normal and derive the *mass-weighted* mean density of that underlying gas distribution. Making use of the previously derived dust properties, we assume fixed temperatures, i.e. 30 and 25 K for LARS 3 and 8 respectively. A summary of the line ratios used as input for the modeling is shown in Table 15. This approach further allows to derive the *dense gas fraction*, defined as the fraction of gas mass with densities higher than 10^{4.5} cm⁻³. The results for LARS 3 and 8 are summarized in Table 14, and the χ^2 solution planes are shown in Figure 25.

⁷<http://www.densegastoolbox.com>

⁸<https://doi.org/10.5281/zenodo.3686329>

5 Discussion

5.1 Turbulence Driven Lyman Alpha Escape

As shown in Table 11, those LARS galaxies with the longest gas depletion times (Group 3: LARS 1, 2, 4, 7) have (on average) largest total gas fractions (while having the lowest molecular gas fractions) and the lowest energy densities (U_{\min}), compared to the other two groups of LARS galaxies. These galaxies really stand out in that they have very high Ly α escape fractions, while their scattering distances, i.e. a measure of the path length a Ly α photon travels before it escapes, are short. The combined properties of being gas-rich and having short scattering distances, is evidence for a kinematic-driven escape in which Ly α photons are shifted out of resonance relatively close to their origin. Previous high-resolution HST imaging in the optical, H α and UV further reveal a sufficiently clumpy ISM (Messa et al., 2019) and disks without substantial bulge in those LARS galaxies. Moreover, Herenz et al. (2016) studied H α kinematics of LARS galaxies and revealed that the highest Ly α escape fractions are found in dispersion dominated systems. Hence, we are likely witnessing early stages of disk formation, similar to the theoretical predictions of Dekel et al. (2009) for high- z galaxies. In such a scenario, cold gas accretion primarily causes disk instabilities that lead to the formation of massive clumps due to shear (each containing a few percent of the disk mass). Encounters between the clumps in the disk further stir up velocity dispersion, which at the same time enables Ly α photons to escape. The timescale of this process, however, is similar to the timescale of turbulent dissipation, so that the dynamical friction between the massive clumps finally leads to loss of angular momentum and migration to the center where a bulge is formed. We thus conclude that this process significantly enhances Ly α escape on timescales of a few hundred Myr. Note that this scenario is also in agreement with simulations of molecular gas (at high redshift) by Kimm et al. (2019), who find that Ly α scatterings and escape are already significant on cloud-scales.

5.2 Stellar Feedback Driven Lyman Alpha Escape

Other LARS galaxies (Group 1: 3, 5, 12, 13) have much shorter gas depletion times. They will run out of fuel in less than ~ 1 Gyr. Also, their physical properties are distinct. They have the highest energy density (U_{\min}) and longest Ly α scattering distances. From HST imaging we also recognize that these galaxies show a rather compact and more centralized light distribution. This suggests that bulk of the gas and star formation is concentrated in a bulge-like structure, explaining higher average energy densities. This is also supported by our molecular line radiative transfer modeling of LARS 3 (member of Group 1), that indicate a very high *mean* molecular gas density of $\sim 10^4$ cm $^{-3}$. On top of that we observed CO(3–2)/CO(1–0) ~ 1 in LARS 13 (also member of Group 1), which is consistent with highly excited gas that is thermalized even up to the CO J=3 level.

Our observations thus imply strong stellar feedback where Ly α photons may escape through channels in the ISM. Although the overall low gas content supports final escape, the photons need to travel significantly larger distances until they reach the point of last scattering. In this scenario the dust content thus plays an important role for Ly α to escape.

5.3 Robustness of our Results against GDR prescriptions

We test whether the high gas fractions and long total gas depletion times seen in Group 3 of LARS galaxies might be caused by the adopted power law in the gas-to-dust-ratio vs. metallicity prescription. For that purpose, we calculate depletion times and gas fractions using a constant GDR of 500. Given the fact that GDR=500 is slightly higher than the average GDR found from the aforementioned metallicity-dependent prescription, we find an average increase of the gas fraction of 5% for the whole sample. Roughly the same increase of 5% is seen for the three groups of LARS galaxies. This is not surprising given the fact that none of the groups are strongly biased towards lower or higher metallicities compared to the other groups. Thus, a constant GDR has no effect on the relative change of gas fractions or total gas depletion times among the groups of LARS galaxies and our results cannot be caused by an over-prediction of the dependence between GDR and metallicity.

6 Conclusion and Summary

LARS is a sample of 14 $z\sim 0$ star-forming galaxies that have continuum sizes, stellar masses and rest-frame absolute magnitudes similar to $2 < z < 3$ star-forming galaxies and massive Lyman Alpha emitters (Guaita et al., 2015).

In this paper, we present observations of LARS galaxies obtained with Herschel/PACS, SOFIA/FIFI-LS, the IRAM 30m telescope and APEX, targeting far-infrared continuum and emission lines of [C II]158 μm , [O I]63 μm and [O III]88 μm as well as low-J CO lines. In combination with archival far-infrared data (WISE, AKARI and IRAS), we applied the models of Draine and Li (2007) and derived parameters such as dust mass, average energy density and PDR mass using a Bayesian approach. Total gas masses were calculated for all LARS galaxies in a homogeneous way using a metallicity-dependent gas-to-dust ratio (GDR), allowing us to establish the Kennicutt-Schmidt relation for all 14 LARS galaxies (see Figure 10).

For those eight galaxies with a detection in [C II]158 μm , we compared the relative [C II]158 μm line strength to the total far-infrared luminosity (see Figure 13) and for five LARS galaxies – with detections of at least two emission lines – be it a finestructure or molecular line – a basic PDR analysis was performed, enabling us to estimate average PDR gas density and FUV radiation field strength (see Figure 24).

We have further applied novel radiative transfers models⁹ (Puschnig et al. in prep.), taking into account that molecular emission lines emerge from a multi-density medium (with a lognorm density distribution) rather than from a single density gas. Using multi-J CO, HCN (1-0) and HCO+ (1-0) observations of LARS 3 and 8, enabled us to derive mean mass-weighted molecular gas densities of these two galaxies.

From the analysis of our data we conclude the following:

- LARS covers a wide dynamic range in the derived properties, with FIR-based star formation rates from $\sim 0.5\text{--}100 M_{\odot} \text{ yr}^{-1}$, gas fractions between $\sim 15\text{--}80\%$ and gas depletion times ranging from a few hundred Myr up to more than 10 Gyr.
- The distribution of LARS galaxies in the Σ_{gas} vs. Σ_{SFR} is quite heterogeneous. However, after defining three groups of galaxies according to their gas depletion times, we observe that the group (LARS 1, 2, 4, 7) with the longest gas depletion times, i.e. relatively high gas surface densities (Σ_{gas}) and low star formation rate densities (Σ_{SFR}), has (by far) the highest Ly α escape fraction. A relatively strong \sim linear trend is found between Ly α escape fraction and total gas depletion time (see Figure 12). We argue that the Ly α escape in those galaxies is driven by accretion-induced turbulence in the star-forming gas that shifts the Ly α photons out of resonance close to the places where they originate (see Figure 14). This scenario is supported by several other findings: From previously published optical, H α and UV imaging, we recognize that these galaxies are very clumpy and most importantly do not show any form of strong bulge, in agreement with our finding of a low average energy density. We speculate that the clumps are the result of recent or ongoing cold gas accretion, which 1) triggered the clump formation and 2) injected turbulence that has not yet dissipated, and thus facilitates Ly α escape.
- Another grouping of LARS galaxies is found in the KS plot. They have relatively low gas surface densities Σ_{gas} that are more similar to observations in normal spirals or main sequence galaxies. However, their extreme star formation rate densities suggest very high star formation efficiencies (LARS 3, 5, 12, 13), corresponding to gas depletion times of a few 100Myr only. We argue that the Ly α escape in those galaxies (which is on the order of a few percent only) is facilitated by an environment that is radiation-dominated and highly ionized. This is supported by our observations of very high average energy densities (U_{min}). HST imaging of these galaxies further shows a compact, centralized light distribution in those galaxies. In such an environment Ly α most likely escapes through channels that are a product of strong stellar feedback. This scenario is also supported by high-J CO observations of LARS 13 that suggest highly excited gas that is thermalized at least up to the J=3 level. Further evidence is found from molecular gas radiative transfer modeling of LARS 3 that suggest very high *mean* molecular gas densities of $\sim 10^4 \text{ cm}^{-3}$. However, it seems that this scenario is less efficient in driving up Ly α escape fractions (compared to the previously described turbulence scenario found in other LARS galaxies), because the photons still undergo scatterings farther out in the halo (suggested by the longer scattering distances) and are thus more prone to dust absorption.
- We further report on an extreme [C II]158 μm excess in LARS 5, the highest [C II]-to-FIR ratio observed in a non-AGN galaxy to date. LARS 5 is known to have an extreme stellar driven outflow of gas. We find that the extreme [C II]158 μm line strength (corresponding to $\sim 14\pm 3\%$ of the FIR) must be related to the outflow as well. This is supported by the fact that the [C II]158 μm line is blueshifted compared to the systemic velocity.

⁹<http://www.densgastoolbox.com>

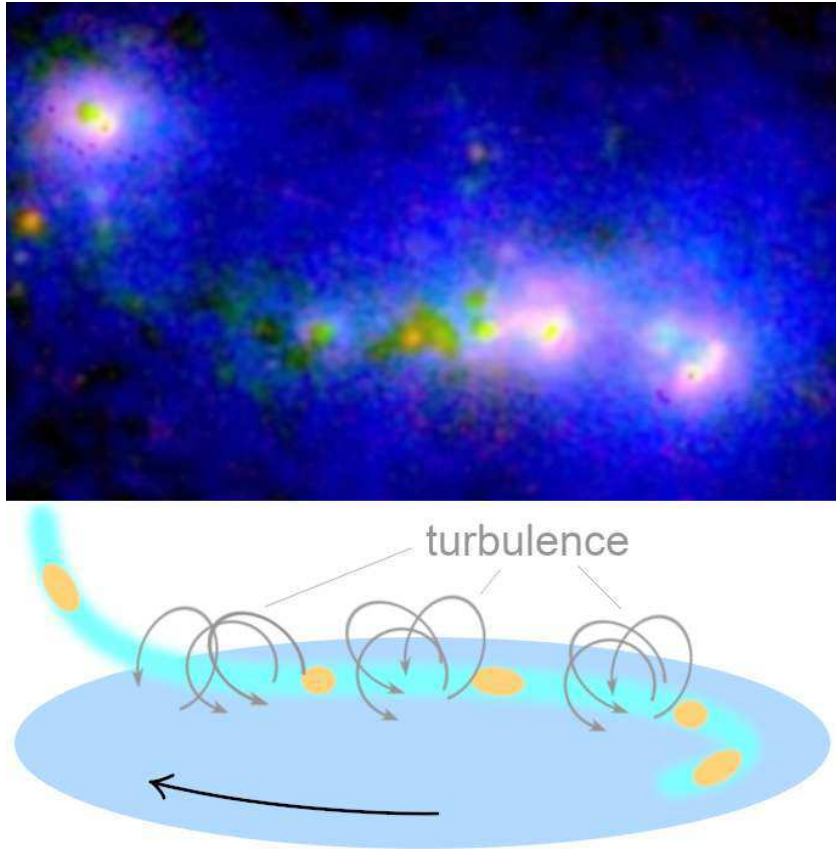


Figure 14. *Top:* RGB image of LARS 2 with red, green and blue channels encoding $H\alpha$, UV continuum and $Ly\alpha$ (scaled to show details). *Bottom:* Sketch of turbulence driven enhanced $Ly\alpha$ escape during disk formation.

Acknowledgements

JP owes special thanks to all IRAM Granada staff. In particular JP thanks Claudia Marka for numerous fruitful discussions, help with the heterodyne receiver setup and data reduction; Nicolas Billot for assigning additional telescope time when observing time was lost due to scheduling constraints or weather; Israel Hermelo for helping to create OTF scripts; Sandra Trevino for support during the first heterodyne pool week in September 2014; and Carsten Kramer for discussions about our observing strategy and absolute calibration accuracy. This work has benefited from research funding from the European Community's Seventh Framework Programme, which covered JP's travelling expenses for IRAM 30m observations connected to programs 082-14 and 064-15. M.H. acknowledges the support of the Swedish Research Council, Vetenskapsrådet and the Swedish National Space Board (SNSB), and is Fellow of the Knut and Alice Wallenberg Foundation. D.K. is supported by the Centre National d'Études Spatiales (CNES)/Centre National de la Recherche Scientifique (CNRS); convention no 131425. JP thanks all APEX staff in Chile, in particular Karl Torstensson for giving great support by enlightening new features of the data reduction environment GILDAS/CLASS. GILDAS is a collection of state-of-the-art softwares oriented toward (sub-)millimeter radioastronomical applications (either single-dish or interferometer). JP thanks Jérôme Pety and Sébastien Bardeau for help with GILDAS/CLASS related questions. This work also benefits from data obtained with the Herschel spacecraft, which was designed, built, tested, and launched under a contract to ESA managed by the Herschel/Planck Project team by an industrial consortium under the overall responsibility of the prime contractor Thales Alenia Space (Cannes), and including Astrium (Friedrichshafen) responsible for the payload module and for system testing at spacecraft level, Thales Alenia Space (Turin) responsible for the service module, and Astrium (Toulouse) responsible for the telescope, with in excess of a hundred subcontractors. This publication makes use of data products from the Wide-field Infrared Survey Explorer, which is a joint project of the University of California, Los Angeles, and the Jet Propulsion Laboratory/California Institute of Technology, funded by the National Aeronautics and Space Administration. This research is based on observations with AKARI, a JAXA project with the participation of ESA. This research has made use of the NASA/IPAC Infrared Science Archive, which is operated by the Jet Propulsion Laboratory, California Institute of Technology, under contract with the National Aeronautics and Space Administration. Funding for the Sloan Digital Sky Survey (SDSS) has been provided by the Alfred P. Sloan Foundation, the Participating Institutions, the National Aeronautics and Space Administration, the National

Science Foundation, the U.S. Department of Energy, the Japanese Monbukagakusho, and the Max Planck Society. The SDSS Web site is <http://www.sdss.org/>. The SDSS is managed by the Astrophysical Research Consortium (ARC) for the Participating Institutions. The Participating Institutions are The University of Chicago, Fermilab, the Institute for Advanced Study, the Japan Participation Group, The Johns Hopkins University, Los Alamos National Laboratory, the Max-Planck-Institute for Astronomy (MPIA), the Max-Planck-Institute for Astrophysics (MPA), New Mexico State University, University of Pittsburgh, Princeton University, the United States Naval Observatory, and the University of Washington. This research made use of Montage, funded by the National Aeronautics and Space Administration's Earth Science Technology Office, Computational Technologies Project, under Cooperative Agreement Number NCC5-626 between NASA and the California Institute of Technology. The code is maintained by the NASA/IPAC Infrared Science Archive.

References

- R. B. Partridge and P. J. E. Peebles. Are Young Galaxies Visible? *ApJ*, 147:868, March 1967. doi: 10.1086/149079.
- D. L. Meier and R. Terlevich. Extragalactic H II regions in the UV - Implications for primeval galaxies. *ApJ*, 246: L109–L113, June 1981. doi: 10.1086/183565.
- L. L. Cowie and E. M. Hu. High- z Ly α Emitters. I. A Blank-Field Search for Objects near Redshift $Z = 3.4$ in and around the Hubble Deep Field and the Hawaii Deep Field SSA 22. *AJ*, 115:1319–1328, April 1998. doi: 10.1086/300309.
- M. Ouchi, K. Shimasaku, M. Akiyama, C. Simpson, T. Saito, Y. Ueda, H. Furusawa, K. Sekiguchi, T. Yamada, T. Kodama, N. Kashikawa, S. Okamura, M. Iye, T. Takata, M. Yoshida, and M. Yoshida. The Subaru/XMM-Newton Deep Survey (SXDS). IV. Evolution of Ly α Emitters from $z = 3.1$ to 5.7 in the 1 deg^2 Field: Luminosity Functions and AGN. *ApJS*, 176:301–330, June 2008. doi: 10.1086/527673.
- M. Ouchi, K. Shimasaku, H. Furusawa, T. Saito, M. Yoshida, M. Akiyama, Y. Ono, T. Yamada, K. Ota, N. Kashikawa, M. Iye, T. Kodama, S. Okamura, C. Simpson, and M. Yoshida. Statistics of 207 Ly α Emitters at a Redshift Near 7: Constraints on Reionization and Galaxy Formation Models. *ApJ*, 723:869–894, November 2010. doi: 10.1088/0004-637X/723/1/869.
- J. J. Adams, J. M. Uson, G. J. Hill, and P. J. MacQueen. A New $z = 0$ Metagalactic Ultraviolet Background Limit. *ApJ*, 728:107, February 2011. doi: 10.1088/0004-637X/728/2/107.
- J. Matthee, D. Sobral, S. Santos, H. Röttgering, B. Darvish, and B. Mobasher. Identification of the brightest Ly α emitters at $z = 6.6$: implications for the evolution of the luminosity function in the reionization era. *MNRAS*, 451: 400–417, July 2015. doi: 10.1093/mnras/stv947.
- S. Santos, D. Sobral, and J. Matthee. The Ly α luminosity function at $z = 5.7 - 6.6$ and the steep drop of the faint end: implications for reionization. *MNRAS*, 463:1678–1691, December 2016. doi: 10.1093/mnras/stw2076.
- E. C. Herenz, T. Urrutia, L. Wisotzki, J. Kerutt, R. Saust, M. Werhahn, K. B. Schmidt, J. Caruana, C. Diener, R. Bacon, J. Brinchmann, J. Schaye, M. Maseda, and P. M. Weilbacher. The MUSE-Wide survey: A first catalogue of 831 emission line galaxies. *A&A*, 606:A12, September 2017. doi: 10.1051/0004-6361/201731055.
- D. Sobral, S. Santos, J. Matthee, A. Paulino-Afonso, B. Ribeiro, J. Calhau, and A. A. Khostovan. Slicing COSMOS with SC4K: the evolution of typical Ly α emitters and the Ly α escape fraction from $z \sim 2$ to 6. *MNRAS*, 476: 4725–4752, June 2018. doi: 10.1093/mnras/sty378.
- T. Urrutia, L. Wisotzki, J. Kerutt, K. B. Schmidt, E. C. Herenz, J. Klar, R. Saust, M. Werhahn, C. Diener, J. Caruana, D. Krajinović, R. Bacon, L. Boogaard, J. Brinchmann, H. Enke, M. Maseda, T. Nanayakkara, J. Richard, M. Steinmetz, and P. M. Weilbacher. The MUSE-Wide Survey: survey description and first data release. *A&A*, 624: A141, Apr 2019. doi: 10.1051/0004-6361/201834656.
- D. A. Neufeld. The transfer of resonance-line radiation in static astrophysical media. *ApJ*, 350:216–241, February 1990. doi: 10.1086/168375.

-
- S.-H. Ahn, H.-W. Lee, and H. M. Lee. $\text{Ly}\alpha$ Line Formation in Starbursting Galaxies. I. Moderately Thick, Dustless, and Static H I Media. *ApJ*, 554:604–614, June 2001. doi: 10.1086/321374.
- S.-H. Ahn, H.-W. Lee, and H. M. Lee. $\text{Ly}\alpha$ Line Formation in Starbursting Galaxies. II. Extremely Thick, Dustless, and Static H I Media. *ApJ*, 567:922–930, March 2002. doi: 10.1086/338497.
- M. Dijkstra, Z. Haiman, and M. Spaans. $\text{Ly}\alpha$ Radiation from Collapsing Protogalaxies. I. Characteristics of the Emergent Spectrum. *ApJ*, 649:14–36, September 2006a. doi: 10.1086/506243.
- M. Dijkstra, Z. Haiman, and M. Spaans. $\text{Ly}\alpha$ Radiation from Collapsing Protogalaxies. II. Observational Evidence for Gas Infall. *ApJ*, 649:37–47, September 2006b. doi: 10.1086/506244.
- A. Verhamme, D. Schaerer, and A. Maselli. 3D $\text{Ly}\alpha$ radiation transfer. I. Understanding $\text{Ly}\alpha$ line profile morphologies. *A&A*, 460:397–413, December 2006. doi: 10.1051/0004-6361:20065554.
- D. Schaerer and A. Verhamme. 3D $\text{Ly}\alpha$ radiation transfer. II. Fitting the Lyman break galaxy MS 1512-cB58 and implications for $\text{Ly}\alpha$ emission in high- z starbursts. *A&A*, 480:369–377, March 2008. doi: 10.1051/0004-6361:20078913.
- A. Verhamme, D. Schaerer, H. Atek, and C. Tapken. 3D $\text{Ly}\alpha$ radiation transfer. III. Constraints on gas and stellar properties of $z \sim 3$ Lyman break galaxies (LBG) and implications for high- z LBGs and $\text{Ly}\alpha$ emitters. *A&A*, 491: 89–111, November 2008. doi: 10.1051/0004-6361:200809648.
- M. Hayes, G. Östlin, D. Schaerer, J. M. Mas-Hesse, C. Leitherer, H. Atek, D. Kunth, A. Verhamme, S. de Barros, and J. Melinder. Escape of about five per cent of Lyman- α photons from high-redshift star-forming galaxies. *Nature*, 464: 562–565, March 2010. doi: 10.1038/nature08881.
- C. Scarlata, J. Colbert, H. I. Teplitz, N. Panagia, M. Hayes, B. Siana, A. Rau, P. Francis, A. Caon, A. Pizzella, and C. Bridge. The Effect of Dust Geometry on the $\text{Ly}\alpha$ Output of Galaxies. *ApJ*, 704:L98–L102, October 2009. doi: 10.1088/0004-637X/704/2/L98.
- Zhen-Ya Zheng, Junxian Wang, James Rhoads, Leopoldo Infante, Sangeeta Malhotra, Weida Hu, Alistair R. Walker, Linhua Jiang, Chunyan Jiang, Pascale Hibon, Alicia Gonzalez, Xu Kong, XianZhong Zheng, Gaspar Galaz, and L. Felipe Barrientos. First Results from the Lyman Alpha Galaxies in the Epoch of Reionization (LAGER) Survey: Cosmological Reionization at $z \sim 7$. *ApJ*, 842(2):L22, Jun 2017. doi: 10.3847/2041-8213/aa794f.
- Daniel Kunth, J. M. Mas-Hesse, E. Terlevich, R. Terlevich, J. Lequeux, and S. Michael Fall. HST study of Lyman-alpha emission in star-forming galaxies: the effect of neutral gas flows. *A&A*, 334:11–20, Jun 1998.
- J. M. Cannon, N. M. McClure-Griffiths, E. D. Skillman, and S. Côté. The Complex Neutral Gas Dynamics of the Dwarf Starburst Galaxy NGC 625. *ApJ*, 607:274–284, May 2004. doi: 10.1086/383408.
- Aida Wofford, Claus Leitherer, and John Salzer. $\text{Ly}\alpha$ Escape from $z \sim 0.03$ Star-forming Galaxies: The Dominant Role of Outflows. *ApJ*, 765(2):118, Mar 2013. doi: 10.1088/0004-637X/765/2/118.
- S. A. Pardy, J. M. Cannon, G. Östlin, M. Hayes, T. Rivera-Thorsen, A. Sandberg, A. Adamo, E. Freeland, E. C. Herenz, L. Guaita, D. Kunth, P. Laursen, J. M. Mas-Hesse, J. Melinder, I. Orlitová, H. Otí-Floranes, J. Puschignig, D. Schaerer, and A. Verhamme. The Lyman Alpha Reference Sample. III. Properties of the Neutral ISM from GBT and VLA Observations. *ApJ*, 794:101, October 2014. doi: 10.1088/0004-637X/794/2/101.
- G. Tenorio-Tagle, S. A. Silich, D. Kunth, E. Terlevich, and R. Terlevich. The evolution of superbubbles and the detection of $\text{Ly}\alpha$ in star-forming galaxies. *MNRAS*, 309:332–342, October 1999. doi: 10.1046/j.1365-8711.1999.02809.x.
- J. M. Mas-Hesse, D. Kunth, G. Tenorio-Tagle, C. Leitherer, R. J. Terlevich, and E. Terlevich. $\text{Ly}\alpha$ Emission in Starbursts: Implications for Galaxies at High Redshift. *ApJ*, 598:858–877, December 2003. doi: 10.1086/379116.
- F. Duval, D. Schaerer, G. Östlin, and P. Laursen. Lyman α line and continuum radiative transfer in a clumpy interstellar medium. *A&A*, 562:A52, February 2014. doi: 10.1051/0004-6361/201220455.
-

-
- A. E. Jaskot and M. S. Oey. Linking Ly α and Low-ionization Transitions at Low Optical Depth. *ApJ*, 791(2):L19, Aug 2014. doi: 10.1088/2041-8205/791/2/L19.
- M. Hayes. Lyman Alpha Emitting Galaxies in the Nearby Universe. *PASA*, 32:e027, July 2015. doi: 10.1017/pasa.2015.25.
- J. S. Bridge, M. Hayes, J. Melinder, G. Östlin, C. Gronwall, R. Ciardullo, H. Atek, J. M. Cannon, M. Gronke, L. Guaita, A. Hagen, E. C. Herenz, D. Kunth, P. Laursen, J. M. Mas-Hesse, and S. A. Pardy. The Ly α Reference Sample. VIII. Characterizing Ly α Scattering in Nearby Galaxies. *ApJ*, 852:9, January 2018. doi: 10.3847/1538-4357/aa9932.
- A. Verhamme, I. Orlitová, D. Schaerer, and M. Hayes. Using Lyman- α to detect galaxies that leak Lyman continuum. *A&A*, 578:A7, June 2015. doi: 10.1051/0004-6361/201423978.
- J. Puschnig, M. Hayes, G. Östlin, T. E. Rivera-Thorsen, J. Melinder, J. M. Cannon, V. Menacho, E. Zackrisson, N. Bergvall, and E. Leitert. The Lyman continuum escape and ISM properties in Tololo 1247-232 - new insights from HST and VLA. *MNRAS*, 469:3252–3269, August 2017. doi: 10.1093/mnras/stx951.
- Ryan F. Trainor, Allison L. Strom, Charles C. Steidel, Gwen C. Rudie, Yuguang Chen, and Rachel L. Theios. Predicting Ly α Emission from Galaxies via Empirical Markers of Production and Escape in the KBSS. *ApJ*, 887(1):85, December 2019. doi: 10.3847/1538-4357/ab4993.
- David Sobral and Jorryt Matthee. Predicting Ly α escape fractions with a simple observable. Ly α in emission as an empirically calibrated star formation rate indicator. *A&A*, 623:A157, Mar 2019. doi: 10.1051/0004-6361/201833075.
- Axel Runnholm, Matthew Hayes, Jens Melinder, Emil Rivera-Thorsen, Göran Östlin, John Cannon, and Daniel Kunth. Lyman Alpha Reference Sample: X. Predicting Lyman alpha output from starforming galaxies using multivariate regression. *arXiv e-prints*, art. arXiv:2002.12378, February 2020.
- M. Hayes, G. Östlin, D. Schaerer, A. Verhamme, J. M. Mas-Hesse, A. Adamo, H. Atek, J. M. Cannon, F. Duval, L. Guaita, E. C. Herenz, D. Kunth, P. Laursen, J. Melinder, I. Orlitová, H. Oti-Flornes, and A. Sandberg. The Lyman Alpha Reference Sample: Extended Lyman Alpha Halos Produced at Low Dust Content. *ApJ*, 765:L27, March 2013. doi: 10.1088/2041-8205/765/2/L27.
- M. Hayes, G. Östlin, F. Duval, A. Sandberg, L. Guaita, J. Melinder, A. Adamo, D. Schaerer, A. Verhamme, I. Orlitová, J. M. Mas-Hesse, J. M. Cannon, H. Atek, D. Kunth, P. Laursen, H. Oti-Flornes, S. Pardy, T. Rivera-Thorsen, and E. C. Herenz. The Lyman Alpha Reference Sample. II. Hubble Space Telescope Imaging Results, Integrated Properties, and Trends. *ApJ*, 782:6, February 2014. doi: 10.1088/0004-637X/782/1/6.
- G. Östlin, M. Hayes, F. Duval, A. Sandberg, T. Rivera-Thorsen, T. Marquart, I. Orlitová, A. Adamo, J. Melinder, L. Guaita, H. Atek, J. M. Cannon, P. Gruyters, E. C. Herenz, D. Kunth, P. Laursen, J. M. Mas-Hesse, G. Micheva, H. Oti-Flornes, S. A. Pardy, M. M. Roth, D. Schaerer, and A. Verhamme. The Ly α Reference Sample. I. Survey Outline and First Results for Markarian 259. *ApJ*, 797:11, December 2014. doi: 10.1088/0004-637X/797/1/11.
- Lennox L. Cowie, Amy J. Barger, and Esther M. Hu. Ly α Emitting Galaxies as Early Stages in Galaxy Formation. *ApJ*, 738(2):136, Sep 2011. doi: 10.1088/0004-637X/738/2/136.
- T. E. Rivera-Thorsen, M. Hayes, G. Östlin, F. Duval, I. Orlitová, A. Verhamme, J. M. Mas-Hesse, D. Schaerer, J. M. Cannon, H. Oti-Flornes, A. Sandberg, L. Guaita, A. Adamo, H. Atek, E. C. Herenz, D. Kunth, P. Laursen, and J. Melinder. The Lyman Alpha Reference Sample. V. The Impact of Neutral ISM Kinematics and Geometry on Ly α Escape. *ApJ*, 805:14, May 2015. doi: 10.1088/0004-637X/805/1/14.
- G. Micheva, G. Östlin, E. Zackrisson, M. Hayes, J. Melinder, L. Guaita, J. M. Cannon, J. S. Bridge, D. Kunth, and A. Sandberg. The Lyman Alpha Reference Sample. IX. Revelations from deep surface photometry. *A&A*, 615:A46, July 2018. doi: 10.1051/0004-6361/201832584.
-

-
- E. C. Herenz, P. Gruyters, I. Orlitova, M. Hayes, G. Östlin, J. M. Cannon, M. M. Roth, A. Bik, S. Pardy, H. Otí-Floranes, J. M. Mas-Hesse, A. Adamo, H. Atek, F. Duval, L. Guaita, D. Kunth, P. Laursen, J. Melinder, J. Puschnig, T. E. Rivera-Thorsen, D. Schaerer, and A. Verhamme. The Lyman alpha reference sample. VII. Spatially resolved H α kinematics. *A&A*, 587:A78, March 2016. doi: 10.1051/0004-6361/201527373.
- M. Schmidt. The Rate of Star Formation. *ApJ*, 129:243, March 1959. doi: 10.1086/146614.
- R. C. Kennicutt, Jr. The Global Schmidt Law in Star-forming Galaxies. *ApJ*, 498:541–552, May 1998. doi: 10.1086/305588.
- T. Wong and L. Blitz. The Relationship between Gas Content and Star Formation in Molecule-rich Spiral Galaxies. *ApJ*, 569:157–183, April 2002. doi: 10.1086/339287.
- F. Bigiel, A. Leroy, F. Walter, E. Brinks, W. J. G. de Blok, B. Madore, and M. D. Thornley. The Star Formation Law in Nearby Galaxies on Sub-Kpc Scales. *AJ*, 136:2846–2871, December 2008. doi: 10.1088/0004-6256/136/6/2846.
- F. Bigiel, A. K. Leroy, F. Walter, E. Brinks, W. J. G. de Blok, C. Kramer, H. W. Rix, A. Schruba, K.-F. Schuster, A. Usero, and H. W. Wiesemeyer. A Constant Molecular Gas Depletion Time in Nearby Disk Galaxies. *ApJ*, 730:L13, April 2011. doi: 10.1088/2041-8205/730/2/L13.
- A. K. Leroy, F. Walter, E. Brinks, F. Bigiel, W. J. G. de Blok, B. Madore, and M. D. Thornley. The Star Formation Efficiency in Nearby Galaxies: Measuring Where Gas Forms Stars Effectively. *AJ*, 136:2782–2845, December 2008. doi: 10.1088/0004-6256/136/6/2782.
- A. K. Leroy, F. Walter, K. Sandstrom, A. Schruba, J.-C. Muñoz-Mateos, F. Bigiel, A. Bolatto, E. Brinks, W. J. G. de Blok, S. Meidt, H.-W. Rix, E. Rosolowsky, E. Schinnerer, K.-F. Schuster, and A. Usero. Molecular Gas and Star Formation in nearby Disk Galaxies. *AJ*, 146:19, August 2013. doi: 10.1088/0004-6256/146/2/19.
- A. D. Bolatto, T. Wong, D. Utomo, L. Blitz, S. N. Vogel, S. F. Sánchez, J. Barrera-Ballesteros, Y. Cao, D. Colombo, H. Dannerbauer, R. García-Benito, R. Herrera-Camus, B. Husemann, V. Kalinova, A. K. Leroy, G. Leung, R. C. Levy, D. Mast, E. Ostriker, E. Rosolowsky, K. M. Sandstrom, P. Teuben, G. van de Ven, and F. Walter. The EDGE-CALIFA Survey: Interferometric Observations of 126 Galaxies with CARMA. *ApJ*, 846:159, September 2017. doi: 10.3847/1538-4357/aa86aa.
- D. Utomo, J. Sun, A. K. Leroy, J. M. D. Kruijssen, E. Schinnerer, A. Schruba, F. Bigiel, G. A. Blanc, M. Chevance, E. Emsellem, C. Herrera, A. P. S. Hygate, K. Kreckel, E. C. Ostriker, J. Pety, M. Querejeta, E. Rosolowsky, K. M. Sandstrom, and A. Usero. Star Formation Efficiency per Free-fall Time in nearby Galaxies. *ApJ*, 861:L18, July 2018. doi: 10.3847/2041-8213/aac8f8f.
- D. Colombo, V. Kalinova, D. Utomo, E. Rosolowsky, A. D. Bolatto, R. C. Levy, T. Wong, S. F. Sanchez, A. K. Leroy, E. Ostriker, L. Blitz, S. Vogel, D. Mast, R. García-Benito, B. Husemann, H. Dannerbauer, L. Ellmeier, and Y. Cao. The EDGE-CALIFA survey: the influence of galactic rotation on the molecular depletion time across the Hubble sequence. *MNRAS*, 475:1791–1808, April 2018. doi: 10.1093/mnras/stx3233.
- J. Wu, N. J. Evans, II, Y. Gao, P. M. Solomon, Y. L. Shirley, and P. A. Vanden Bout. Connecting Dense Gas Tracers of Star Formation in our Galaxy to High-z Star Formation. *ApJ*, 635:L173–L176, December 2005. doi: 10.1086/499623.
- A. Schruba, A. K. Leroy, F. Walter, F. Bigiel, E. Brinks, W. J. G. de Blok, G. Dumas, C. Kramer, E. Rosolowsky, K. Sandstrom, K. Schuster, A. Usero, A. Weiss, and H. Wiesemeyer. A Molecular Star Formation Law in the Atomic-gas-dominated Regime in Nearby Galaxies. *AJ*, 142:37, August 2011. doi: 10.1088/0004-6256/142/2/37.
- A. D. Bolatto, A. K. Leroy, K. Jameson, E. Ostriker, K. Gordon, B. Lawton, S. Stanimirović, F. P. Israel, S. C. Madden, S. Hony, K. M. Sandstrom, C. Bot, M. Rubio, P. F. Winkler, J. Roman-Duval, J. T. van Loon, J. M. Oliveira, and R. Indebetouw. The State of the Gas and the Relation between Gas and Star Formation at Low Metallicity: The Small Magellanic Cloud. *ApJ*, 741:12, November 2011. doi: 10.1088/0004-637X/741/1/12.
-

-
- K. E. Jameson, A. D. Bolatto, A. K. Leroy, M. Meixner, J. Roman-Duval, K. Gordon, A. Hughes, F. P. Israel, M. Rubio, R. Indebetouw, S. C. Madden, C. Bot, S. Hony, D. Cormier, E. W. Pellegrini, M. Galametz, and G. Sonneborn. The Relationship Between Molecular Gas, H I, and Star Formation in the Low-mass, Low-metallicity Magellanic Clouds. *ApJ*, 825:12, July 2016. doi: 10.3847/0004-637X/825/1/12.
- V. A. Semenov, A. V. Kravtsov, and N. Y. Gnedin. What Sets the Slope of the Molecular Kennicutt-Schmidt Relation? *ApJ*, 870:79, January 2019. doi: 10.3847/1538-4357/aaf163.
- N. J. Evans, II, M. M. Dunham, J. K. Jørgensen, M. L. Enoch, B. Merín, E. F. van Dishoeck, J. M. Alcalá, P. C. Myers, K. R. Stapelfeldt, T. L. Huard, L. E. Allen, P. M. Harvey, T. van Kempen, G. A. Blake, D. W. Koerner, L. G. Mundy, D. L. Padgett, and A. I. Sargent. The Spitzer c2d Legacy Results: Star-Formation Rates and Efficiencies; Evolution and Lifetimes. *ApJS*, 181:321–350, April 2009. doi: 10.1088/0067-0049/181/2/321.
- N. J. Evans, II, A. Heiderman, and N. Vutisalchavakul. Star Formation Relations in Nearby Molecular Clouds. *ApJ*, 782:114, February 2014. doi: 10.1088/0004-637X/782/2/114.
- A. Heiderman, N. J. Evans, II, L. E. Allen, T. Huard, and M. Heyer. The Star Formation Rate and Gas Surface Density Relation in the Milky Way: Implications for Extragalactic Studies. *ApJ*, 723:1019–1037, November 2010. doi: 10.1088/0004-637X/723/2/1019.
- R. A. Gutermuth, J. L. Pipher, S. T. Megeath, P. C. Myers, L. E. Allen, and T. S. Allen. A Correlation between Surface Densities of Young Stellar Objects and Gas in Eight Nearby Molecular Clouds. *ApJ*, 739:84, October 2011. doi: 10.1088/0004-637X/739/2/84.
- R. Genzel, L. J. Tacconi, J. Gracia-Carpio, A. Sternberg, M. C. Cooper, K. Shapiro, A. Bolatto, N. Bouché, F. Bournaud, A. Burkert, F. Combes, J. Comerford, P. Cox, M. Davis, N. M. F. Schreiber, S. Garcia-Burillo, D. Lutz, T. Naab, R. Neri, A. Omont, A. Shapley, and B. Weiner. A study of the gas-star formation relation over cosmic time. *MNRAS*, 407:2091–2108, October 2010. doi: 10.1111/j.1365-2966.2010.16969.x.
- R. Genzel, L. J. Tacconi, D. Lutz, A. Saintonge, S. Berta, B. Magnelli, F. Combes, S. García-Burillo, R. Neri, A. Bolatto, T. Contini, S. Lilly, J. Boissier, F. Boone, N. Bouché, F. Bournaud, A. Burkert, M. Carollo, L. Colina, M. C. Cooper, P. Cox, C. Feruglio, N. M. Förster Schreiber, J. Freundlich, J. Gracia-Carpio, S. Juneau, K. Kovac, M. Lippa, T. Naab, P. Salome, A. Renzini, A. Sternberg, F. Walter, B. Weiner, A. Weiss, and S. Wuyts. Combined CO and Dust Scaling Relations of Depletion Time and Molecular Gas Fractions with Cosmic Time, Specific Star-formation Rate, and Stellar Mass. *ApJ*, 800:20, February 2015. doi: 10.1088/0004-637X/800/1/20.
- D. Calzetti, G. W. Wilson, B. T. Draine, H. Roussel, K. E. Johnson, M. H. Heyer, W. F. Wall, K. Grasha, A. Battisti, J. E. Andrews, A. Kirkpatrick, D. Rosa González, O. Vega, J. Puschig, M. Yun, G. Östlin, A. S. Evans, Y. Tang, J. Lowenthal, and D. Sánchez-Argüelles. Spatially Resolved Dust, Gas, and Star Formation in the Dwarf Magellanic Irregular NGC 4449. *ApJ*, 852:106, January 2018. doi: 10.3847/1538-4357/aaa1e2.
- Y. Gao and P. M. Solomon. HCN Survey of Normal Spiral, Infrared-luminous, and Ultraluminous Galaxies. *ApJS*, 152: 63–80, May 2004a. doi: 10.1086/383003.
- Y. Gao and P. M. Solomon. The Star Formation Rate and Dense Molecular Gas in Galaxies. *ApJ*, 606:271–290, May 2004b. doi: 10.1086/382999.
- Charles J. Lada, Marco Lombardi, and João F. Alves. On the Star Formation Rates in Molecular Clouds. *ApJ*, 724(1): 687–693, Nov 2010. doi: 10.1088/0004-637X/724/1/687.
- Charles J. Lada, Jan Forbrich, Marco Lombardi, and João F. Alves. Star Formation Rates in Molecular Clouds and the Nature of the Extragalactic Scaling Relations. *ApJ*, 745(2):190, Feb 2012. doi: 10.1088/0004-637X/745/2/190.
- F. Bigiel, A. K. Leroy, M. J. Jiménez-Donaire, J. Pety, A. Usero, D. Cormier, A. Bolatto, S. Garcia-Burillo, D. Colombo, M. González-García, A. Hughes, A. A. Kepley, C. Kramer, K. Sandstrom, E. Schinnerer, A. Schrubba, K. Schuster, N. Tomićic, and L. Zschaechner. The EMPIRE Survey: Systematic Variations in the Dense Gas Fraction and Star Formation Efficiency from Full-disk Mapping of M51. *ApJ*, 822:L26, May 2016. doi: 10.3847/2041-8205/822/2/L26.
-

-
- María J. Jiménez-Donaire, F. Bigiel, A. K. Leroy, A. Usero, D. Cormier, J. Puschign, M. Gallagher, A. Kepley, A. Bolatto, S. García-Burillo, A. Hughes, C. Kramer, J. Pety, E. Schinnerer, A. Schrubba, K. Schuster, and F. Walter. EMPIRE: The IRAM 30 m Dense Gas Survey of Nearby Galaxies. *ApJ*, 880(2):127, Aug 2019. doi: 10.3847/1538-4357/ab2b95.
- J. M. Diederik Kruijssen, Andreas Schrubba, Mélanie Chevance, Steven N. Longmore, Alexander P. S. Hygate, Daniel T. Haydon, Anna F. McLeod, Julianne J. Dalcanton, Linda J. Tacconi, and Ewine F. van Dishoeck. Fast and inefficient star formation due to short-lived molecular clouds and rapid feedback. *Nature*, 569(7757):519–522, May 2019. doi: 10.1038/s41586-019-1194-3.
- P. Popesso, A. Concas, L. Morselli, C. Schreiber, G. Rodighiero, G. Cresci, S. Belli, G. Erfanianfar, C. Mancini, H. Inami, M. Dickinson, O. Ilbert, M. Pannella, and D. Elbaz. The main sequence of star-forming galaxies - I. The local relation and its bending. *MNRAS*, 483:3213–3226, March 2019. doi: 10.1093/mnras/sty3210.
- J. Brinchmann, S. Charlot, S. D. M. White, C. Tremonti, G. Kauffmann, T. Heckman, and J. Brinkmann. The physical properties of star-forming galaxies in the low-redshift Universe. *MNRAS*, 351:1151–1179, July 2004. doi: 10.1111/j.1365-2966.2004.07881.x.
- K. G. Noeske, S. M. Faber, B. J. Weiner, D. C. Koo, J. R. Primack, A. Dekel, C. Papovich, C. J. Conselice, E. Le Floch, G. H. Rieke, A. L. Coil, J. M. Lotz, R. S. Somerville, and K. Bundy. Star Formation in AEGIS Field Galaxies since $z=1.1$: Staged Galaxy Formation and a Model of Mass-dependent Gas Exhaustion. *ApJ*, 660:L47–L50, May 2007. doi: 10.1086/517927.
- E. Daddi, M. Dickinson, G. Morrison, R. Chary, A. Cimatti, D. Elbaz, D. Frayer, A. Renzini, A. Pope, D. M. Alexander, F. E. Bauer, M. Giavalisco, M. Huynh, J. Kurk, and M. Mignoli. Multiwavelength Study of Massive Galaxies at z^2 . I. Star Formation and Galaxy Growth. *ApJ*, 670:156–172, November 2007. doi: 10.1086/521818.
- D. Elbaz, E. Daddi, D. Le Borgne, M. Dickinson, D. M. Alexander, R.-R. Chary, J.-L. Starck, W. N. Brandt, M. Kitzbichler, E. MacDonald, M. Nonino, P. Popesso, D. Stern, and E. Vanzella. The reversal of the star formation-density relation in the distant universe. *A&A*, 468:33–48, June 2007. doi: 10.1051/0004-6361:20077525.
- Y.-j. Peng, S. J. Lilly, K. Kovač, M. Bolzonella, L. Pozzetti, A. Renzini, G. Zamorani, O. Ilbert, C. Knobel, A. Iovino, C. Maier, O. Cucciati, L. Tasca, C. M. Carollo, J. Silverman, P. Kampanyk, L. de Ravel, D. Sanders, N. Scoville, T. Contini, V. Mainieri, M. Scodreggio, J.-P. Kneib, O. Le Fèvre, S. Bardelli, A. Bongiorno, K. Caputi, G. Coppola, S. de la Torre, P. Franzetti, B. Garilli, F. Lamareille, J.-F. Le Borgne, V. Le Brun, M. Mignoli, E. Perez Montero, R. Pello, E. Ricciardelli, M. Tanaka, L. Tresse, D. Vergani, N. Welikala, E. Zucca, P. Oesch, U. Abbas, L. Barnes, R. Bordoloi, D. Bottini, A. Cappi, P. Cassata, A. Cimatti, M. Fumana, G. Hasinger, A. Koekemoer, A. Leauthaud, D. Maccagni, C. Marinoni, H. McCracken, P. Memeo, B. Meneux, P. Nair, C. Porciani, V. Presotto, and R. Scaramella. Mass and Environment as Drivers of Galaxy Evolution in SDSS and zCOSMOS and the Origin of the Schechter Function. *ApJ*, 721:193–221, September 2010. doi: 10.1088/0004-637X/721/1/193.
- S. Wuyts, N. M. Förster Schreiber, A. van der Wel, B. Magnelli, Y. Guo, R. Genzel, D. Lutz, H. Aussel, G. Barro, S. Berta, A. Cava, J. Graciá-Carpio, N. P. Hathi, K.-H. Huang, D. D. Kocevski, A. M. Koekemoer, K.-S. Lee, E. Le Floch, E. J. McGrath, R. Nordon, P. Popesso, F. Pozzi, L. Riguccini, G. Rodighiero, A. Saintonge, and L. Tacconi. Galaxy Structure and Mode of Star Formation in the SFR-Mass Plane from $z \sim 2.5$ to $z \sim 0.1$. *ApJ*, 742:96, December 2011. doi: 10.1088/0004-637X/742/2/96.
- K. E. Whitaker, P. G. van Dokkum, G. Brammer, and M. Franx. The Star Formation Mass Sequence Out to $z = 2.5$. *ApJ*, 754:L29, August 2012. doi: 10.1088/2041-8205/754/2/L29.
- K. E. Whitaker, M. Franx, J. Leja, P. G. van Dokkum, A. Henry, R. E. Skelton, M. Fumagalli, I. G. Momcheva, G. B. Brammer, I. Labbé, E. J. Nelson, and J. R. Rigby. Constraining the Low-mass Slope of the Star Formation Sequence at $0.5 < z < 2.5$. *ApJ*, 795:104, November 2014. doi: 10.1088/0004-637X/795/2/104.
- A. R. Tomczak, R. F. Quadri, K.-V. H. Tran, I. Labbé, C. M. S. Straatman, C. Papovich, K. Glazebrook, R. Allen, G. B. Brammer, M. Cowley, M. Dickinson, D. Elbaz, H. Inami, G. G. Kacprzak, G. E. Morrison, T. Nanayakkara, S. E.
-

-
- Persson, G. A. Rees, B. Salmon, C. Schreiber, L. R. Spitler, and K. E. Whitaker. The SFR-M* Relation and Empirical Star-Formation Histories from ZFOURGE* at $0.5 < z < 4$. *ApJ*, 817:118, February 2016. doi: 10.3847/0004-637X/817/2/118.
- G. Rodighiero, E. Daddi, I. Baronchelli, A. Cimatti, A. Renzini, H. Aussel, P. Popesso, D. Lutz, P. Andreani, S. Berta, A. Cava, D. Elbaz, A. Feltre, A. Fontana, N. M. Förster Schreiber, A. Franceschini, R. Genzel, A. Grazian, C. Gruppioni, O. Ilbert, E. Le Floch, G. Magdis, M. Magliocchetti, B. Magnelli, R. Maiolino, H. McCracken, R. Nordon, A. Poglitsch, P. Santini, F. Pozzi, L. Riguccini, L. J. Tacconi, S. Wuyts, and G. Zamorani. The Lesser Role of Starbursts in Star Formation at $z = 2$. *ApJ*, 739(2):L40, Oct 2011. doi: 10.1088/2041-8205/739/2/L40.
- L. J. Tacconi, R. Neri, R. Genzel, F. Combes, A. Bolatto, M. C. Cooper, S. Wuyts, F. Bournaud, A. Burkert, J. Comerford, P. Cox, M. Davis, N. M. Förster Schreiber, S. García-Burillo, J. Gracia-Carpio, D. Lutz, T. Naab, S. Newman, A. Omont, A. Saintonge, K. Shapiro Griffin, A. Shapley, A. Sternberg, and B. Weiner. Phibbs: Molecular Gas Content and Scaling Relations in $z \sim 1-3$ Massive, Main-sequence Star-forming Galaxies. *ApJ*, 768:74, May 2013. doi: 10.1088/0004-637X/768/1/74.
- N. Scoville, N. Lee, P. Vanden Bout, T. Diaz-Santos, D. Sanders, B. Darvish, A. Bongiorno, C. M. Casey, L. Murchikova, J. Koda, P. Capak, C. Vlahakis, O. Ilbert, K. Sheth, K. Morokuma-Matsui, R. J. Ivison, H. Aussel, C. Laigle, H. J. McCracken, L. Armus, A. Pope, S. Toft, and D. Masters. Evolution of Interstellar Medium, Star Formation, and Accretion at High Redshift. *ApJ*, 837:150, March 2017. doi: 10.3847/1538-4357/aa61a0.
- A. A. Hakobyan, V. Z. Adibekyan, L. S. Aramyan, A. R. Petrosian, J. M. Gomes, G. A. Mamon, D. Kunth, and M. Turatto. Supernovae and their host galaxies. I. The SDSS DR8 database and statistics. *A&A*, 544:A81, August 2012. doi: 10.1051/0004-6361/201219541.
- F. Duval, G. Östlin, M. Hayes, E. Zackrisson, A. Verhamme, I. Orlitova, A. Adamo, L. Guaita, J. Melinder, J. M. Cannon, P. Laursen, T. Rivera-Thorsen, E. C. Herenz, P. Gruyters, J. M. Mas-Hesse, D. Kunth, A. Sandberg, D. Schaerer, and T. Månsson. The Lyman alpha reference sample. VI. Lyman alpha escape from the edge-on disk galaxy Mrk 1486. *A&A*, 587:A77, March 2016. doi: 10.1051/0004-6361/201526876.
- R. Güsten, L. Å. Nyman, P. Schilke, K. Menten, C. Cesarsky, and R. Booth. The Atacama Pathfinder EXperiment (APEX) - a new submillimeter facility for southern skies -. *A&A*, 454:L13–L16, August 2006. doi: 10.1051/0004-6361:20065420.
- V. Belitsky, I. Lapkin, R. Monje, V. Vassilev, C. Risacher, A. Pavolotsky, D. Meledin, M. Olberg, M. Pantaleev, and R. Booth. Heterodyne single-pixel facility instrumentation for the APEX Telescope. In *Society of Photo-Optical Instrumentation Engineers (SPIE) Conference Series*, volume 6275 of Proc. SPIE, page 62750G, June 2006. doi: 10.1117/12.671383.
- V. Vassilev, D. Meledin, I. Lapkin, V. Belitsky, O. Nyström, D. Henke, A. Pavolotsky, R. Monje, C. Risacher, M. Olberg, M. Strandberg, E. Sundin, M. Fredrixon, S.-E. Ferm, V. Desmaris, D. Dochev, M. Pantaleev, P. Bergman, and H. Olofsson. A Swedish heterodyne facility instrument for the APEX telescope. *A&A*, 490:1157–1163, November 2008. doi: 10.1051/0004-6361:200810459.
- A. Poglitsch, C. Waelkens, N. Geis, H. Feuchtgruber, B. Vandenbussche, L. Rodriguez, O. Krause, E. Renotte, C. van Hoof, P. Saraceno, J. Cepa, F. Kerschbaum, P. Agnèse, B. Ali, B. Altieri, P. Andreani, J.-L. Augueres, Z. Balog, L. Barl, O. H. Bauer, N. Belbachir, M. Benedettini, N. Billot, O. Boulade, H. Bischof, J. Blommaert, E. Callut, C. Cara, R. Cerulli, D. Cesarsky, A. Contursi, Y. Creten, W. De Meester, V. Doublier, E. Doumayrou, L. Duband, K. Exter, R. Genzel, J.-M. Gillis, U. Grözinger, T. Henning, J. Herreros, R. Huygen, M. Inguscio, G. Jakob, C. Jamar, C. Jean, J. de Jong, R. Katterloher, C. Kiss, U. Klaas, D. Lemke, D. Lutz, S. Madden, B. Marquet, J. Martignac, A. Mazy, P. Merken, F. Montfort, L. Morbidelli, T. Müller, M. Nielbock, K. Okumura, R. Orfei, R. Ottensamer, S. Pezzuto, P. Popesso, J. Putzeys, S. Regibo, V. Reveret, P. Royer, M. Sauvage, J. Schreiber, J. Stegmaier, D. Schmitt, J. Schubert, E. Sturm, M. Thiel, G. Tofani, R. Vavrek, M. Wetzstein, E. Wieprecht, and E. Wieszorrek. The Photodetector Array Camera and Spectrometer (PACS) on the Herschel Space Observatory. *A&A*, 518:L2, July 2010. doi: 10.1051/0004-6361/201014535.
-

-
- G. L. Pilbratt, J. R. Riedinger, T. Passvogel, G. Crone, D. Doyle, U. Gageur, A. M. Heras, C. Jewell, L. Metcalfe, S. Ott, and M. Schmidt. Herschel Space Observatory. An ESA facility for far-infrared and submillimetre astronomy. *A&A*, 518:L1, July 2010. doi: 10.1051/0004-6361/201014759.
- S. Ott. The Herschel Data Processing System - HIPE and Pipelines - Up and Running Since the Start of the Mission. In Y. Mizumoto, K.-I. Morita, and M. Ohishi, editors, *Astronomical Data Analysis Software and Systems XIX*, volume 434 of *Astronomical Society of the Pacific Conference Series*, page 139, December 2010.
- I. Smirnova-Pinchukova, B. Husemann, G. Busch, P. Appleton, M. Bethermin, F. Combes, S. Croom, T. A. Davis, C. Fischer, M. Gaspari, B. Groves, R. Klein, C. P. O’Dea, M. Pérez-Torres, J. Scharwächter, M. Singha, G. R. Tremblay, and T. Urrutia. The Close AGN Reference Survey (CARS). Discovery of a global [C II] 158 μm line excess in AGN HE 1353-1917. *A&A*, 626:L3, Jun 2019. doi: 10.1051/0004-6361/201935577.
- A. S. Fruchter and R. N. Hook. Drizzle: A method for the linear reconstruction of undersampled images. *Publications of the Astronomical Society of the Pacific*, 114(792):144–152, feb 2002. doi: 10.1086/338393. URL <https://doi.org/10.1086%2F338393>.
- S. D. Lord. NASA Technical Memorandum 103957. Technical report, NASA, 1992. URL <https://atran.arc.nasa.gov/cgi-bin/atran/atran.cgi>.
- E. L. Wright, P. R. M. Eisenhardt, A. K. Mainzer, M. E. Ressler, R. M. Cutri, T. Jarrett, J. D. Kirkpatrick, D. Padgett, R. S. McMillan, M. Skrutskie, S. A. Stanford, M. Cohen, R. G. Walker, J. C. Mather, D. Leisawitz, T. N. Gautier, III, I. McLean, D. Benford, C. J. Lonsdale, A. Blain, B. Mendez, W. R. Irace, V. Duval, F. Liu, D. Royer, I. Heinrichsen, J. Howard, M. Shannon, M. Kendall, A. L. Walsh, M. Larsen, J. G. Cardon, S. Schick, M. Schwalm, M. Abid, B. Fabinsky, L. Naes, and C.-W. Tsai. The Wide-field Infrared Survey Explorer (WISE): Mission Description and Initial On-orbit Performance. *AJ*, 140:1868-1881, December 2010. doi: 10.1088/0004-6256/140/6/1868.
- E. Bertin and S. Arnouts. SExtractor: Software for source extraction. *A&AS*, 117:393–404, June 1996. doi: 10.1051/aas:1996164.
- D. Lang. unWISE: Unblurred Coadds of the WISE Imaging. *AJ*, 147:108, May 2014. doi: 10.1088/0004-6256/147/5/108.
- H. Murakami, H. Baba, P. Barthel, D. L. Clements, M. Cohen, Y. Doi, K. Enya, E. Figueredo, N. Fujishiro, H. Fujiwara, M. Fujiwara, P. Garcia-Lario, T. Goto, S. Hasegawa, Y. Hibi, T. Hirao, N. Hiromoto, S. S. Hong, K. Imai, M. Ishigaki, M. Ishiguro, D. Ishihara, Y. Ita, W.-S. Jeong, K. S. Jeong, H. Kaneda, H. Kataza, M. Kawada, T. Kawai, A. Kawamura, M. F. Kessler, D. Kester, T. Kii, D. C. Kim, W. Kim, H. Kobayashi, B. C. Koo, S. M. Kwon, H. M. Lee, R. Lorente, S. Makiuti, H. Matsuhara, T. Matsumoto, H. Matsuo, S. Matsuura, T. G. Müller, N. Murakami, H. Nagata, T. Nakagawa, T. Naoi, M. Narita, M. Noda, S. H. Oh, A. Ohnishi, Y. Ohyama, Y. Okada, H. Okuda, S. Oliver, T. Onaka, T. Ootsubo, S. Oyabu, S. Pak, Y.-S. Park, C. P. Pearson, M. Rowan-Robinson, T. Saito, I. Sakon, A. Salama, S. Sato, R. S. Savage, S. Serjeant, H. Shibai, M. Shirahata, J. Sohn, T. Suzuki, T. Takagi, H. Takahashi, T. TanabÉ, T. T. Takeuchi, S. Takita, M. Thomson, K. Uemizu, M. Ueno, F. Usui, E. Verdugo, T. Wada, L. Wang, T. Watabe, H. Watarai, G. J. White, I. Yamamura, C. Yamauchi, and A. Yasuda. The Infrared Astronomical Mission AKARI*. *PASJ*, 59:S369–S376, October 2007. doi: 10.1093/pasj/59.sp2.S369.
- M. Kawada, H. Baba, P. D. Barthel, D. Clements, M. Cohen, Y. Doi, E. Figueredo, M. Fujiwara, T. Goto, S. Hasegawa, Y. Hibi, T. Hirao, N. Hiromoto, W.-S. Jeong, H. Kaneda, T. Kawai, A. Kawamura, D. Kester, T. Kii, H. Kobayashi, S. M. Kwon, H. M. Lee, S. Makiuti, H. Matsuo, S. Matsuura, T. G. Müller, N. Murakami, H. Nagata, T. Nakagawa, M. Narita, M. Noda, S. H. Oh, Y. Okada, H. Okuda, S. Oliver, T. Ootsubo, S. Pak, Y.-S. Park, C. P. Pearson, M. Rowan-Robinson, T. Saito, A. Salama, S. Sato, R. S. Savage, S. Serjeant, H. Shibai, M. Shirahata, J. Sohn, T. Suzuki, T. Takagi, H. Takahashi, M. Thomson, F. Usui, E. Verdugo, T. Watabe, G. J. White, L. Wang, I. Yamamura, C. Yamauchi, and A. Yasuda. The Far-Infrared Surveyor (FIS) for AKARI. *PASJ*, 59:S389, October 2007. doi: 10.1093/pasj/59.sp2.S389.
- Y. Doi, S. Takita, T. Ootsubo, K. Arimatsu, M. Tanaka, Y. Kitamura, M. Kawada, S. Matsuura, T. Nakagawa, T. Morishima, M. Hattori, S. Komugi, G. J. White, N. Ikeda, D. Kato, Y. Chinone, M. Etxaluze, and E. F. Cypriano. The AKARI far-infrared all-sky survey maps. *PASJ*, 67:50, June 2015. doi: 10.1093/pasj/psv022.
-

-
- S. Takita, Y. Doi, T. Ootsubo, K. Arimatsu, N. Ikeda, M. Kawada, Y. Kitamura, S. Matsuura, T. Nakagawa, M. Hattori, T. Morishima, M. Tanaka, and S. Komugi. Calibration of the AKARI far-infrared all-sky survey maps. *PASJ*, 67:51, June 2015. doi: 10.1093/pasj/psv033.
- B. T. Draine and A. Li. Infrared Emission from Interstellar Dust. IV. The Silicate-Graphite-PAH Model in the Post-Spitzer Era. *ApJ*, 657:810–837, March 2007. doi: 10.1086/511055.
- J. S. Mathis, P. G. Mezger, and N. Panagia. Interstellar radiation field and dust temperatures in the diffuse interstellar matter and in giant molecular clouds. *A&A*, 128:212–229, November 1983.
- H. J. Habing. The interstellar radiation density between 912 Å and 2400 Å. *Bull. Astron. Inst. Netherlands*, 19:421, January 1968.
- B. T. Draine, D. A. Dale, G. Bendo, K. D. Gordon, J. D. T. Smith, L. Armus, C. W. Engelbracht, G. Helou, R. C. Kennicutt, Jr., A. Li, H. Roussel, F. Walter, D. Calzetti, J. Moustakas, E. J. Murphy, G. H. Rieke, C. Bot, D. J. Hollenbach, K. Sheth, and H. I. Teplitz. Dust Masses, PAH Abundances, and Starlight Intensities in the SINGS Galaxy Sample. *ApJ*, 663:866–894, July 2007. doi: 10.1086/518306.
- Frédéric Galliano. A dust spectral energy distribution model with hierarchical Bayesian inference – I. Formalism and benchmarking. *Monthly Notices of the Royal Astronomical Society*, 476(2):1445–1469, 01 2018. ISSN 0035-8711. doi: 10.1093/mnras/sty189. URL <https://doi.org/10.1093/mnras/sty189>.
- U. Lisenfeld and A. Ferrara. Dust-to-Gas Ratio and Metal Abundance in Dwarf Galaxies. *ApJ*, 496:145–154, March 1998. doi: 10.1086/305354.
- H. Hirashita, Y. Y. Tajiri, and H. Kamaya. Dust-to-gas ratio and star formation history of blue compact dwarf galaxies. *A&A*, 388:439–445, June 2002. doi: 10.1051/0004-6361:20020605.
- A. James, L. Dunne, S. Eales, and M. G. Edmunds. SCUBA observations of galaxies with metallicity measurements: a new method for determining the relation between submillimetre luminosity and dust mass. *MNRAS*, 335:753–761, September 2002. doi: 10.1046/j.1365-8711.2002.05660.x.
- L. Hunt, S. Bianchi, and R. Maiolino. The optical-to-radio spectral energy distributions of low-metallicity blue compact dwarf galaxies. *A&A*, 434:849–866, May 2005. doi: 10.1051/0004-6361:20042157.
- C. W. Engelbracht, G. H. Rieke, K. D. Gordon, J.-D. T. Smith, M. W. Werner, J. Moustakas, C. N. A. Willmer, and L. Vanzì. Metallicity Effects on Dust Properties in Starbursting Galaxies. *ApJ*, 678:804–827, May 2008. doi: 10.1086/529513.
- F. Galliano, E. Dwek, and P. Chianal. Stellar Evolutionary Effects on the Abundances of Polycyclic Aromatic Hydrocarbons and Supernova-Condensed Dust in Galaxies. *ApJ*, 672:214–243, January 2008. doi: 10.1086/523621.
- J. C. Muñoz-Mateos, A. Gil de Paz, S. Boissier, J. Zamorano, D. A. Dale, P. G. Pérez-González, J. Gallego, B. F. Madore, G. Bendo, M. D. Thornley, B. T. Draine, A. Boselli, V. Buat, D. Calzetti, J. Moustakas, and R. C. Kennicutt, Jr. Radial Distribution of Stars, Gas, and Dust in Sings Galaxies. II. Derived Dust Properties. *ApJ*, 701:1965–1991, August 2009. doi: 10.1088/0004-637X/701/2/1965.
- G. J. Bendo, C. D. Wilson, B. E. Warren, E. Brinks, H. M. Butner, P. Chianal, D. L. Clements, S. Courteau, J. Irwin, F. P. Israel, J. H. Knapen, J. Leech, H. E. Matthews, S. Mühle, G. Petitpas, S. Serjeant, B. K. Tan, R. P. J. Tilanus, A. Usero, M. Vaccari, P. van der Werf, C. Vlahakis, T. Wiegert, and M. Zhu. The JCMT Nearby Galaxies Legacy Survey - III. Comparisons of cold dust, polycyclic aromatic hydrocarbons, molecular gas and atomic gas in NGC 2403. *MNRAS*, 402:1409–1425, March 2010. doi: 10.1111/j.1365-2966.2009.16043.x.
- M. Galametz, S. C. Madden, F. Galliano, S. Hony, G. J. Bendo, and M. Sauvage. Probing the dust properties of galaxies up to submillimetre wavelengths. II. Dust-to-gas mass ratio trends with metallicity and the submm excess in dwarf galaxies. *A&A*, 532:A56, August 2011. doi: 10.1051/0004-6361/201014904.
-

-
- L. Magrini, S. Bianchi, E. Corbelli, L. Cortese, L. Hunt, M. Smith, C. Vlahakis, J. Davies, G. J. Bendo, M. Baes, A. Boselli, M. Clemens, V. Casasola, I. De Looze, J. Fritz, C. Giovanardi, M. Grossi, T. Hughes, S. Madden, C. Pappalardo, M. Pohlen, S. di Serego Alighieri, and J. Verstappen. The Herschel Virgo Cluster Survey. IX. Dust-to-gas mass ratio and metallicity gradients in four Virgo spiral galaxies. *A&A*, 535:A13, November 2011. doi: 10.1051/0004-6361/201116872.
- K. M. Sandstrom, A. K. Leroy, F. Walter, A. D. Bolatto, K. V. Croxall, B. T. Draine, C. D. Wilson, M. Wolfire, D. Calzetti, R. C. Kennicutt, G. Aniano, J. Donovan Meyer, A. Usero, F. Bigiel, E. Brinks, W. J. G. de Blok, A. Crocker, D. Dale, C. W. Engelbracht, M. Galametz, B. Groves, L. K. Hunt, J. Koda, K. Kreckel, H. Linz, S. Meidt, E. Pellegrini, H.-W. Rix, H. Roussel, E. Schinnerer, A. Schrubba, K.-F. Schuster, R. Skibba, T. van der Laan, P. Appleton, L. Armus, B. Brandl, K. Gordon, J. Hinz, O. Krause, E. Montiel, M. Sauvage, A. Schmiedeke, J. D. T. Smith, and L. Vigroux. The CO-to-H₂ Conversion Factor and Dust-to-gas Ratio on Kiloparsec Scales in Nearby Galaxies. *ApJ*, 777:5, November 2013. doi: 10.1088/0004-637X/777/1/5.
- A. Rémy-Ruyer, S. C. Madden, F. Galliano, M. Galametz, T. T. Takeuchi, R. S. Asano, S. Zhukovska, V. Lebouteiller, D. Cormier, A. Jones, M. Bocchio, M. Baes, G. J. Bendo, M. Boquien, A. Boselli, I. DeLooze, V. Doublier-Pritchard, T. Hughes, O. Ł. Karczewski, and L. Spinoglio. Gas-to-dust mass ratios in local galaxies over a 2 dex metallicity range. *A&A*, 563:A31, March 2014. doi: 10.1051/0004-6361/201322803.
- J. Roman-Duval, K. D. Gordon, M. Meixner, C. Bot, A. Bolatto, A. Hughes, T. Wong, B. Babler, J.-P. Bernard, G. C. Clayton, Y. Fukui, M. Galametz, F. Galliano, S. Glover, S. Hony, F. Israel, K. Jameson, V. Lebouteiller, M.-Y. Lee, A. Li, S. Madden, K. Misselt, E. Montiel, K. Okumura, T. Onishi, P. Panuzzo, W. Reach, A. Remy-Ruyer, T. Robitaille, M. Rubio, M. Sauvage, J. Seale, M. Sewilo, L. Staveley-Smith, and S. Zhukovska. Dust and Gas in the Magellanic Clouds from the HERITAGE Herschel Key Project. II. Gas-to-dust Ratio Variations across Interstellar Medium Phases. *ApJ*, 797:86, December 2014. doi: 10.1088/0004-637X/797/2/86.
- L. Cortese, K. Bekki, A. Boselli, B. Catinella, L. Ciesla, T. M. Hughes, M. Baes, G. J. Bendo, M. Boquien, I. de Looze, M. W. L. Smith, L. Spinoglio, and S. Viaene. The selective effect of environment on the atomic and molecular gas-to-dust ratio of nearby galaxies in the Herschel Reference Survey. *MNRAS*, 459:3574–3584, July 2016. doi: 10.1093/mnras/stw801.
- L. Kahre, R. A. Walterbos, H. Kim, D. Thilker, D. Calzetti, J. C. Lee, E. Sabbi, L. Ubeda, A. Aloisi, M. Cignoni, D. O. Cook, D. A. Dale, B. G. Elmegreen, D. M. Elmegreen, M. Fumagalli, J. S. Gallagher, III, D. A. Gouliermis, K. Grasha, E. K. Grebel, D. A. Hunter, E. Sacchi, L. J. Smith, M. Tosi, A. Adamo, J. E. Andrews, G. Ashworth, S. N. Bright, T. M. Brown, R. Chandar, C. Christian, S. E. de Mink, C. Dobbs, A. S. Evans, A. Herrero, K. E. Johnson, R. C. Kennicutt, M. R. Krumholz, M. Messa, P. Nair, A. Nota, A. Pellerin, J. E. Ryon, D. Schaerer, F. Shabani, S. D. Van Dyk, B. C. Whitmore, and A. Wofford. Extinction Maps and Dust-to-gas Ratios in Nearby Galaxies with LEGUS. *ApJ*, 855:133, March 2018. doi: 10.3847/1538-4357/aab101.
- F. Galliano, S. C. Madden, A. P. Jones, C. D. Wilson, J.-P. Bernard, and F. Le Peintre. ISM properties in low-metallicity environments. II. The dust spectral energy distribution of NGC 1569. *A&A*, 407:159–176, August 2003. doi: 10.1051/0004-6361:20030814.
- F. Galliano, S. C. Madden, A. P. Jones, C. D. Wilson, and J.-P. Bernard. ISM properties in low-metallicity environments. III. The spectral energy distributions of II Zw 40, He 2-10 and NGC 1140. *A&A*, 434:867–885, May 2005. doi: 10.1051/0004-6361:20042369.
- F. Galliano, S. Hony, J.-P. Bernard, C. Bot, S. C. Madden, J. Roman-Duval, M. Galametz, A. Li, M. Meixner, C. W. Engelbracht, V. Lebouteiller, K. Misselt, E. Montiel, P. Panuzzo, W. T. Reach, and R. Skibba. Non-standard grain properties, dark gas reservoir, and extended submillimeter excess, probed by Herschel in the Large Magellanic Cloud. *A&A*, 536:A88, December 2011. doi: 10.1051/0004-6361/201117952.
- P. M. Solomon and P. A. Vanden Bout. Molecular Gas at High Redshift. *ARA&A*, 43:677–725, September 2005. doi: 10.1146/annurev.astro.43.051804.102221.
-

-
- U. Lisenfeld, D. Espada, L. Verdes-Montenegro, N. Kuno, S. Leon, J. Sabater, N. Sato, J. Sulentic, S. Verley, and M. S. Yun. The AMIGA sample of isolated galaxies. IX. Molecular gas properties. *A&A*, 534:A102, October 2011. doi: 10.1051/0004-6361/201117056.
- D. V. Stark, S. J. Kannappan, L. H. Wei, A. J. Baker, A. K. Leroy, K. D. Eckert, and S. N. Vogel. The Fueling Diagram: Linking Galaxy Molecular-to-atomic Gas Ratios to Interactions and Accretion. *ApJ*, 769:82, May 2013. doi: 10.1088/0004-637X/769/1/82.
- J. S. Young, S. Xie, L. Tacconi, P. Knezek, P. Viscuso, L. Tacconi-Garman, N. Scoville, S. Schneider, F. P. Schloerb, S. Lord, A. Lesser, J. Kenney, Y.-L. Huang, N. Devereux, M. Claussen, J. Case, J. Carpenter, M. Berry, and L. Allen. The FCRAO Extragalactic CO Survey. I. The Data. *ApJS*, 98:219, May 1995. doi: 10.1086/192159.
- T. A. Davis, K. Alatalo, M. Bureau, M. Cappellari, N. Scott, L. M. Young, L. Blitz, A. Crocker, E. Bayet, M. Bois, F. Bournaud, R. L. Davies, P. T. de Zeeuw, P.-A. Duc, E. Emsellem, S. Khochfar, D. Krajnović, H. Kuntschner, P.-Y. Lablanche, R. M. McDermid, R. Morganti, T. Naab, T. Oosterloo, M. Sarzi, P. Serra, and A.-M. Weijmans. The ATLAS^{3D} Project - XIV. The extent and kinematics of the molecular gas in early-type galaxies. *MNRAS*, 429: 534–555, February 2013. doi: 10.1093/mnras/sts353.
- E. P. Hubble. Extragalactic nebulae. *ApJ*, 64, December 1926. doi: 10.1086/143018.
- A. D. Bolatto, M. Wolfire, and A. K. Leroy. The CO-to-H₂ Conversion Factor. *ARA&A*, 51:207–268, August 2013. doi: 10.1146/annurev-astro-082812-140944.
- G. E. Magdis, E. Daddi, D. Elbaz, M. Sargent, M. Dickinson, H. Dannerbauer, H. Aussel, F. Walter, H. S. Hwang, V. Charmandaris, J. Hodge, D. Riechers, D. Rigopoulou, C. Carilli, M. Pannella, J. Mullaney, R. Leiton, and D. Scott. GOODS-Herschel: Gas-to-dust Mass Ratios and CO-to-H₂ Conversion Factors in Normal and Starbursting Galaxies at High-*z*. *ApJ*, 740:L15, October 2011. doi: 10.1088/2041-8205/740/1/L15.
- R. Genzel, L. J. Tacconi, F. Combes, A. Bolatto, R. Neri, A. Sternberg, M. C. Cooper, N. Bouché, F. Bournaud, A. Burkert, J. Comerford, P. Cox, M. Davis, N. M. Förster Schreiber, S. Garcia-Burillo, J. Gracia-Carpio, D. Lutz, T. Naab, S. Newman, A. Saintonge, K. Shapiro, A. Shapley, and B. Weiner. The Metallicity Dependence of the CO-H₂ Conversion Factor in $z \geq 1$ Star-forming Galaxies. *ApJ*, 746:69, February 2012. doi: 10.1088/0004-637X/746/1/69.
- D. Narayanan, M. R. Krumholz, E. C. Ostriker, and L. Hernquist. A general model for the CO-H₂ conversion factor in galaxies with applications to the star formation law. *MNRAS*, 421:3127–3146, April 2012. doi: 10.1111/j.1365-2966.2012.20536.x.
- A. Schruba, A. K. Leroy, F. Walter, F. Bigiel, E. Brinks, W. J. G. de Blok, C. Kramer, E. Rosolowsky, K. Sandstrom, K. Schuster, A. Usero, A. Weiss, and H. Wiesemeyer. Low CO Luminosities in Dwarf Galaxies. *AJ*, 143:138, June 2012. doi: 10.1088/0004-6256/143/6/138.
- L. K. Hunt, S. García-Burillo, V. Casasola, P. Caselli, F. Combes, C. Henkel, A. Lundgren, R. Maiolino, K. M. Menten, L. Testi, and A. Weiss. Molecular depletion times and the CO-to-H₂ conversion factor in metal-poor galaxies. *A&A*, 583:A114, November 2015. doi: 10.1051/0004-6361/201526553.
- R. Amorín, C. Muñoz-Tuñón, J. A. L. Aguerra, and P. Planesas. Molecular gas in low-metallicity starburst galaxies: Scaling relations and the CO-to-H₂ conversion factor. *A&A*, 588:A23, April 2016. doi: 10.1051/0004-6361/201526397.
- G. Accurso, A. Saintonge, B. Catinella, L. Cortese, R. Davé, S. H. Dunsheath, R. Genzel, J. Gracia-Carpio, T. M. Heckman, Jimmy, C. Kramer, C. Li, K. Lutz, D. Schiminovich, K. Schuster, A. Sternberg, E. Sturm, L. J. Tacconi, K. V. Tran, and J. Wang. Deriving a multivariate α_{CO} conversion function using the [C II]/CO (1-0) ratio and its application to molecular gas scaling relations. *MNRAS*, 470:4750–4766, October 2017. doi: 10.1093/mnras/stx1556.
-

-
- Andreas Schruba, Adam K. Leroy, J. M. Diederik Kruijssen, Frank Bigiel, Alberto D. Bolatto, W. J. G. de Blok, Linda Tacconi, Ewine F. van Dishoeck, and Fabian Walter. Physical properties of molecular clouds at 2 pc resolution in the low-metallicity dwarf galaxy NGC 6822 and the milky way. *The Astrophysical Journal*, 835(2):278, feb 2017. doi: 10.3847/1538-4357/835/2/278. URL <https://doi.org/10.3847/1538-4357/835/2/278>.
- R. C. Kennicutt and N. J. Evans. Star Formation in the Milky Way and Nearby Galaxies. *ARA&A*, 50:531–608, September 2012. doi: 10.1146/annurev-astro-081811-125610.
- C.-N. Hao, R. C. Kennicutt, B. D. Johnson, D. Calzetti, D. A. Dale, and J. Moustakas. Dust-corrected Star Formation Rates of Galaxies. II. Combinations of Ultraviolet and Infrared Tracers. *ApJ*, 741:124, November 2011. doi: 10.1088/0004-637X/741/2/124.
- E. J. Murphy, J. J. Condon, E. Schinnerer, R. C. Kennicutt, D. Calzetti, L. Armus, G. Helou, J. L. Turner, G. Aniano, P. Beirão, A. D. Bolatto, B. R. Brandl, K. V. Croxall, D. A. Dale, J. L. Donovan Meyer, B. T. Draine, C. Engelbracht, L. K. Hunt, C.-N. Hao, J. Koda, H. Roussel, R. Skibba, and J.-D. T. Smith. Calibrating Extinction-free Star Formation Rate Diagnostics with 33 GHz Free-free Emission in NGC 6946. *ApJ*, 737:67, August 2011. doi: 10.1088/0004-637X/737/2/67.
- P. Kroupa and C. Weidner. Galactic-Field Initial Mass Functions of Massive Stars. *ApJ*, 598:1076–1078, December 2003. doi: 10.1086/379105.
- E. E. Salpeter. The Luminosity Function and Stellar Evolution. *ApJ*, 121:161, January 1955. doi: 10.1086/145971.
- G. Chabrier. Galactic Stellar and Substellar Initial Mass Function. *PASP*, 115:763–795, July 2003. doi: 10.1086/376392.
- G. H. Rieke, A. Alonso-Herrero, B. J. Weiner, P. G. Pérez-González, M. Blaylock, J. L. Donley, and D. Marcillac. Determining Star Formation Rates for Infrared Galaxies. *ApJ*, 692:556–573, February 2009. doi: 10.1088/0004-637X/692/1/556.
- Ilse De Looze, Diane Cormier, Vianney Lebouteiller, Suzanne Madden, Maarten Baes, George J. Bendo, Médéric Boquien, Alessandro Boselli, David L. Clements, Luca Cortese, Asantha Cooray, Maud Galametz, Frédéric Galliano, Javier Graciá-Carpio, Kate Isaak, Oskar Ł. Karczewski, Tara J. Parkin, Eric W. Pellegrini, Aurélie Rémy-Ruyer, Luigi Spinoglio, Matthew W. L. Smith, and Eckhard Sturm. The applicability of far-infrared fine-structure lines as star formation rate tracers over wide ranges of metallicities and galaxy types. *A&A*, 568:A62, Aug 2014. doi: 10.1051/0004-6361/201322489.
- P. N. Appleton, P. Guillard, F. Boulanger, M. E. Cluver, P. Ogle, E. Falgarone, G. Pineau des Forêts, E. O’Sullivan, P. A. Duc, S. Gallagher, Y. Gao, T. Jarrett, I. Konstantopoulos, U. Lisenfeld, S. Lord, N. Lu, B. W. Peterson, C. Struck, E. Sturm, R. Tuffs, I. Valchanov, P. van der Werf, and K. C. Xu. Shock-enhanced C⁺ Emission and the Detection of H₂O from the Stephan’s Quintet Group-wide Shock Using Herschel. *ApJ*, 777(1):66, Nov 2013. doi: 10.1088/0004-637X/777/1/66.
- P. N. Appleton, T. Diaz-Santos, D. Fadda, P. Ogle, A. Togi, L. Lanz, K. Alatalo, C. Fischer, J. Rich, and P. Guillard. Jet-related Excitation of the [C II] Emission in the Active Galaxy NGC 4258 with SOFIA. *ApJ*, 869(1):61, Dec 2018. doi: 10.3847/1538-4357/aaed2a.
- A. Saintonge, G. Kauffmann, C. Kramer, L. J. Tacconi, C. Buchbender, B. Catinella, S. Fabello, J. Graciá-Carpio, J. Wang, L. Cortese, J. Fu, R. Genzel, R. Giovanelli, Q. Guo, M. P. Haynes, T. M. Heckman, M. R. Krumholz, J. Lemonias, C. Li, S. Moran, N. Rodriguez-Fernandez, D. Schiminovich, K. Schuster, and A. Sievers. COLD GASS, an IRAM legacy survey of molecular gas in massive galaxies - I. Relations between H₂, H I, stellar content and structural properties. *MNRAS*, 415:32–60, July 2011a. doi: 10.1111/j.1365-2966.2011.18677.x.
- A. Saintonge, G. Kauffmann, J. Wang, C. Kramer, L. J. Tacconi, C. Buchbender, B. Catinella, J. Graciá-Carpio, L. Cortese, S. Fabello, J. Fu, R. Genzel, R. Giovanelli, Q. Guo, M. P. Haynes, T. M. Heckman, M. R. Krumholz, J. Lemonias, C. Li, S. Moran, N. Rodriguez-Fernandez, D. Schiminovich, K. Schuster, and A. Sievers. COLD GASS,
-

-
- an IRAM legacy survey of molecular gas in massive galaxies - II. The non-universality of the molecular gas depletion time-scale. *MNRAS*, 415:61–76, July 2011b. doi: 10.1111/j.1365-2966.2011.18823.x.
- A. Saintonge, L. J. Tacconi, S. Fabello, J. Wang, B. Catinella, R. Genzel, J. Graciá-Carpio, C. Kramer, S. Moran, T. M. Heckman, D. Schiminovich, K. Schuster, and S. Wuyts. The Impact of Interactions, Bars, Bulges, and Active Galactic Nuclei on Star Formation Efficiency in Local Massive Galaxies. *ApJ*, 758:73, October 2012. doi: 10.1088/0004-637X/758/2/73.
- B. Catinella, D. Schiminovich, G. Kauffmann, S. Fabello, C. Hummels, J. Lemonias, S. M. Moran, R. Wu, A. Cooper, and J. Wang. The GALEX Arcibo SDSS Survey. VI. Second data release and updated gas fraction scaling relations. *A&A*, 544:A65, August 2012. doi: 10.1051/0004-6361/201219261.
- M. R. Krumholz, A. Dekel, and C. F. McKee. A Universal, Local Star Formation Law in Galactic Clouds, nearby Galaxies, High-redshift Disks, and Starbursts. *ApJ*, 745:69, January 2012. doi: 10.1088/0004-637X/745/1/69.
- R. Herrera-Camus, E. Sturm, J. Graciá-Carpio, D. Lutz, A. Contursi, S. Veilleux, J. Fischer, E. González-Alfonso, A. Poglitsch, L. Tacconi, R. Genzel, R. Maiolino, A. Sternberg, R. Davies, and A. Verma. SHINING, A Survey of Far-infrared Lines in Nearby Galaxies. I. Survey Description, Observational Trends, and Line Diagnostics. *ApJ*, 861: 94, July 2018a. doi: 10.3847/1538-4357/aac0f6.
- R. Herrera-Camus, E. Sturm, J. Graciá-Carpio, D. Lutz, A. Contursi, S. Veilleux, J. Fischer, E. González-Alfonso, A. Poglitsch, L. Tacconi, R. Genzel, R. Maiolino, A. Sternberg, R. Davies, and A. Verma. SHINING, A Survey of Far-infrared Lines in Nearby Galaxies. II. Line-deficit Models, AGN Impact, [C II]-SFR Scaling Relations, and Mass-Metallicity Relation in (U)LIRGs. *ApJ*, 861:95, July 2018b. doi: 10.3847/1538-4357/aac0f9.
- Y. Zhao, L. Yan, and C.-W. Tsai. Properties of Interstellar Medium In Infrared-bright QSOs Probed by [O I] 63 um and [C II] 158 um Emission Lines. *ApJ*, 824:146, June 2016. doi: 10.3847/0004-637X/824/2/146.
- M. J. Kaufman, M. G. Wolfire, D. J. Hollenbach, and M. L. Luhman. Far-Infrared and Submillimeter Emission from Galactic and Extragalactic Photodissociation Regions. *ApJ*, 527:795–813, December 1999. doi: 10.1086/308102.
- M. J. Kaufman, M. G. Wolfire, and D. J. Hollenbach. [Si II], [Fe II], [C II], and H₂ Emission from Massive Star-forming Regions. *ApJ*, 644:283–299, June 2006. doi: 10.1086/503596.
- M. W. Pound and M. G. Wolfire. The Photo Dissociation Region Toolbox. In R. W. Argyle, P. S. Bunclark, and J. R. Lewis, editors, *Astronomical Data Analysis Software and Systems XVII*, volume 394 of *Astronomical Society of the Pacific Conference Series*, page 654, August 2008.
- J. V. Wall. Practical Statistics for Astronomers - II. Correlation, Data-modelling and Sample Comparison. *QJRAS*, 37: 519, December 1996.
- G. Helou, I. R. Khan, L. Malek, and L. Boehmer. IRAS observations of galaxies in the Virgo cluster area. *ApJS*, 68: 151–172, October 1988. doi: 10.1086/191285.
- J. Graciá-Carpio, E. Sturm, S. Hailey-Dunsheath, J. Fischer, A. Contursi, A. Poglitsch, R. Genzel, E. González-Alfonso, A. Sternberg, A. Verma, N. Christopher, R. Davies, H. Feuchtgruber, J. A. de Jong, D. Lutz, and L. J. Tacconi. Far-infrared Line Deficits in Galaxies with Extreme $L_{\text{FIR}}/M_{\text{H}_2}$ Ratios. *ApJ*, 728:L7, February 2011. doi: 10.1088/2041-8205/728/1/L7.
- A. Contursi, A. J. Baker, S. Berta, B. Magnelli, D. Lutz, J. Fischer, A. Verma, M. Nielbock, J. Gracia Carpio, S. Veilleux, E. Sturm, R. Davies, R. Genzel, S. Hailey-Dunsheath, R. Herrera-Camus, A. Janssen, A. Poglitsch, A. Sternberg, and L. J. Tacconi. Interstellar medium conditions in z 0.2 Lyman-break analogs. *A&A*, 606:A86, October 2017. doi: 10.1051/0004-6361/201730609.
- D. Cormier, S. C. Madden, V. Lebouteiller, S. Hony, S. Aalto, F. Costagliola, A. Hughes, A. Rémy-Ruyer, N. Abel, E. Bayet, F. Bigiel, J. M. Cannon, R. J. Cumming, M. Galametz, F. Galliano, S. Viti, and R. Wu. The molecular gas reservoir of 6 low-metallicity galaxies from the Herschel Dwarf Galaxy Survey. A ground-based follow-up survey of CO(1-0), CO(2-1), and CO(3-2). *A&A*, 564:A121, April 2014. doi: 10.1051/0004-6361/201322096.
-

-
- D. Cormier, S. C. Madden, V. Lebouteiller, N. Abel, S. Hony, F. Galliano, A. Rémy-Ruyer, F. Bigiel, M. Baes, A. Boselli, M. Chevance, A. Cooray, I. De Looze, V. Doublier, M. Galametz, T. Hughes, O. Ł. Karczewski, M.-Y. Lee, N. Lu, and L. Spinoglio. The Herschel Dwarf Galaxy Survey. I. Properties of the low-metallicity ISM from PACS spectroscopy. *A&A*, 578:A53, June 2015. doi: 10.1051/0004-6361/201425207.
- G. E. Magdis, D. Rigopoulou, R. Hopwood, J.-S. Huang, D. Farrah, C. Pearson, A. Alonso-Herrero, J. J. Bock, D. Clements, A. Cooray, M. J. Griffin, S. Oliver, I. Perez Fournon, D. Riechers, B. M. Swinyard, D. Scott, N. Thatte, I. Valtchanov, and M. Vaccari. A Far-infrared Spectroscopic Survey of Intermediate Redshift (Ultra) Luminous Infrared Galaxies. *ApJ*, 796:63, November 2014. doi: 10.1088/0004-637X/796/1/63.
- C. L. Carilli and F. Walter. Cool Gas in High-Redshift Galaxies. *ARA&A*, 51:105–161, August 2013. doi: 10.1146/annurev-astro-082812-140953.
- A. Zanella, E. Daddi, G. Magdis, T. Diaz Santos, D. Cormier, D. Liu, A. Cibinel, R. Gobat, M. Dickinson, M. Sargent, G. Popping, S. C. Madden, M. Bethermin, T. M. Hughes, F. Valentino, W. Rujopakarn, M. Pannella, F. Bournaud, F. Walter, T. Wang, D. Elbaz, and R. T. Coogan. The [C II] emission as a molecular gas mass tracer in galaxies at low and high redshifts. *MNRAS*, 481:1976–1999, December 2018. doi: 10.1093/mnras/sty2394.
- H. Umehata, Y. Matsuda, Y. Tamura, K. Kohno, I. Smail, R. J. Ivison, C. C. Steidel, S. C. Chapman, J. E. Geach, M. Hayes, T. Nagao, Y. Ao, R. Kawabe, M. S. Yun, B. Hatsukade, M. Kubo, Y. Kato, T. Saito, S. Ikarashi, K. Nakanishi, M. Lee, T. Izumi, M. Mori, and M. Ouchi. ALMA Reveals Strong [C II] Emission in a Galaxy Embedded in a Giant Ly α Blob at $z = 3.1$. *ApJ*, 834:L16, January 2017. doi: 10.3847/2041-8213/834/2/L16.
- M. S. Bothwell, J. E. Aguirre, M. Aravena, M. Bethermin, T. G. Bisbas, S. C. Chapman, C. De Breuck, A. H. Gonzalez, T. R. Greve, Y. Hezaveh, J. Ma, M. Malkan, D. P. Marrone, E. J. Murphy, J. S. Spilker, M. Strandet, J. D. Vieira, and A. Weiß. ALMA observations of atomic carbon in $z \sim 4$ dusty star-forming galaxies. *MNRAS*, 466:2825–2841, April 2017. doi: 10.1093/mnras/stw3270.
- C. De Breuck, R. Maiolino, P. Caselli, K. Coppin, S. Hailey-Dunsheath, and T. Nagao. Enhanced [CII] emission in a $z = 4.76$ submillimetre galaxy. *A&A*, 530:L8, June 2011. doi: 10.1051/0004-6361/201116868.
- G. J. Stacey, S. Hailey-Dunsheath, C. Ferkinhoff, T. Nikola, S. C. Parshley, D. J. Benford, J. G. Staguhn, and N. Fiolet. A 158 μm [C II] Line Survey of Galaxies at $z \sim 1-2$: An Indicator of Star Formation in the Early Universe. *ApJ*, 724: 957–974, December 2010. doi: 10.1088/0004-637X/724/2/957.
- D. Cormier, S. C. Madden, S. Hony, A. Contursi, A. Poglitsch, F. Galliano, E. Sturm, V. Doublier, H. Feuchtgruber, M. Galametz, N. Geis, J. de Jong, K. Okumura, P. Panuzzo, and M. Sauvage. The effects of star formation on the low-metallicity ISM: NGC 4214 mapped with Herschel/PACS spectroscopy. *A&A*, 518:L57, July 2010. doi: 10.1051/0004-6361/201014699.
- Suzanne C. Madden and Diane Cormier. Dwarf galaxies: Their low metallicity interstellar medium. *Proceedings of the International Astronomical Union*, 14(S344):240–254, 2018. doi: 10.1017/S1743921318007147.
- Y. Gao and P. M. Solomon. The Star Formation Rate and Dense Molecular Gas in Galaxies. *ApJ*, 606:271–290, May 2004c. doi: 10.1086/382999.
- M. J. Jiménez-Donaire, F. Bigiel, A. K. Leroy, D. Cormier, M. Gallagher, A. Usero, A. Bolatto, D. Colombo, S. García-Burillo, A. Hughes, C. Kramer, M. R. Krumholz, D. S. Meier, E. Murphy, J. Pety, E. Rosolowsky, E. Schinnerer, A. Schrubba, N. Tomičić, and L. Zschaechner. Optical depth estimates and effective critical densities of dense gas tracers in the inner parts of nearby galaxy discs. *MNRAS*, 466:49–62, April 2017. doi: 10.1093/mnras/stw2996.
- S. Juneau, D. T. Narayanan, J. Moustakas, Y. L. Shirley, R. S. Bussmann, R. C. Kennicutt, Jr., and P. A. Vanden Bout. Enhanced Dense Gas Fraction in Ultraluminous Infrared Galaxies. *ApJ*, 707:1217–1232, December 2009. doi: 10.1088/0004-637X/707/2/1217.
- Johannes Puschignig. Dense Gas Toolbox, February 2020. URL <https://doi.org/10.5281/zenodo.3686329>.
-

-
- F. F. S. van der Tak, J. H. Black, F. L. Schöier, D. J. Jansen, and E. F. van Dishoeck. A computer program for fast non-LTE analysis of interstellar line spectra. With diagnostic plots to interpret observed line intensity ratios. *A&A*, 468:627–635, June 2007. doi: 10.1051/0004-6361:20066820.
- A. K. Leroy, A. Usero, A. Schruba, F. Bigiel, J. M. D. Kruijssen, A. Kepley, G. A. Blanc, A. D. Bolatto, D. Cormier, M. Gallagher, A. Hughes, M. J. Jiménez-Donaire, E. Rosolowsky, and E. Schinnerer. Millimeter-wave Line Ratios and Sub-beam Volume Density Distributions. *ApJ*, 835:217, February 2017. doi: 10.3847/1538-4357/835/2/217.
- Matteo Messa, Angela Adamo, Göran Å-stlin, Jens Melinder, Matthew Hayes, Johanna S. Bridge, and John Cannon. Star-forming clumps in the Lyman Alpha Reference Sample of galaxies - I. Photometric analysis and clumpiness. *MNRAS*, 487(3):4238–4260, Aug 2019. doi: 10.1093/mnras/stz1337.
- A. Dekel, R. Sari, and D. Ceverino. Formation of Massive Galaxies at High Redshift: Cold Streams, Clumpy Disks, and Compact Spheroids. *ApJ*, 703:785–801, September 2009. doi: 10.1088/0004-637X/703/1/785.
- Taysun Kimm, Jérémy Blaizot, Thibault Garel, Léo Michel-Dansac, Harley Katz, Joakim Rosdahl, Anne Verhamme, and Martin Haehnelt. Understanding the escape of LyC and Ly α photons from turbulent clouds. *MNRAS*, 486(2): 2215–2237, June 2019. doi: 10.1093/mnras/stz989.
- L. Guaita, J. Melinder, M. Hayes, G. Östlin, J. E. Gonzalez, G. Micheva, A. Adamo, J. M. Mas-Hesse, A. Sandberg, H. Otí-Floranes, D. Schaerer, A. Verhamme, E. Freeland, I. Orlitová, P. Laursen, J. M. Cannon, F. Duval, T. Rivera-Thorsen, E. C. Herenz, D. Kunth, H. Atek, J. Puschnig, P. Gruyters, and S. A. Pardy. The Lyman alpha reference sample. IV. Morphology at low and high redshift. *A&A*, 576:A51, Apr 2015. doi: 10.1051/0004-6361/201425053.
- A. K. Leroy, A. Bolatto, K. Gordon, K. Sandstrom, P. Gratier, E. Rosolowsky, C. W. Engelbracht, N. Mizuno, E. Corbelli, Y. Fukui, and A. Kawamura. The CO-to-H₂ Conversion Factor from Infrared Dust Emission across the Local Group. *ApJ*, 737:12, August 2011. doi: 10.1088/0004-637X/737/1/12.

A Bayesian Joint Posterior Probability Distribution for Draine & Li model parameters

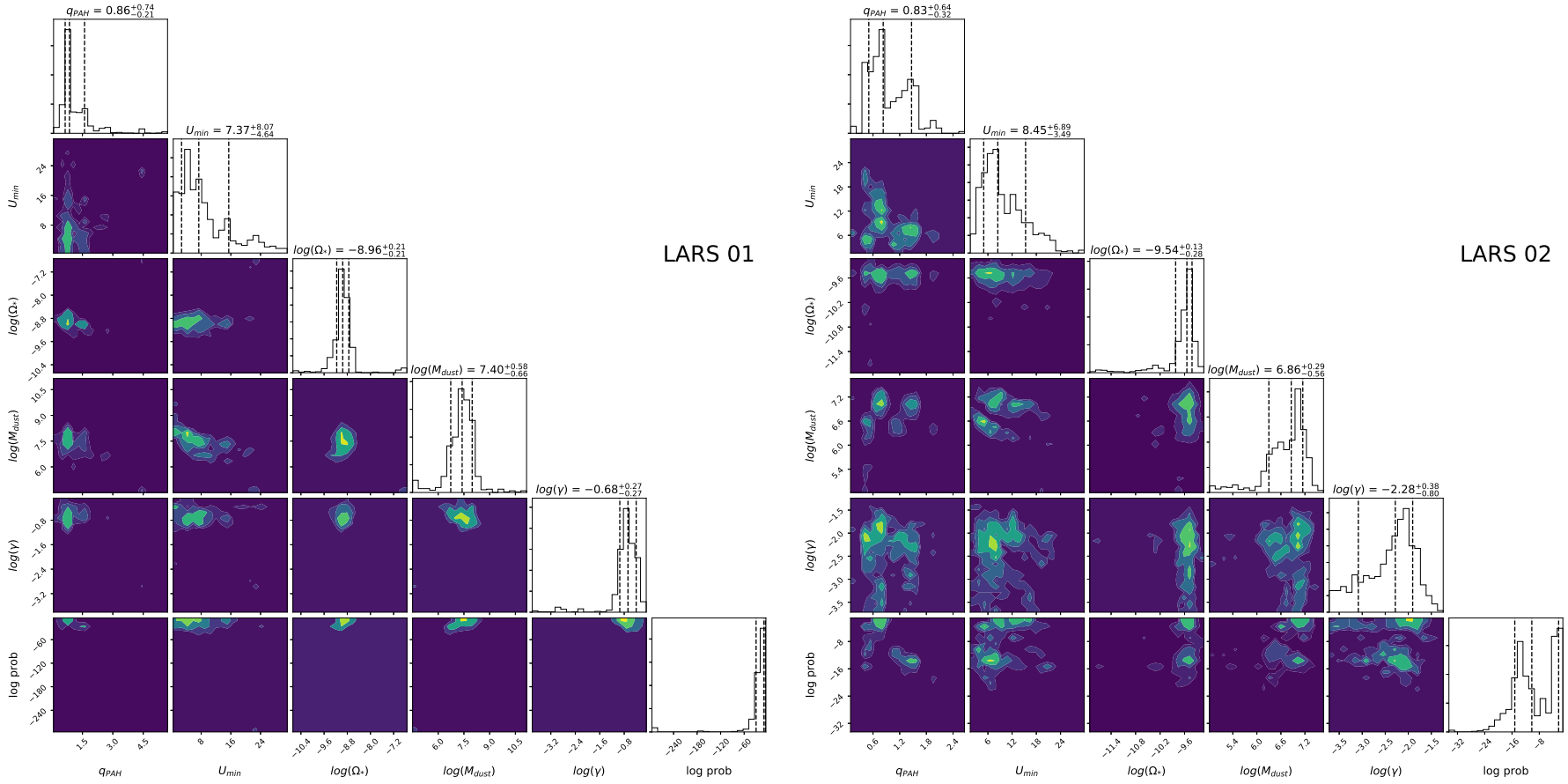
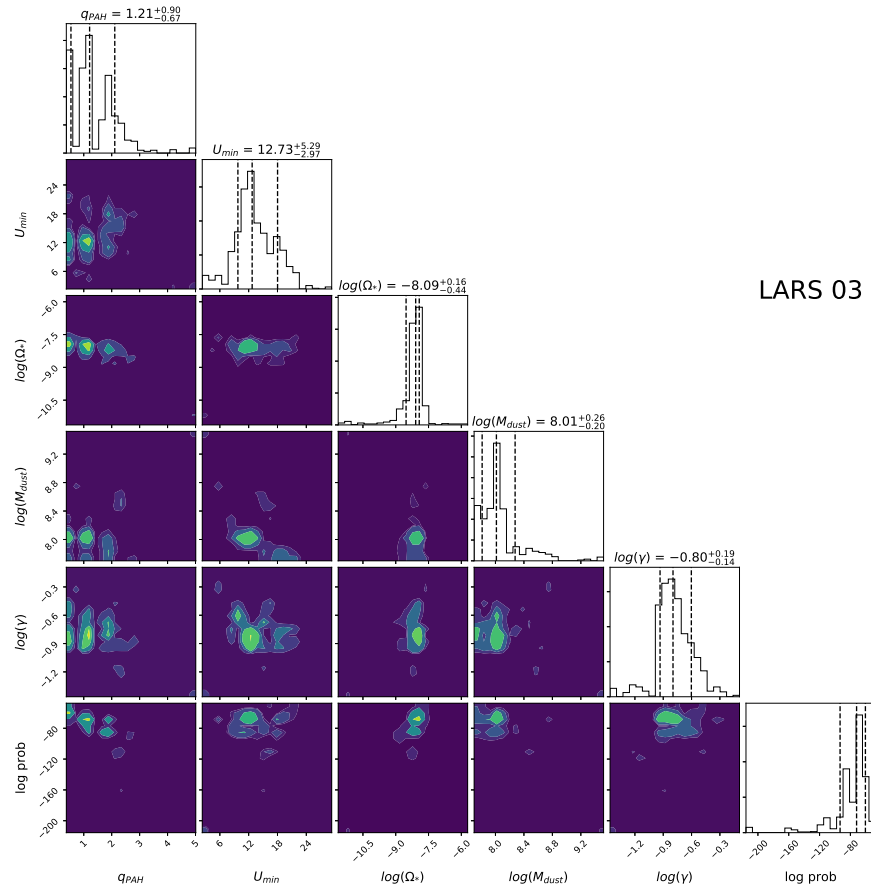
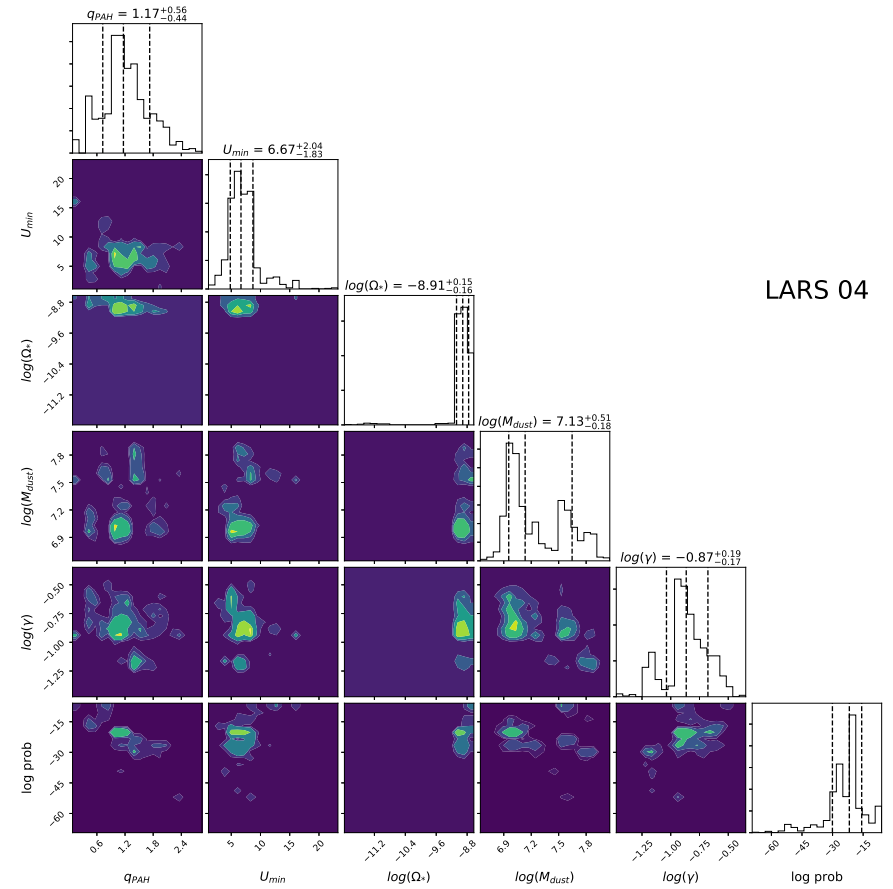


Figure 15. Corner plots showing the posterior probability distribution for the derived Draine & Li model parameters.

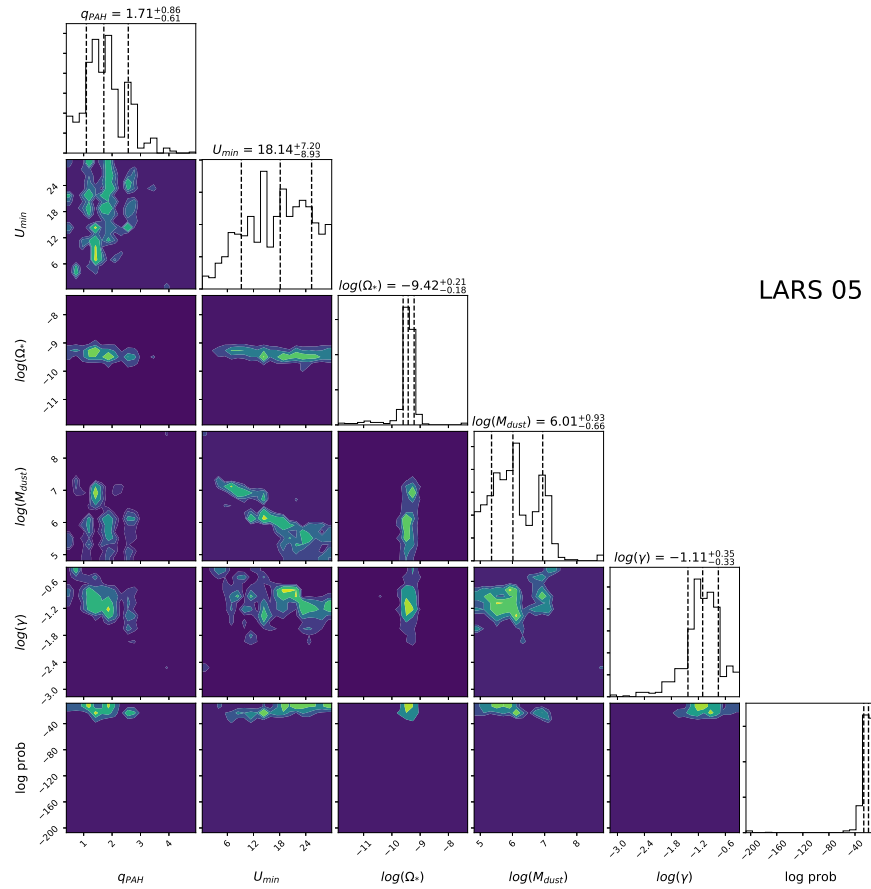


LARS 03

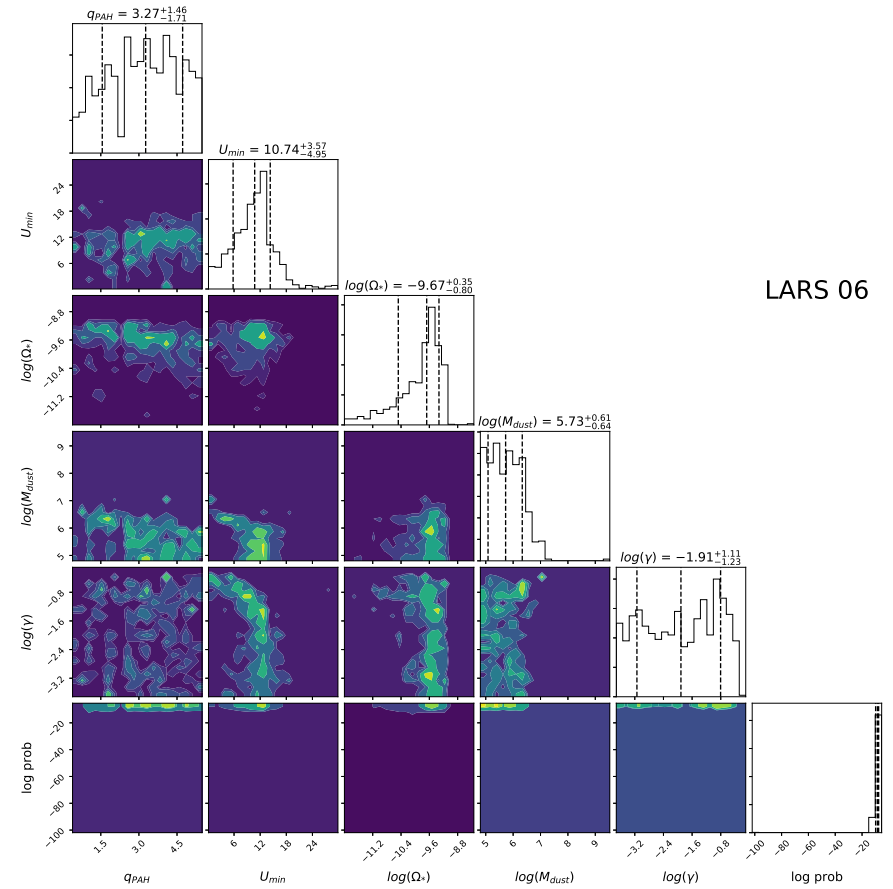


LARS 04

Figure 16. Corner plots showing the posterior probability distribution for the derived Draine & Li model parameters.

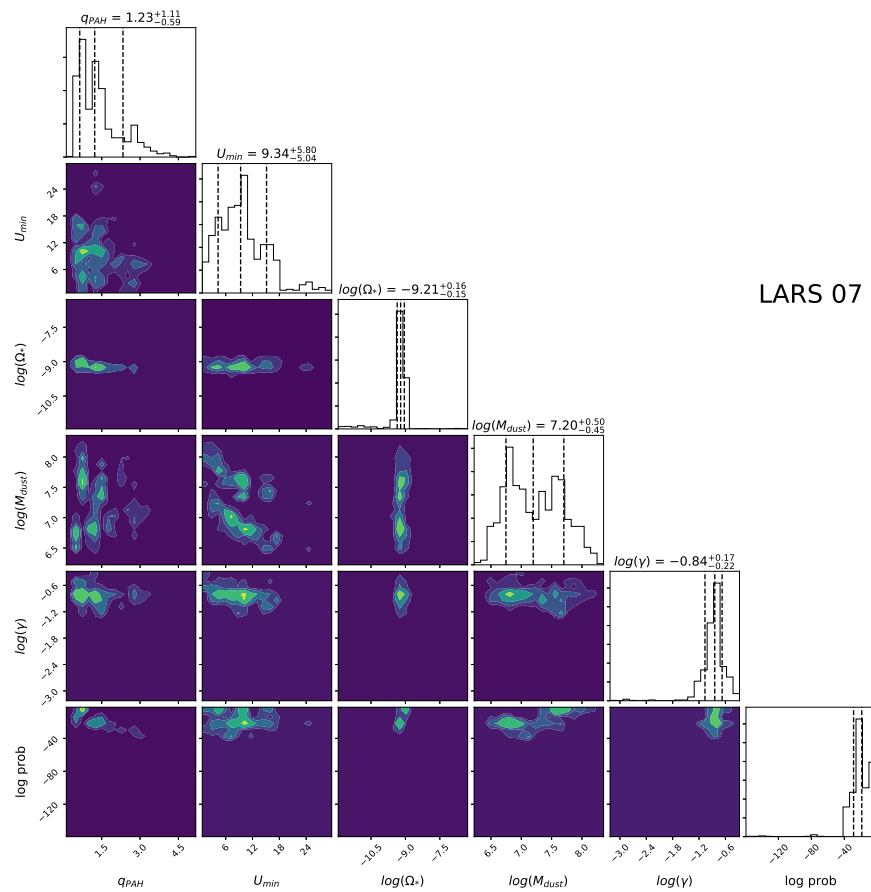


LARS 05

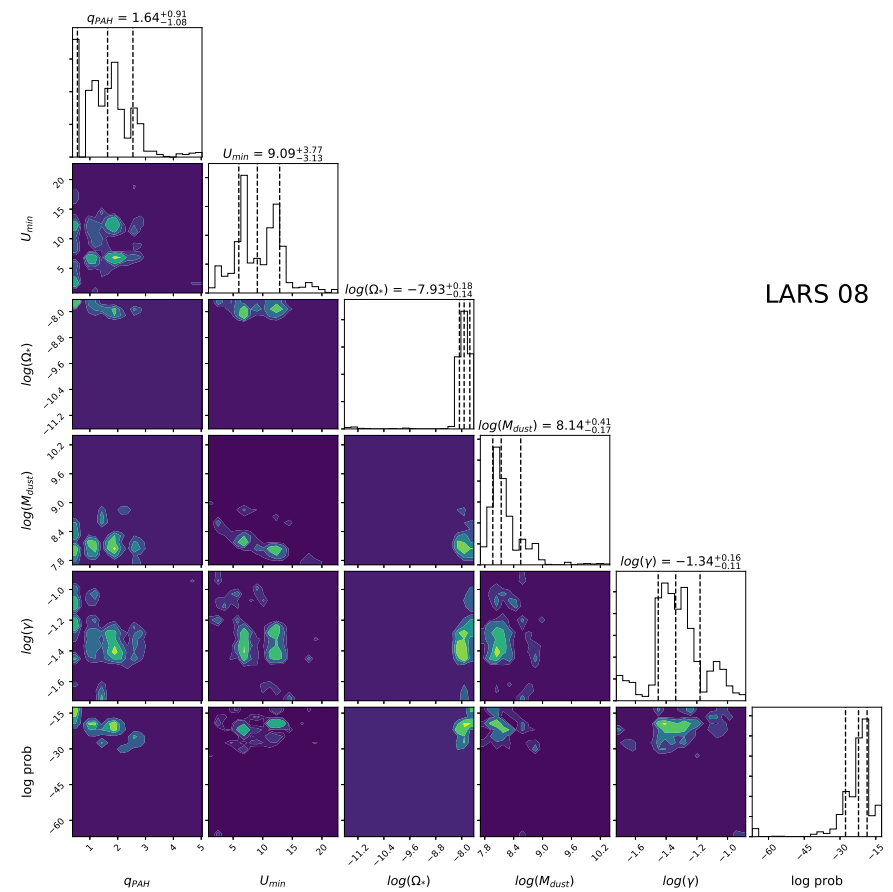


LARS 06

Figure 17. Corner plots showing the posterior probability distribution for the derived Draine & Li model parameters.

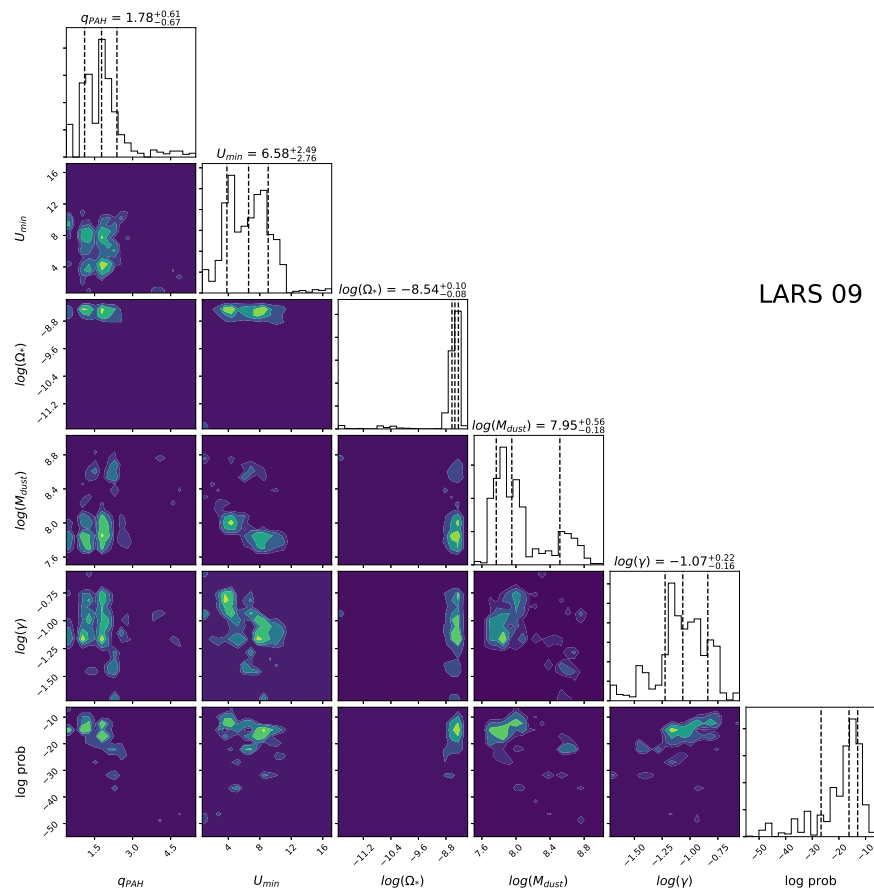


LARS 07

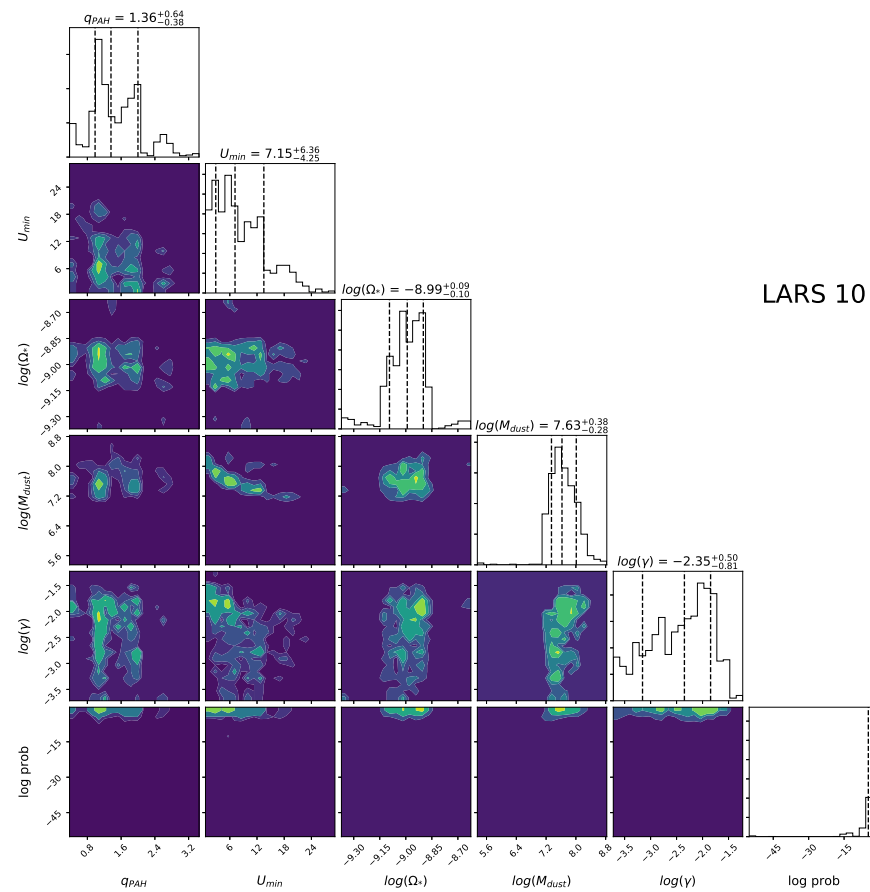


LARS 08

Figure 18. Corner plots showing the posterior probability distribution for the derived Draine & Li model parameters.

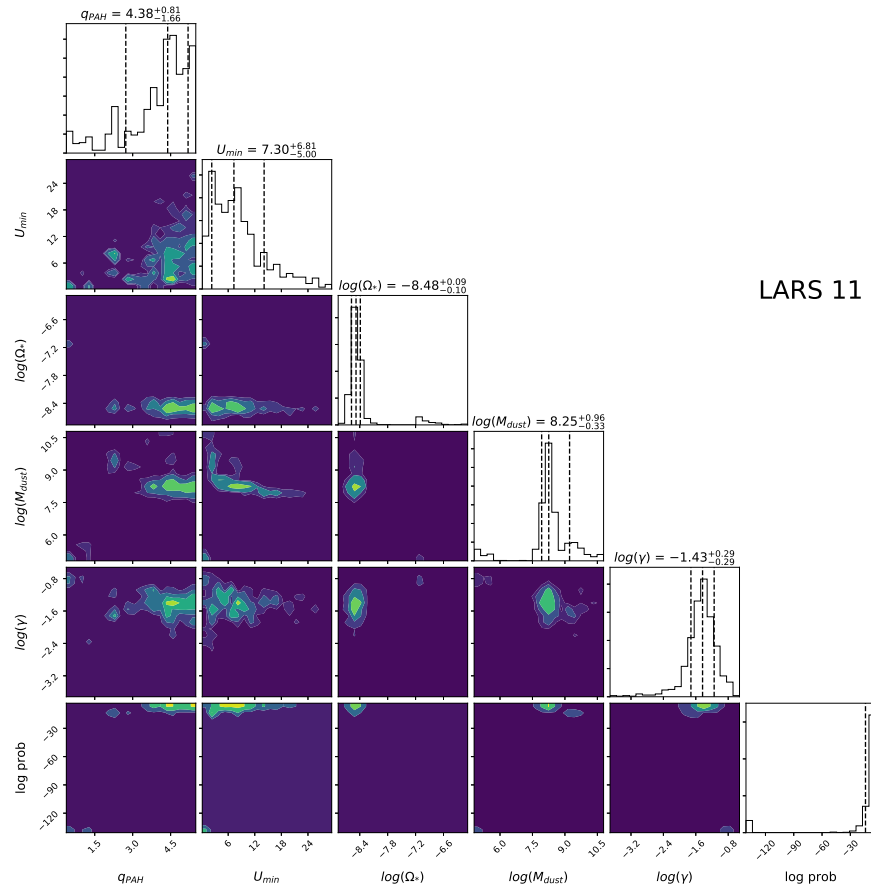


LARS 09

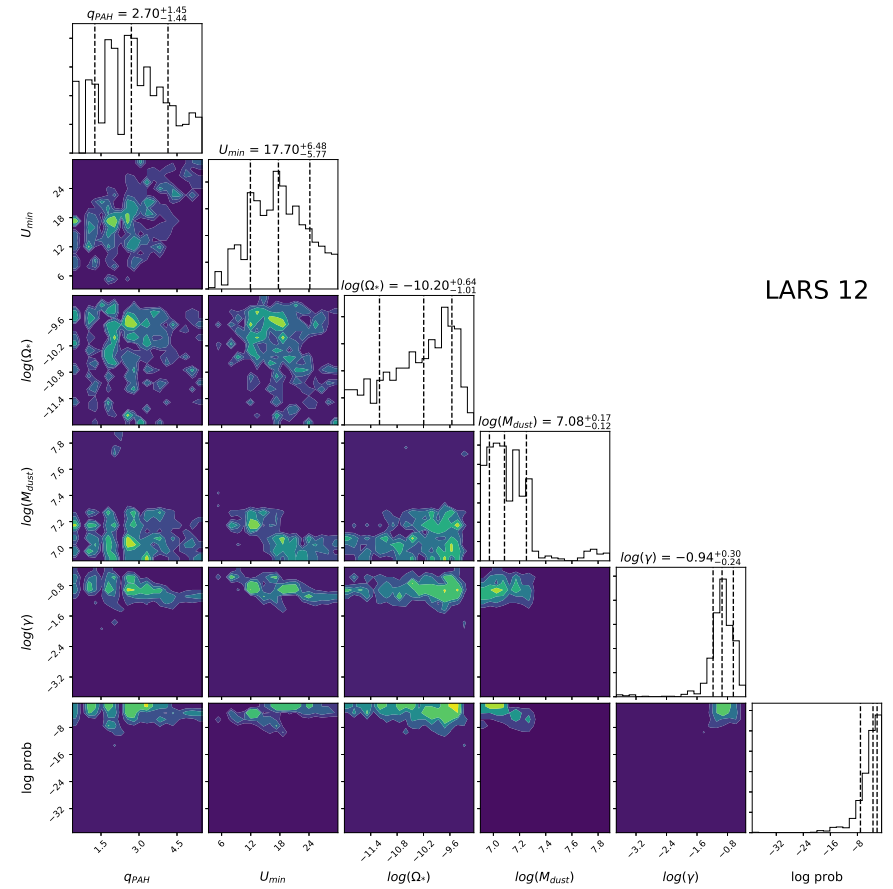


LARS 10

Figure 19. Corner plots showing the posterior probability distribution for the derived Draine & Li model parameters.

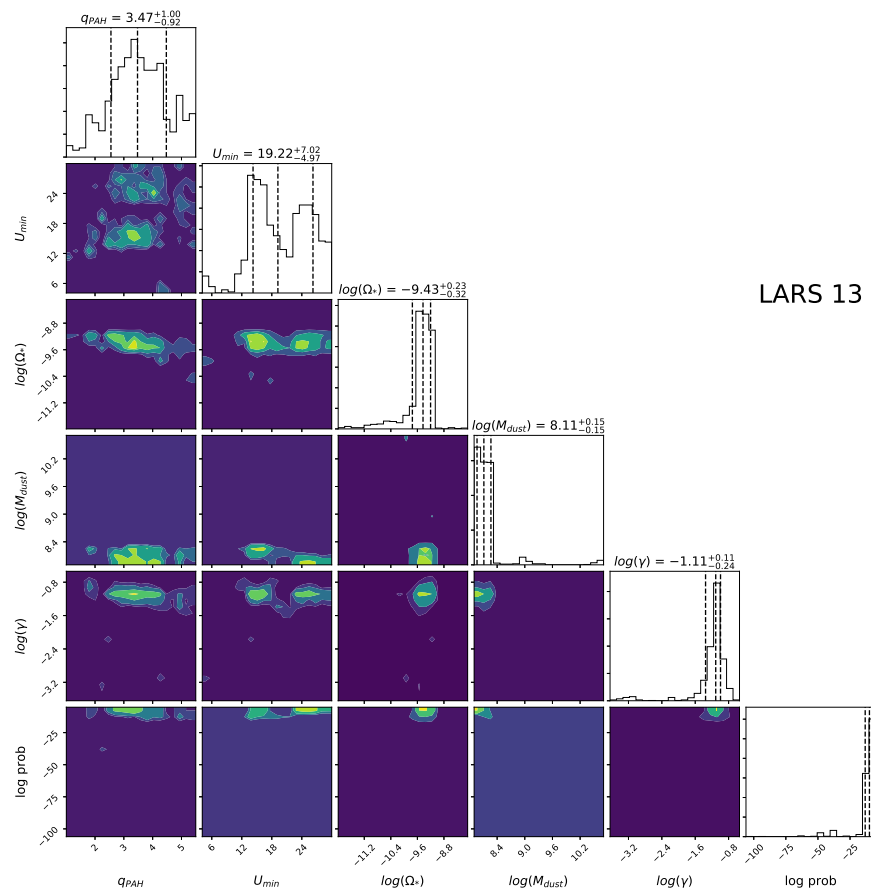


LARS 11

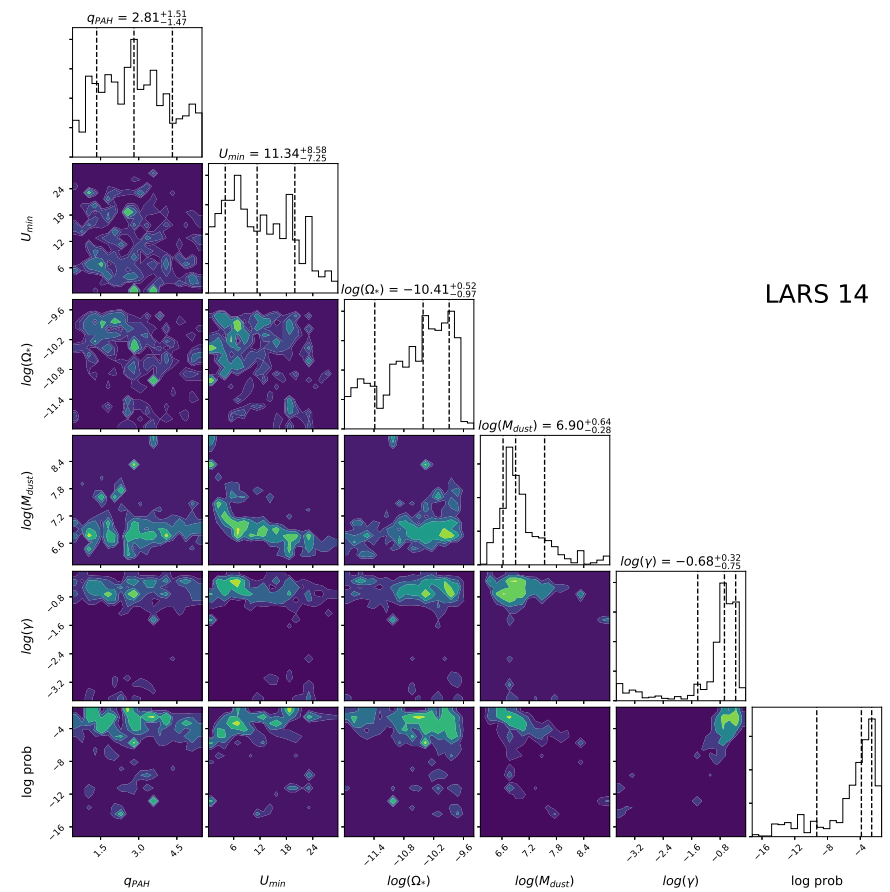


LARS 12

Figure 20. Corner plots showing the posterior probability distribution for the derived Draine & Li model parameters.



LARS 13



LARS 14

Figure 21. Corner plots showing the posterior probability distribution for the derived Draine & Li model parameters.

B Draine & Li SED fits using the MCMC method

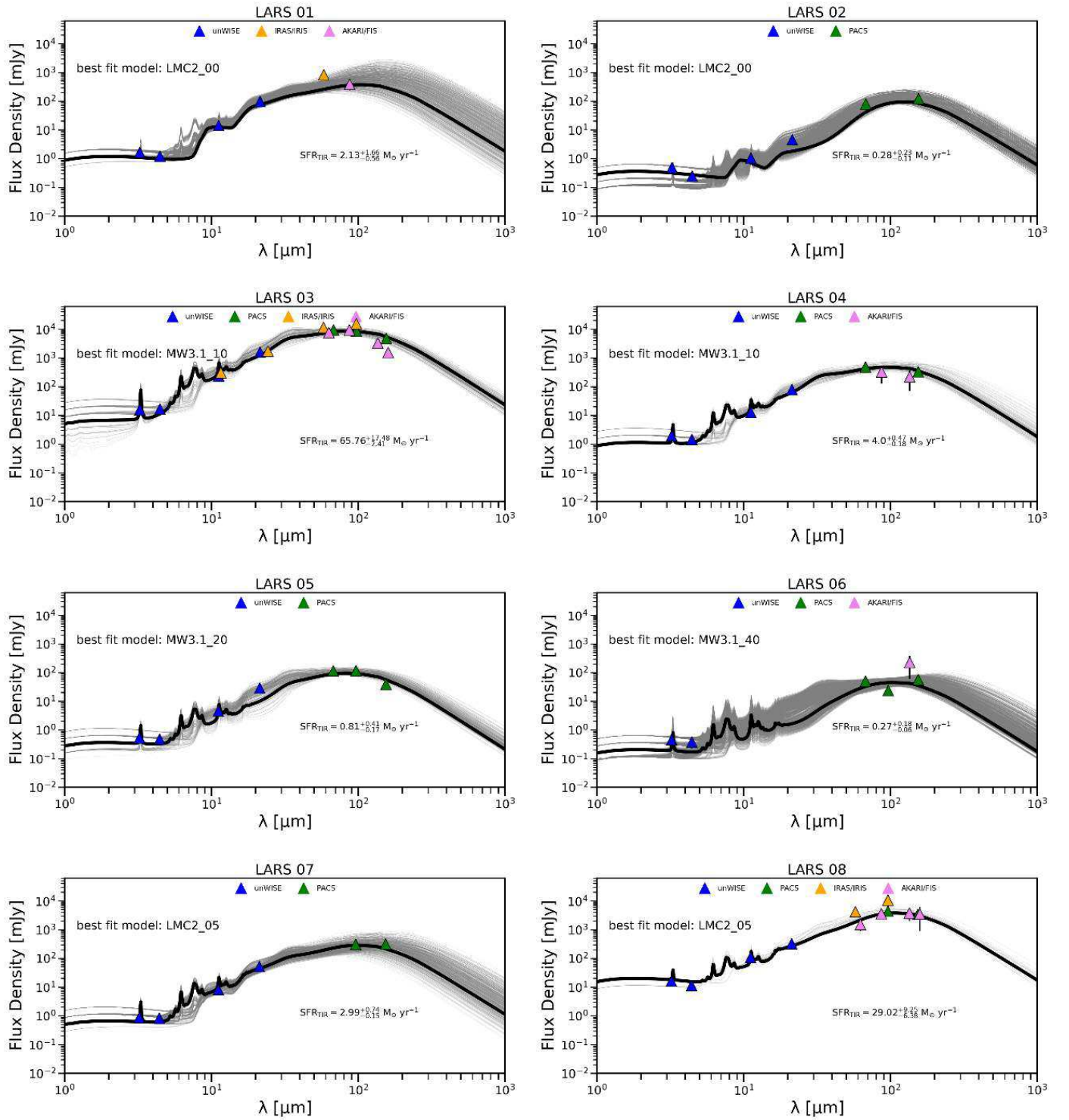


Figure 22. Infrared spectral energy distribution of LARS galaxies inferred from exploration of the parameter space using the Markov-Chain Monte Carlo method. The best fit SED is indicated by a *thick black curve* and was found from the 50% quantile of the logarithmic posterior distribution. The other fits that are shown (*thin grey lines*) are those lying within the quantile-based credible interval corresponding to 16% and 84%. They are thus representing our uncertainties.

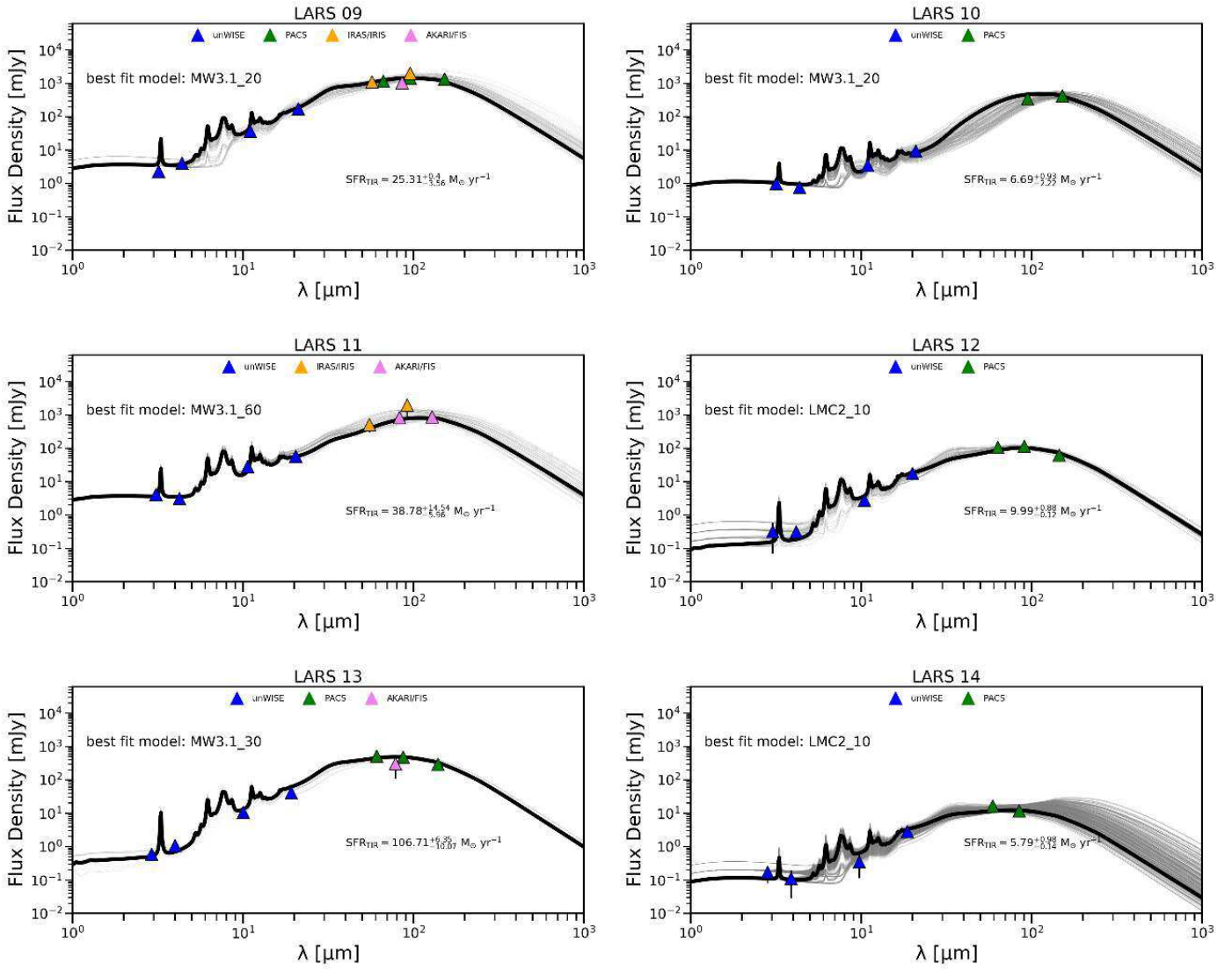


Figure 23. Same as in Figure 22.

C PDR models Fit Quality

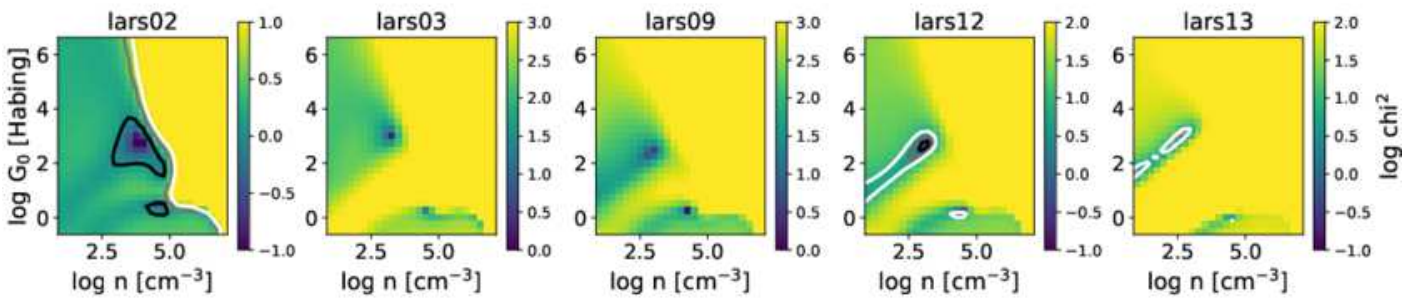


Figure 24. PDR model logarithmic χ^2 distribution across the (n, G_0) solution plane. The contours show 1, 2 and 3 σ significance regions around the best model fits. Note that for LARS 3 and 9 (both merging galaxies) the models are not able to reproduce the observations.

D Molecular Gas Density and Temperature from Line Radiative Transfer Modeling

Table 15. Calculated molecular line ratios used as input for radiative transfer modeling of LARS 3 and 8

ID	Line	I_{mb} [K km/s]	C_{AP}	θ [arcsec]	Line/CO(1-0)
3	CO (1-0)	7.13	1.94	22.1	1.00
3	CO (2-1)	15.93	3.58	11.0	1.02
3	HCN (1-0)	1.06	1.00	28.7	0.13
3	HCO+ (1-0)	1.08	1.00	28.6	0.13
8	CO (1-0)	6.85	1.36	22.2	1.00
8	CO (2-1)	11.70	1.10	11.1	0.35
8	CO (3-2)	6.50	1.00	18.5	0.48
8	HCN (1-0)	0.29	1.00	28.9	0.05
8	HCO+ (1-0)	0.19	1.00	28.7	0.03

The galaxy id is given in *column 1*, followed by the observed integrated main beam brightness temperature in *column 2* and the aperture correction factor as well as the beam size in *columns 3 and 4*. Normalized line ratios (*column 5*) are then calculated as: $(I_{\text{mb}} * C_{\text{AP}} * \theta^2) / (I_{\text{mb,CO10}} * C_{\text{AP,CO10}} * \theta_{\text{CO10}}^2)$. Note that the squared beam-size needs to be taken into account, as explained in Solomon and Vanden Bout (2005).

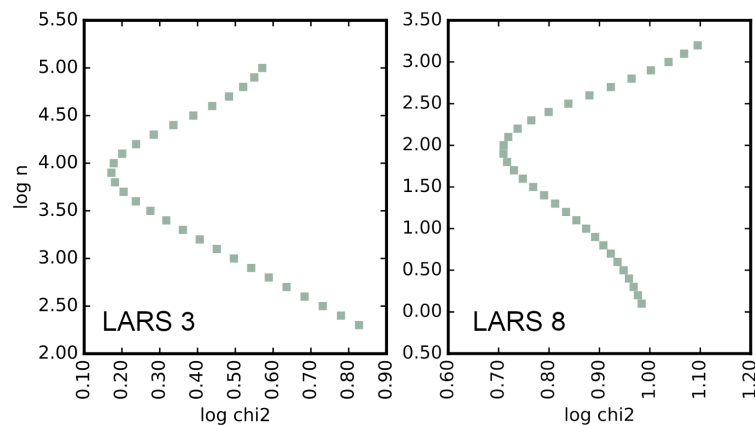


Figure 25. Mass-weighted mean molecular gas density vs. χ^2 for LARS 3 and 8. The (mass-weighted) mean density ($\log n$) of the emitting gas could be derived using a novel radiative transfer approach. The models (Puschnig et al. in prep) were minimized against observed line luminosities of CO (1-0), CO (2-1), HCN (1-0) and HCO+ (1-0) for LARS 3 and additional CO (3-2) for LARS 8.

E Choice of GDR and α_{CO}

Given the fact that our galaxy sample is very heterogeneous in terms of metallicity, stellar mass and star formation activity, we adopt a metallicity-dependent gas-to-dust ratio and CO-to-H₂ conversion factor when calculating total and molecular gas masses respectively. For the galaxies with atomic gas mass estimates from HI 21 cm observations, we compare available recipes for GDR and α_{CO} . The results are shown in Table 16. We find that the combination of the prescriptions in Narayanan et al. (2012) (N12) for α_{CO} and the linear GDR scalings in Rémy-Ruyer et al. (2014) give the best fit for our sample, with a deviation of only ~ 0.1 dex for the total gas mass (see Figure 9). The sublinear GDR scaling of Leroy et al. (2011) (L11) for example underestimates our observed molecular masses. The α_{CO} prescriptions of Schrubba et al. (2012) (S12) and Accurso et al. (2017) (A17) lead to deviations of ~ 0.3 dex and ~ 0.2 dex compared to our dust-based estimates. It is important to note that the prescriptions for α_{CO} of N12, S12 and A17 are fundamentally different and rely on different assumptions. S12 assume a constant star formation efficiency or gas depletion time to

derive their relation for the metallicity-dependence of α_{CO} . A17 use combined CO (1-0) and [C II]158 μm observations and relate those to α_{CO} . In their prescription, α_{CO} depends not only on metallicity, but also on the offset of the galaxy from the main sequence. The metallicity basically describes the total dust content available to shield CO from UV radiation and the offset from the main sequence describes the strength of this radiation field. On the other hand, N12 define α_{CO} to depend on metallicity and CO surface brightness I_{CO} (i.e. velocity integrated brightness temperature). While the metallicity dependence in N12 has basically the same meaning as in S12 or A17, i.e. to account for CO-dark gas at low dust contents, the dependence on I_{CO} makes α_{CO} sensitive to environmental variations, i.e. variations in density and temperature of the molecular gas. For example, it is known that ULIRGs (mergers) have lower α_{CO} values, because in nuclear starbursts the molecular gas is denser and hotter with molecular gas being mostly non-virialized compared to normal star forming regions. This leads to brighter CO emission (and thus lower α_{CO}) due to higher excitation temperatures. The fact that 1) the peak brightness temperature of the emission is sensitive to excitation temperature, and 2) the line width increases in the presence of non-virialized, dense, hot gas, makes I_{CO} sensitive to changing environmental conditions. Hence, the reason why the α_{CO} prescription of N12 best fits our observations is an indication for changing environmental conditions among LARS galaxies that have strong implications for α_{CO} .

Table 16. Mean deviation in *dex* of dust-based estimates of the molecular gas mass ΔM_{H_2} , i.e. dust-based total gas minus M_{HI} from Pardy et al. (2014), see Table 1, and mean deviation in *dex* of dust-based estimates of the total gas mass ΔM_{gas} , i.e. dust-based total gas minus $M_{\text{HI}}+M_{\text{H}_2}$. Note that deviations could only be calculated for galaxies with both, M_{HI} and M_{H_2} measured (LARS 3, 8, 9 and 11), and are biased towards higher metallicities. We evaluate the deviations for a combination of prescriptions for the gas-to-dust ratio (R14: Rémy-Ruyer et al. (2014), L11: Leroy et al. (2011), and for the CO-to- H_2 conversion factor (N12: Narayanan et al. (2012), S12: Schruba et al. (2012), A17: Accurso et al. (2017)).

	N12	N12	S12	S12	A17	A17
	ΔM_{H_2}	ΔM_{g}	ΔM_{H_2}	ΔM_{g}	ΔM_{H_2}	ΔM_{g}
R14,ref	0.23	0.11	0.48	0.32	0.34	0.19
R14,PL	0.61	0.36	0.31	0.22	0.31	0.28
R14,BPL	0.23	0.11	0.48	0.32	0.34	0.19
L11	neg	0.14	neg	0.52	neg	0.14